UNIVERSIDADE FEDERAL DE PERNAMBUCO
CENTRO DE CIÊNCIAS EXATAS E DA NATUREZA
PROGRAMA DE PÓS-GRADUAÇÃO EM FÍSICA

ALEXANDRE ANDRADE CAVALCANTI DE ALMEIDA

FORWARD FOUR-WAVE MIXING EXPERIMENTS IN HOT AND COLD ATOMIC SYSTEMS

Recife
2023

ALEXANDRE ANDRADE CAVALCANTI DE ALMEIDA

FORWARD FOUR-WAVE MIXING EXPERIMENTS IN HOT AND COLD ATOMIC SYSTEMS

Tese apresentada ao Programa de Pós-Graduação em Física da Universidade Federal de Pernambuco, como requisito parcial para obtenção do título de doutor em Física. Área de concentração: Óptica.

Orientadora: Profa. Dra. Sandra Sampaio Vianna

Recife

2023

Catalogação na fonte
Bibliotecária Nataly Soares Leite Moro, CRB4-1722

A447f Almeida, Alexandre Andrade Cavalcanti de
Forward four-wave mixing experiments in hot and cold atomic systems / Alexandre Andrade Cavalcanti de Almeida. – 2023.
165 f.: il., fig.

Orientadora: Sandra Sampaio Vianna.
Tese (Doutorado) – Universidade Federal de Pernambuco. CCEN, Física, Recife, 2023.
Inclui referências e apêndices.

1. Óptica. 2. Mistura de quatro ondas. 3. Ótica não-linear. 4. Espectroscopia atômica. 5. Vapor de rubídio. I. Vianna, Sandra Sampaio (orientadora). II. Título.

535.2 CDD (23. ed.) UFPE- CCEN 2023 - 46

ALEXANDRE ANDRADE CAVALCANTI DE ALMEIDA

FORWARD FOUR-WAVE MIXING EXPERIMENTS IN HOT AND COLD ATOMIC SYSTEMS

Tese apresentada ao Programa de Pós-Graduação em Física da Universidade Federal de Pernambuco, como requisito parcial para a obtenção do título de Doutor em Física.

Aprovada em: 28/02/2023.

BANCA EXAMINADORA

_____

Profa. Sandra Sampaio Vianna
Orientadora
Universidade Federal de Pernambuco

_____

Prof. Daniel Felinto Pires Barbosa
Examinador Interno
Universidade Federal de Pernambuco

_____

Prof. Lúcio Hora Acioli
Examinador Interno
Universidade Federal de Pernambuco

_____

Prof. Celso Jorge Villas-Bôas
Examinador Externo
Universidade Federal de São Carlos

_____

Prof. Marcelo Martinelli
Examinador Externo
Universidade de São Paulo

AGRADECIMENTOS

Os quatro anos em que fiz meu doutorado foram desafiadores. Anos em que vivemos uma pandemia que afetou o mundo inteiro. Anos em que vivemos uma luta diária para manter viva a produção científica no Brasil. Nesse contexto seria impossível fazer um trabalho como este sem a ajuda de muitas pessoas. Expresso então meus sinceros agradecimentos.

À minha esposa Mariana Pessoa, por não só me acompanhar desde os tempos em que a física era só um sonho, como por garantir que eu não desistisse no meio do caminho. Mais ainda, por me dar a maior alegria da vida, meu pequeno Murilo.

Aos meus pais Evângela Andrade e Antônio Carlos Almeida, que me apoiaram integralmente na minha formação e a todos familiares, em especial meu irmão Mário Jorge Andrade que mesmo com a pouca idade muito me ajudou.

À professora Sandra Vianna, que aceitou me orientar desde o segundo período da graduação até o fim do doutorado, depois de quase uma década. Agradeço por ser um modelo de orientadora, que espero um dia poder atingir.

Aos amigos que do laboratório levo para a vida, Alexis García-Wong, Mateus Motta e Natalia de Melo.

Agradeço a todos os colegas de curso, aos professores e funcionários do departamento de física e a todos aqueles que desempenharam os mais diversos papéis para a conclusão deste trabalho.

Por fim, agradeço ao CNPq pelo apoio financeiro.

ABSTRACT

In this work, we present a set of experiments involving four-wave mixing processes in rubidium atoms. We employ several experimental configurations exploring two- and three-level systems in cascade or Λ configurations, all of which are in a copropagating geometry, to investigate different physical phenomena present in each scenario. In the first experiment, we combine a cw diode laser and a 1 GHz femtosecond pulse train to generate coherent blue light through the four-wave mixing process in hot rubidium vapor. The generated coherent signal is analyzed by scanning either the diode frequency or the repetition rate of the frequency comb. In both cases, the cw laser induces an Autler-Townes splitting with a wide separation in the doublet structure due to the configuration of copropagating fields. To model these results, we employ the density matrix formalism to write the Bloch equations and solve them numerically. The solutions allow us to explore other cases beyond those involving our experimental setup, comparing the response of the upper-level population and the generated signal coherence for homogeneously and non-homogeneously broadened systems. Moreover, in this same experiment, we also observed an unexpected interference effect between excitation routes of the four-wave mixing process when the repetition rate of the pulse train is scanned. The theoretical model demonstrates that the interfering effect appears only when the repetition rate is carefully chosen to produce a pair of modes of the frequency comb resonant with both one- and two-photon transitions for the same atomic velocity group. In the second experiment, still with a hot rubidium vapor, we explore two symmetrical degenerate four-wave mixing signals induced by two almost copropagating laser beams, with $\vec{k}_a$ and $\vec{k}_b$ wave-vectors, and detected simultaneously in the $2\vec{k}_a - \vec{k}_b$ and $2\vec{k}_b - \vec{k}_a$ directions. Each spectrum has a single peak with a short frequency separation between them, which our model indicates is due to the nonlinear behavior of the refractive indexes, a consequence of the high intensity of both input fields. Finally, we use the same experimental setup for the two symmetrical signals to study the field intensity fluctuations of the degenerate four-wave mixing signals and the transmission signals. In this case, the sample is an ensemble of cold rubidium atoms in a magneto-optical trap. There is an intensity-intensity cross-correlation between the signals due to the resonant phase-noise to amplitude-noise conversion. In this type of cold system, we can neglect the Doppler-

broadening, allowing a straightforward study of the dependency of the correlations on the laser detuning. In these measurements, we observe a type of oscillation in the correlation curves that the theoretical model indicates to be connected with Rabi oscillations, revealed by the fluctuations long after the transient period.

Keywords: four-wave mixing; nonlinear optics; atomic spectroscopy; rubidium vapor; cold atoms.

RESUMO

Neste trabalho, é apresentado um conjunto de experimentos envolvendo processos de mistura de quatro ondas em átomos de rubídio. Diversas configurações experimentais são utilizadas explorando sistema de dois e três níveis em configuração de cascata e Λ, todas numa geometria copropagante, procurando investigar fenômenos físicos presentes em cada cenário. No primeiro experimento, um laser de diodo contínuo e um trem de pulsos ultracurtos, de 1GHz, são combinados para gerar um sinal de luz azul coerente via processo de mistura de quatro ondas em um vapor quente de rubídio. O sinal coerente é analisado variando a frequência do laser de diodo ou a taxa de repetição do pente de frequências. Em ambos os casos, o laser contínuo induz um efeito Autler-Townes com uma larga separação na estrutura de dubleto devido à configuração copropagante dos campos. O formalismo da matriz densidade é utilizado para modelar esses resultados, obtendo as equações de Bloch e as resolvendo numericamente. As soluções permitem explorar mais cenários que o experimento, comparando a resposta da população do estado excitado e do sinal gerado coerentemente para sistemas alargados homogênea e inomogeneamente. Ademais, neste mesmo experimento, também se observa um efeito de interferência inesperado entre rotas de excitação do processo de mistura de quatro ondas quando a taxa de repetição do trem de pulsos é variada. O modelo teórico demonstra que este efeito de interferência ocorre apenas quando a taxa de repetição é escolhida cuidadosamente para produzir um par de modos do pente de frequência ressonante com ambas as transições de um e dois fótons para o mesmo grupo de velocidade. O segundo experimento, ainda utilizando vapor quente de rubídio, explora dois sinais simétricos de mistura de quatro ondas degenerada, induzidos por dois campos quase copropagantes com vetores de onda $\vec{k}_a$ e $\vec{k}_b$, e detectados simultaneamente nas direções $2\vec{k}_a - \vec{k}_b$ e $2\vec{k}_b - \vec{k}_a$. Cada espectro apresenta um único pico com uma pequena separação em frequência entre eles. O modelo teórico indica que esta separação é causada pelo comportamento não linear do índice de refração devido ao fato dos dois feixes incidentes serem intensos. Finalmente, a mesma configuração experimental de geração de sinais simétricos é utilizada para estudar as flutuações de intensidade dos sinais de mistura de quatro ondas degenerada e dos sinais de transmissão. Nesse caso, a amostra é um conjunto de átomos frios

de rubídio em uma armadilha magneto-ótica. Existe uma correlação cruzada entre as intensidades dos sinais, devido à conversão ressonante de ruído de fase em ruído de amplitude. Neste tipo de sistema frio, é possível descartar o alargamento Doppler, o que permite um estudo mais direto da relação entre a correlação e a dessintonia do laser. Nestas medidas, observa-se um tipo de oscilação nas curvas de correlação que o modelo teórico indica estar conectado com oscilações de Rabi, reveladas pelas flutuações de intensidade muito tempo após o período transiente.

Palavras-chave: mistura de quatro ondas; ótica não-linear; espectroscopia atômica; vapor de rubídio; átomos frios.

LIST OF FIGURES

CONTENTS

1 INTRODUCTION

A new era in optics began with the development of the first laser by Maiman [1] in 1960. This source of intense coherent light is behind several technological innovations that do not restrict themselves to physics but permeates several areas of knowledge, from basic science to industry or even medicine. In physics, the impact was particularly overriding for the field of nonlinear optics [2] since laser light combines high coherence and high intensity in a way never seen before. These properties represented an enormous advance from the previous light sources, which gave rise to a new type of physical process to be studied.

Nonlinear optics has been studied as early as the nineteenth century, with the first studies on the Kerr effect [3]. However, the first experiment to explore this area of physics in the laser era was the classical experiment by Franken *et al.* in 1961 [4]. It is impressive how quickly this invention, the laser, was already being used in the most different scenarios in such a short time. In this experiment, Franken *et al.* shone a quartz crystal with an intense pulse of red light from a ruby laser. The output signal included a small blue light pulse with precisely half the wavelength of the original red light. This new frequency is generated because of the crystal nonlinearity, rendering the famous second harmonic generation (SHG).

After this demonstration of the potential of the laser in nonlinear optics, a series of new fascinating results came along. We can quote some relevant examples, such as the observation of two-photon absorption by Kaiser and Garrett [5], the stimulated Raman scattering by Ng and Woodbury [6], the third-harmonic generation, and the anti-Stokes frequency mixing both by Maker and Terhune [7, 8]. An interesting case is the parametric down-conversion [9], the inverse process of SHG. In this phenomenon, one photon interacts with a nonlinear medium (typically a crystal) and generates two photons, obeying momentum and energy conservation. These “twins” photons are produced simultaneously and are said to be correlated. The particularity of these output photons lies in the statistics behind the process. In opposition to the classical fields produced by a beam splitter acting on a laser, for example, that obeys Poisson counting

statistics, the twin photons of the parametric down-conversion present a correlation incompatible with classical light fields. This is one example of non-classical light, which eventually resulted in modern quantum optics, a field in accelerated growth in the past decades.

The topics of nonlinear optics we want to address in this thesis arise from the interaction of coherent optical fields within a third-order nonlinear medium. In particular, among the several third-order phenomena, we are interested in four-wave mixing (FWM). This process has been used extensively to investigate a variety of optical phenomena in different atomic systems. Regarding the energy structure, since very early studies, different atomic level configurations have been explored to enhance the efficiency of this nonlinear process as, for example, two-level [10, 11], three-level Λ [12, 13], and four-level double-Λ schemes [14].

In terms of recent applications of FWM that are relevant to some of the results in this thesis, we may cite the generation of quantum correlated beams [15, 16], the storage of quantum memory, the transfer of orbital angular momentum between light beams [17, 18], the reduction of the paraxial diffraction of light [19], and the development of single-photon sources [20].

In particular, a common characteristic in much of the FWM processes described in the literature is the possibility to control the refractive index [21] of the medium, and in some conditions cancel the resonant absorption, due to the phenomenon of electromagnetically induced transparency (EIT) [22, 23], or enhance the absorption, via electromagnetically induced absorption (EIA) [24, 25].

We describe the FWM process in more detail in section 2, where we present the fundamental concepts necessary for understanding the experiments reported in this thesis. Namely, we delineate the energy structure of our sample, rubidium atoms, which we explore in different experimental setups involving hot vapors or cooled trapped Rb gases. Moreover, we present the electromagnetic wave theory, which eventually connects with the theoretical models for the phenomena, building a semiclassical treatment, in which the fields are classic, but the atoms are quantum systems. The quantum treatment of the atomic systems is provided, as well as an example of a

three-level system, which is useful for the description of the results of the remaining sections.

The bulk of this work encloses three different experiments, each one exploring different aspects and effects of the FWM process, in particular, in a forward configuration. This configuration poses some experimental challenges but also reveals phenomena that could not be observed in a counterpropagating arrangement of the input fields.

Most of the FWM experiments are performed with cw lasers, exploring the high power and the tunability near atomic resonances. However, a powerful tool one can employ is a femtosecond (fs) laser, taking advantage of coherent temporal control techniques [26]. In recent years, advances in ultrafast lasers have enhanced the direct application of mode-locked fs lasers, leading, for instance, to the development of a rapid multidimensional coherent spectroscopy with high spectral resolution [27]. In this sense, we present in section 3 a set of results involving a coherent blue light signal obtained through an FWM process using a combination of cw laser and femtosecond pulse train. This combination allows us not only to probe the action of each laser but also to explore the different characteristics of the nonlinear process.

In particular, we want to explore the dynamic Stark shift, also known as the AC Stark effect, observed in the FWM results of this experiment. This phenomenon occurs when a near-resonant strong field interacts with matter. It results in the energy level splitting at a transition and has important implications in spectroscopy. In three-level systems, this effect is also known as the Autler-Townes (AT) splitting [28]. Typically, it results in a double peak in the weak field absorption, with the most common setup in three-level cascade systems being with counterpropagating laser beams, exploring the almost Doppler-free configuration. However, our experimental setup has a copropagating configuration, leading to different results. In particular, we demonstrate that the AT doublet, in the copropagating setup, can only be distinguished in the FWM signal, in opposition to what would be detected in the fluorescence signal. To confirm this, we employ numerical methods to model the phenomenon in the high-intensity regime and for a Doppler-broadened media, exploring more scenarios than in the experiment.

Another feature the same experimental system allows us to observe is an inter-

ference between FWM excitation routes. This interference is characterized by a very narrow peak over the AT spectra, and it connects with the repetition rate of the fs laser. We show that if one tunes the repetition rate attentively, the first step of the FWM process can be performed by either of the lasers, cw or fs. This creates a situation of indistinguishability, inducing an interference that can be controlled via the repetition rate of the fs laser.

Working with Doppler-broadened media still, we present in section 4 results regarding a degenerate FWM process. In this case, we focus on two symmetric FWM signals that are generated within a hot rubidium cell. These signals are generated by two laser beams, with $\mathbf{k}_a$ and $\mathbf{k}_b$ wave vectors. It is an interesting configuration since most of the experiments involving degenerate FWM are performed by counterpropagating input laser beams, as this setup satisfies the phase-matching conditions automatically. However, we show the phase-matching conditions for copropagating configurations give rise to new interesting phenomena. In particular, we observe that each FWM spectra shows a single peak separated by a small frequency shift when the two input fields resonate with the closed transition ^{85}Rb $5S_{1/2}(F=3) \rightarrow 5P_{3/2}(F=4)$. This frequency shift itself is not unexpected, as there are reports in the literature connecting it to the phase-matching conditions [29], in which the phase mismatch is mainly due to the wavelength differences. However, since our process is degenerate, the changes in the refractive index of both input fields lead to a shift in the opposite direction of these typical cases.

Especially, as we detect the two signals simultaneously, we can distinguish a frequency shift towards red or blue, from each peak associated with the FWM signals, depending on how the beam whose frequency is swept contributes to the observed signal. Naturally, understanding how to effectively control the proprieties of the atomic media, where the nonlinear process is taking place, is of widespread interest for fundamental aspects of atom-light interaction. In this sense, this section aims to investigate the main physical mechanisms responsible for these frequency shifts and how they are related to the coherence induced in the atomic system.

Finally, in section 5, we present a study of the correlation between intensity fluctuations of both FWM signals and the transmission signals in a similar experimental

configuration to section 4. However, for this study, we change the hot rubidium cells for a cloud of trapped Rb atoms in a magneto-optical trap. We do so to avoid the complications of Doppler-broadening, as one of the objectives of this experiment is to study how these correlations behave as a function of laser detuning. As will be discussed extensively, Doppler-broadened media have several velocity groups that respond differently to the input laser in terms of detuning, while the cold sample has a very narrow Maxwell-Boltzmann distribution.

There has been a significant interest in the past decades in the study of light intensity fluctuations when it interacts with matter. Early experimental work by Yabusaki *et al* [30] demonstrated that it was possible to obtain spectroscopic information by analyzing the intensity fluctuations of a laser beam interacting with rubidium vapor, that is, without any need to modulate the laser frequency. R. Walser and P. Zoller [31] then provided a theoretical framework to explain this new spectroscopy, in particular how the conversion of phase noise to amplitude noise plays a crucial role in the process.

This type of spectroscopy involves the measurement of noise (or fluctuations) in a system to extract information about the underlying physics. This can be done by analyzing the frequency spectrum of the noise, which may reveal information about the dynamics and interactions of the system. In laser systems, noise can arise from various sources, such as fluctuations in pump power, thermal fluctuations, and noise in cavity mirrors.

An important aspect of these cases is the distinction between different types of fluctuation. Typically one can model these fluctuations as Gaussian or non-Gaussian fluctuations, and the distinction between them is important because they reveal information about the noise sources within the system. For example, Gaussian noise is often associated with thermal fluctuations, while non-Gaussian noise is often associated with external noise sources and nonlinear processes [32].

Since these pioneering studies, there have been numerous research efforts focused on exploring these fluctuations in light-matter interactions. Notable findings include the examination of correlations and anti-correlations in electromagnetically induced transparency [33, 34, 35, 36], the control of intensity noise correlations and

squeezing of FWM processes through polarization [37], and the generation of correlated and anti-correlated fields using atomic spin coherence [38].

In our experiment, different polarization configurations are compared, accessing distinct internal energy level structures. Furthermore, we observe an oscillatory behavior compatible with Rabi oscillations [39] in the correlation functions. We can detect these oscillations long after the transient period, retrieving the frequency information through the correlation function. To model the correlation in general and, in particular understand these oscillations, we use the theoretical model from Ariunbold *et al.* [40] to simulate the fluctuations and look for agreements with the experimental results.

In this introductory section, we have provided a comprehensive overview of the research topic and problems that our thesis aims to address. We have discussed some of the backgrounds of the experiments, as well as the research questions and objectives that we will be addressing throughout the thesis. We have also outlined the thesis structure and the methods that were used. In section 6, we will present the conclusions of our research, summarize our findings, and discuss their implications for future research in the field.

2 FUNDAMENTAL CONCEPTS

This section introduces the basic set of concepts relevant to the understanding of the problems we address throughout this thesis. We begin describing the energy structure of alkali atoms, with particular attention to rubidium, as it is the atomic species we use in all of the experiments described here. Next, we briefly describe the classic electromagnetic fields that interact with the atomic medium to build a semiclassical treatment of the phenomena [41]. We then present the density-matrix formalism and the optical Bloch equations to study the dynamics of the atom-light interaction. As an example, we show the step-by-step solution of a three-level system interacting with two input fields. Not only this serves as an example but also sets the first steps to solving some of the problems of the following sections.

2.1 Energy structure of alkali atoms

The experiments presented here are all performed with rubidium samples, an alkali metal with the atomic number $Z = 37$. Alkalis are a family of elements much used in atomic physics experiments due to their single optically active electron. Even though these are multi-electron atoms, and therefore we cannot solve their energy structure analytically, we can make approximations that take advantage of their similarities with the hydrogen atom. With alkalis, all electrons but one fully occupy the energy subshells. The single unpaired valence electron behaves much like the single electron of hydrogen, meaning that, given adequate approximations, alkalis are a fairly simple atomic system to study.

In the past few decades, there was a popularization of rubidium and cesium samples in atomic spectroscopy laboratories. Since the 1990s, cheap diode lasers have been available in the near-infrared, the same region of the spectrum in which lies the D_1 and D_2 lines of Rb and Cs. The atomic vapor is also easily obtainable in small cells due to the relatively low vapor pressure of these atomic species, leading to the spread of these samples in many research groups. Especially for Rb, there was quite a success in laser cooling techniques with the development of the magneto-optical trap

[42] and consequently, the first realization of Bose-Einstein condensation [43], both achievements that rendered Nobel prizes.

Then, it is relevant for this work to understand the energy structure of the alkalis, with particular attention to Rb. One can perform a phenomenological qualitative analysis of the spectra and write down the energy levels of the alkalis (with some corrections) just like for the hydrogen atom. This is the so-called quantum defect approach, which uses the hydrogen expressions correcting the numerical parameters phenomenologically. On the other hand, more quantitative approaches are also available with the Hartree-Fock method [44] or even the post-Hartree-Fock methods that include electron correlation to achieve more precise results. However, in this work, we are interested in the energy structures that lie within the energy levels.

One can obtain the hydrogen energy structure through the Schrödinger equation. However, there are relativistic corrections that must be performed to account for some shifts in the energy levels or even degeneracy breaks. In the latter case, the existence of the electron spin leads to the spin-orbit (SO) interaction, which is described by the hamiltonian [44]

$$H_{SO} = \left(\frac{Ze^2}{4\pi\varepsilon_0}\right)\frac{(g_s-1)}{2m^2c^2r^3}\mathbf{L}\cdot\mathbf{S}, \tag{1}$$

where ε_0 is the vacuum permittivity; m is the electron's mass; g_s is the electron spin g-factor; $\mathbf{L}$ and $\mathbf{S}$ are the orbital and spin angular momentum operators, respectively.

The basic idea behind the SO coupling is that an electron's spin and orbital angular momentum are not independent, but are instead coupled together through the interaction of the electron's intrinsic magnetic moment with the magnetic moment of the orbit. This interaction results in a shift in the energy levels of the electron. One of the most relevant effects of SO coupling is the break of the degeneracy of some energy levels into the so-called fine structure.

To find out the energy shifts due to the SO coupling, it is interesting to look for an adequate set of quantum numbers, which will be $|n,L,S,J,m_J\rangle$. This way, we can express

the product $\mathbf{L}\cdot\mathbf{S}$ in terms of total angular momentum $\mathbf{J}=\mathbf{L}+\mathbf{S}$

$$\mathbf{L}\cdot\mathbf{S}=\frac{\mathbf{J}^2-\mathbf{L}^2-\mathbf{S}^2}{2}. \tag{2}$$

Therefore, the fine structure shift is proportional to

$$\Delta E_{fs}=\frac{A_{fs}}{2}\left[J\left(J+1\right)-L\left(L+1\right)-S\left(S+1\right)\right], \tag{3}$$

where all the parameters of Eq. 1 are contained in the constant A_{fs}. Consider the energy level $n=5$, which is the fundamental energy level of the valence electron of Rb, then the SO interaction breaks the degeneracy of the $L=0$ and $L=1$ components of this level into $5S_{1/2}$, $5P_{1/2}$, and $5P_{3/2}$. Notice that we are using spectroscopic notation, which is especially useful for this situation.

Spectroscopic notation is used to describe the energy levels of an atom and the transitions between them. The notation consists of three parts: the principal quantum number (n), the angular momentum quantum number (L), and the total angular momentum quantum number (J). It is the typical way to write down the state of an atom and it is particularly useful when dealing with fine structure energy levels. The general form is nL_j, where L is written as *S, P, D, F* for $L=0,1,2,3$. For atoms with more than one optically active electron, the number of spin states $2S+1$ is also depicted as a superscript after the principal quantum number. For alkalis, this number is always 2, so we choose to not write it down.

So far, we have neglected the nucleus spin, but the same type of coupling between orbital angular momentum and spin applies to it as well. This will lead to an even smaller energy structure called hyperfine energy structure. The strength of this energy structure splitting depends on the nuclear spin of the element and the energy level of the electron. In the case of rubidium, it will allow differentiating both naturally occurring isotopes, ^{85}Rb and ^{87}Rb, as the differences in the number of neutrons change the nucleus total spin.

We can express this coupling with the hamiltonian [44]

$$H_{hfs} = A_{hfs}\mathbf{I}\cdot\mathbf{J}, \tag{4}$$

where the physical parameters are within A_{hfs}. In this case, we go to a new basis $|n,J,I,F,m_F\rangle$ for which we redefine the total angular momentum to include the nucleus spin angular momentum

$$\mathbf{F} = \mathbf{J} + \mathbf{I}. \tag{5}$$

The form of the energy shift is very similar to the fine structure one, with the adequate changes of the angular momentum operators

$$\Delta E_{hfs} = \frac{A_{hfs}}{2}\left[F\left(F+1\right) - I\left(I+1\right) - J\left(J+1\right)\right]. \tag{6}$$

Once the energy structure of the alkalis is detailed, we can show the actual energy levels with the fine and hyperfine structure for the D_2 line of both rubidium isotopes in Figs. 1 and 2. We detail the two atomic species because there are some results of this work with one of them and some with the other. The following section's experiment also includes the 5D levels, which have their energy structure detailed in Ref. [45]. The so-called D_2 lines encopasses the transitions $5S_{1/2} \rightarrow 5P_{3/2}$ while the D_1 line is for transitions $5S_{1/2} \rightarrow 5P_{1/2}$.

The final energy structure within the scope of this work is the Zeeman sublevels. Consider an external weak magnetic field, that is, that can be treated as a perturbation to the hyperfine hamiltonian $\mu_b B < A_{hfs}$. Then, the effective hamiltonian for this interaction is

$$H_B = \mu_B g_F B F_z, \tag{7}$$

where μ_B is the Bohr magneton; g_F is the Landé factor; B the external magnetic field; and F_z the z-component of the total angular momentum F. The Landé g-factors are multiplicative terms in the Hamiltonians of the interaction of the atom with an external magnetic field and, in this case, are given by [46]

Figure 1 – Rubidium 85 D_2 transition hyperfine structure, with frequency splittings between the hyperfine energy levels. The approximate Landé g_F-factors for each level are also given, with the corresponding Zeeman splittings between adjacent magnetic sublevels.

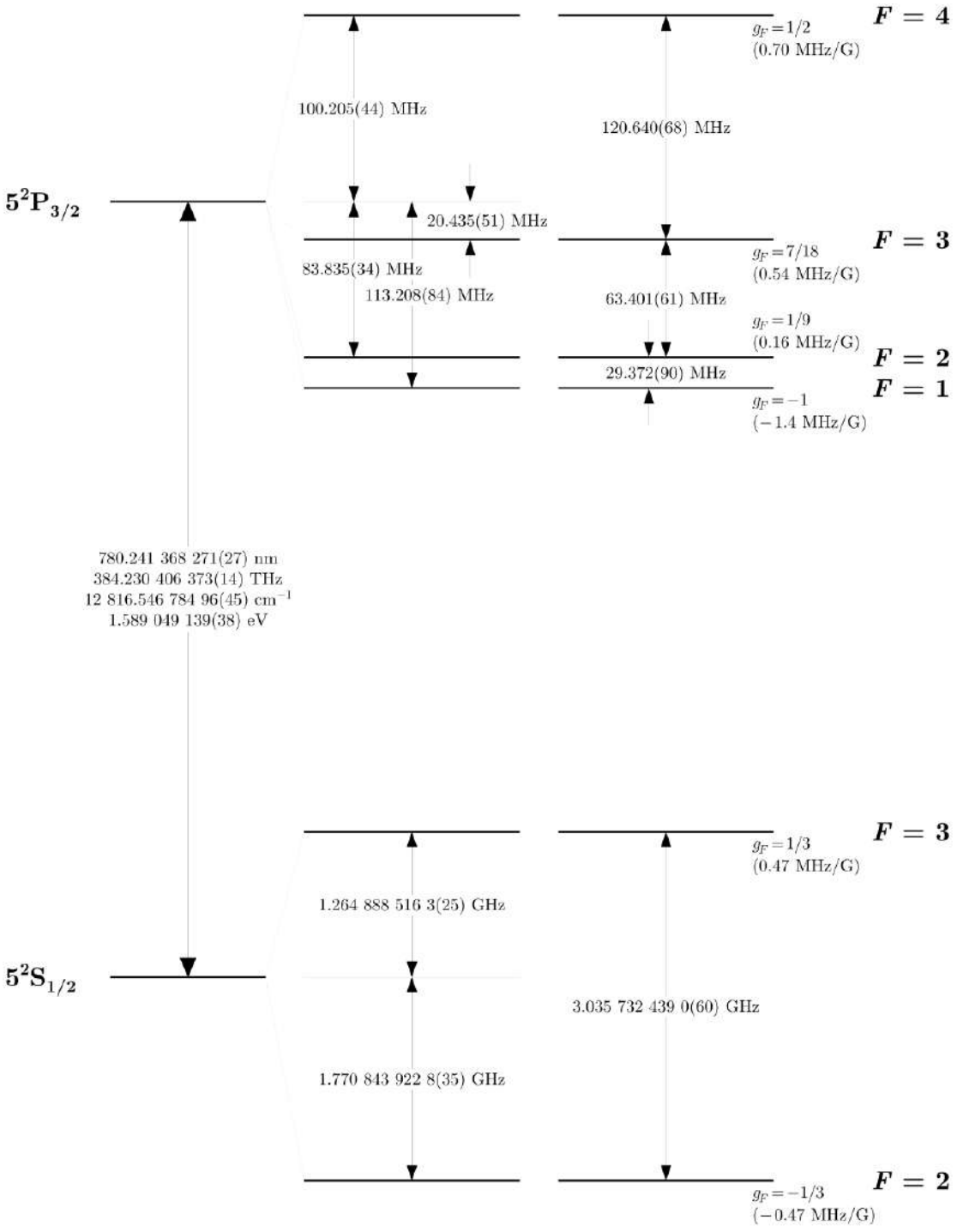

Source: Ref [46].

Figure 2 – Rubidium 87 D_2 transition hyperfine structure, with frequency splittings between the hyperfine energy levels. The approximate Landé g_F-factors for each level are also given, with the corresponding Zeeman splittings between adjacent magnetic sublevels.

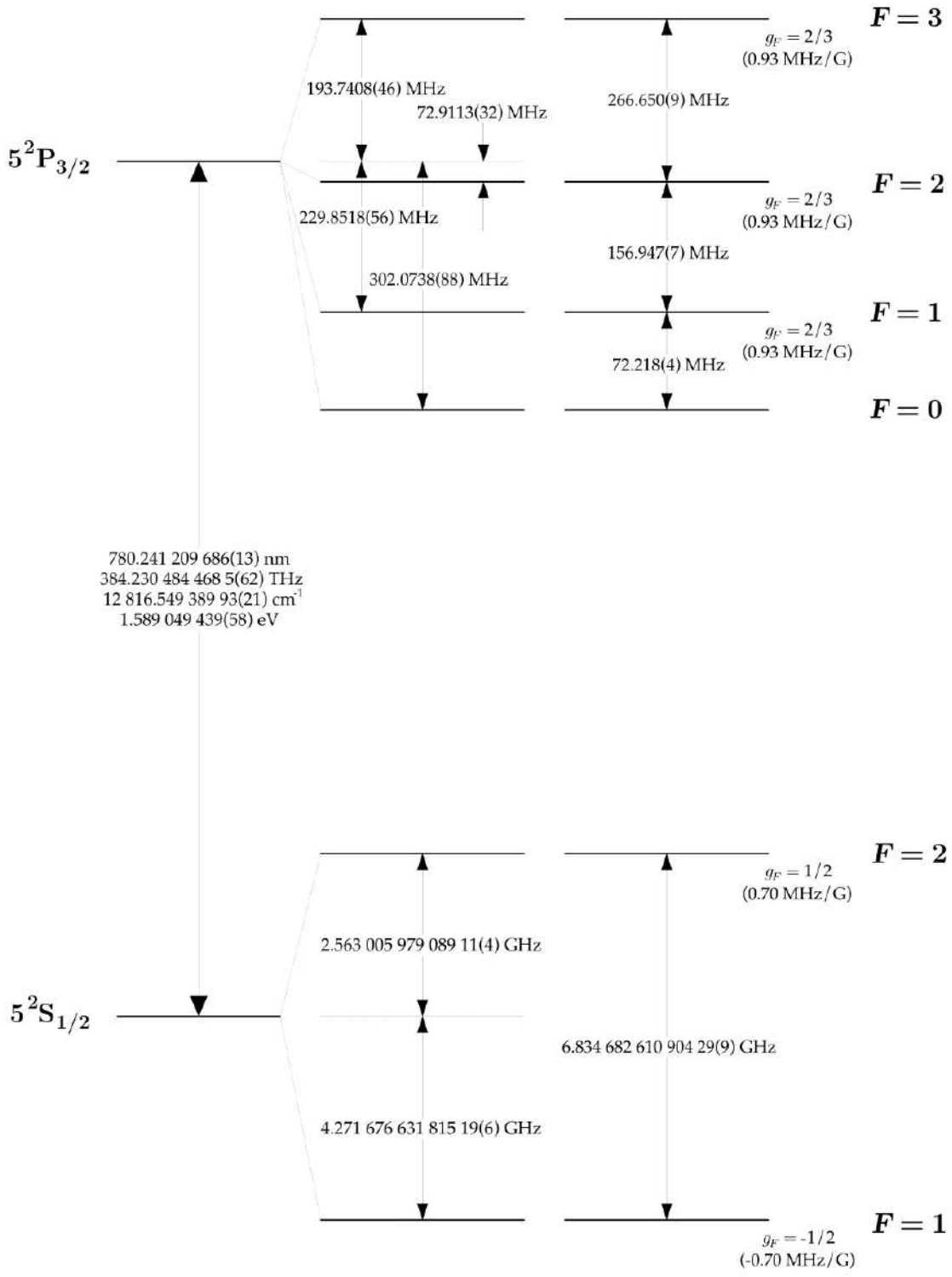

Source: Ref [46].

$$g_F \approx g_J \frac{F(F+1)-I(I+1)+J(J+1)}{2F(F+1)}, \tag{8}$$

$$g_J \approx 1+\frac{J(J+1)+S(S+1)-L(L+1)}{2J(J+1)}, \tag{9}$$

where we performed a few approximations, namely: neglect the nuclear term in g_F as it is a 0.1% correction and use the approximate values $g_S \approx 2$ and $g_L \approx 1$. This last g-factor might deviate from this approximation depending on the isotope or energy level due to multielectron or quantum electrodynamics (QED) [47] effects, so it is advisable to use experimentally obtained values.

Notice that, in this Zeeman effect scenario, the degeneracy of the sublevels within the hyperfine structure is lifted with each F hyperfine energy level containing $2F+1$ sublevels, labeled by m_F. This is of particular importance even when there is not an external magnetic field, due to the selection rules for transitions between these sublevels. We address this problem in more detail in section 4.

Finally, for a strong magnetic field, one must change the basis once again as the basis $|n,J,I,F,m_F\rangle$ that we used for describing the hyperfine structure is no longer adequate. In this case, we treat the hyperfine hamiltonian as a perturbation leading to different energy levels, in the so-called Paschen-Back regime [44].

2.2 Electromagnetic fields

After this brief description of the atomic systems used in the experiments of this work, it is time to look at the electromagnetic fields. The existence and behavior of electromagnetic waves within an atomic medium are dictated by Maxwell's equations [48]

$$\nabla \cdot \mathbf{D} = \rho, \tag{10}$$

$$\nabla \cdot \mathbf{B} = 0, \tag{11}$$

$$\nabla \times \mathbf{E} = -\frac{\partial \mathbf{B}}{\partial t}, \tag{12}$$

$$\nabla \times \mathbf{H} = \frac{\partial \mathbf{D}}{\partial t} + \mathbf{j}, \tag{13}$$

where ρ is the charge density and **j** is the free current density. The constitutive relations are

$$\mathbf{D} = \varepsilon_0 \mathbf{E} + \mathbf{P}, \tag{14}$$

$$\mathbf{B} = \mu_0 \mathbf{H} + \mathbf{M}, \tag{15}$$

where μ_0 is the vacuum magnetic permeability, $\mathbf{P}$ is the polarization, and $\mathbf{M}$ is the magnetization. There are a few simplifications that the neutral atomic samples we use allow: first, there are no free charges ($\rho = 0$) nor free currents ($\mathbf{j} = 0$); second, the material is nonmagnetic ($\mathbf{M} = 0$). This second condition connects to the fact that we will treat the interaction hamiltonian using the electric dipole term, as it is the most relevant one. With these considerations, it is rather simple to find the optical wave equation following the usual procedure of taking the curl of the Maxwell-Faraday equation (Eq. 12). Hence, we arrive at the partial differential equation (PDE)

$$\nabla^2 \mathbf{E} - \frac{1}{c^2}\frac{\partial^2}{\partial t^2}\mathbf{E} = \frac{1}{\varepsilon_0 c^2}\frac{\partial^2 \mathbf{P}}{\partial t^2}. \tag{16}$$

We must emphasize that in deriving this last PDE, we neglected the contribution of $\nabla(\nabla \cdot \mathbf{E})$ that comes from the vector identity for $\nabla \times \nabla \times \mathbf{E}$. Even though this term is only null for linear phenomena in isotropic media, it is usually very small in the nonlinear optics problems we are interested in here [49].

It is in the polarization, that is, the dipole moment per unit volume, that lies the description of the optical response in nonlinear optics phenomena. We can express it in a power series in terms of the electric field as

$$P = \varepsilon_0 \left(\chi^{(1)} E + \chi^{(2)} E^2 + \chi^{(3)} E^3 + \ldots \right), \tag{17}$$

where the coefficients $\chi^{(n)}$ are the n-th-order optical susceptibilities of the medium. Note that we considered the polarization $\mathbf{P}$ and electrical field $\mathbf{E}$ as scalars for simplicity. In general, $\chi^{(n)}$ is an $(n+1)$-th-rank tensor which represents both the polarization-dependent nature of the interaction and the symmetries of the nonlinear medium.

Figure 3 – Wave mixing processes described by Eq. 18 that can occur when two input waves interact in a medium characterized by a $\chi^{(3)}$ susceptibility.

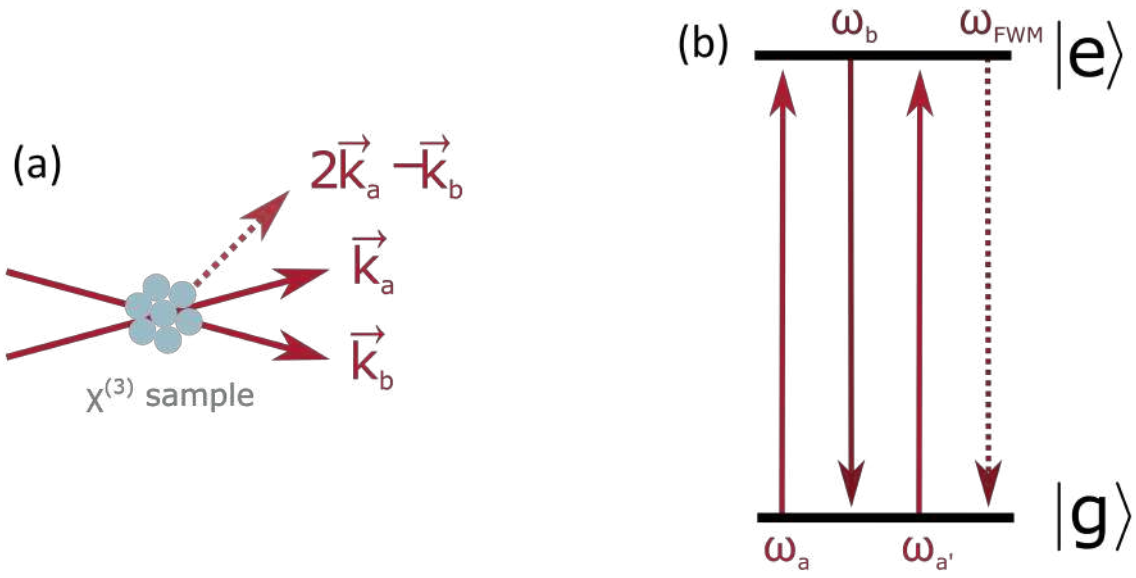

Source: The author (2023).

Atomic vapors are naturally centrosymmetric, hence they have a null second-order term, meaning that the first nonlinear term is the third-order term.

Consider then that two incident fields with frequency components ω_a and ω_b, with the latter being a weak field, interact with a $\chi^{(3)}$ medium. There will be several frequency combinations allowed to happen, but we are interested in the combination with frequency $2\omega_a - \omega_b$, that is, the FWM process frequency (see Fig. 3(a)).

FWM is a parametric nonlinear optical process that occurs when two photons of the field with frequency ω_a are annihilated while another photon is created in the weak field mode so that the nonlinear polarization associated with this phenomenon is

$$P(2\omega_a - \omega_b) = 3\varepsilon_0 \chi^{(3)} E_a^2 E_b^*. \tag{18}$$

The factor of 3 comes from the different field permutations that may contribute to this particular polarization term. With such polarization, a fourth photon is generated in the frequency of the FWM process to conserve energy and momentum. This process is depicted in the simple level scheme of Fig. 3(b).

This process we described is parametric because the system's initial and final quantum states are identical. A difference between parametric and nonparametric processes is that in the first case photon energy is always conserved, while this condition does not necessarily hold for the second process, since energy can be transferred to (or from) the medium.

Still, regarding the energy level structure, a very common configuration for the FWM process is the non-degenerate configuration, in which the incident fields are at different frequencies. This is the case we analyze in section 3. Another common configuration for the FWM process is the so-called degenerate configuration, in which all of the incident fields are at the same frequency. In this case, the generated fields will also be at the same frequency, with the direction and polarization dictated by the specific conditions of the experiment. We analyze a process such as this in sections 4 and 5.

One of the key factors that determine the efficiency of FWM is the phase-matching condition, which determines the direction of propagation of the generated fields. Phase-matching can be achieved either by adjusting the refractive index of the medium or by adjusting the angle of the incident fields. In some cases, it is also possible to achieve phase-matching by using an external field, such as an electric or magnetic field, to modify the energy levels of the atoms in the medium.

Finally, keep in mind that FWM is a process with typically very small efficiency. This means that it is usually necessary to use very high-intensity fields to obtain significant amounts of the generated fields. Hence, the generated fields are often very weak, and it can be challenging to detect them experimentally.

2.3 Bloch equations

Our final goal is to use the quantum mechanics formalisms to derive the atomic parameters that connect with the nonlinear optical susceptibilities. The idea is to express how the susceptibility depends on the atomic system's parameters such as dipole transition moments and energy levels. Moreover, by solving the equations of motion that we will find, we can make predictions of the numerical values of the nonlinear

response and model experimental results. These numerical results are typically reliable for the case of atomic vapors since the parameters of these systems (energy levels, dipole transition moments, decay rates, etc.) are often available in the literature with high accuracy.

To describe the dynamics of the atomic medium under the interaction with electromagnetic fields we must look for the equations of motion of this system. We have already provided a classical description of the fields, but the treatment of the atoms must follow the rules of quantum mechanics as depicted in the first subsection. Hence, let us briefly recapitulate the traditional quantum mechanics postulates and then build up the density-matrix formalism.

For a pure quantum system, at any time t_0, its state can be specified by the ket $|\psi(t_0)\rangle$, an element of the Hilbert space $\mathscr{H}$ [50]. An observable, that is, any measurable quantity, is a Hermitian operator $\hat{A}$ acting upon $\mathscr{H}$. When a measurement is performed, the possible outcomes are the eigenvalues of the observable $\hat{A}$ corresponding to that measurement. Moreover, the probability of obtaining an eigenvalue a_n is given by

$$p(a_n) = \sum_{k=1}^{g_n} \left| \langle \psi \left| u_n^k \right\rangle \right|^2, \tag{19}$$

where g_n is the degenerescence degree of the eigenvalue a_n and $\left|u_n^k\right\rangle$ represents the set of orthonormal kets of the degenerate subspace. We must be careful with these degeneracies especially in the context of this work, because of transitions in the hyperfine structure, as each level contains several Zeeman sublevels. The same probability can also be written in terms of a projector into the set of kets $\left|u_n^k\right\rangle$

$$p(a_n) = \langle \psi | P_n | \psi \rangle, \tag{20}$$

with the projector being $P_n = \sum_{k=1}^{g_n} \left|u_n^k\right\rangle \left\langle u_n^k\right|$. If the result of the measurement is a_n, the system abruptly evolves to a new state

$$\left|\psi'\right\rangle = \frac{P_n |\psi\rangle}{\sqrt{p(a_n))}}. \tag{21}$$

This type of measurement, called a projective measurement, causes the system state to evolve in time in this immediate way, referred to as the “collapse” of the wavefunction. There are other ways to extract information about the system state, but they are out of the scope of this text.

The temporal evolution of the system, when there is not a measurement happening, is given by the Schrödinger equation

$$i\hbar\frac{d}{dt}|\psi\rangle = \hat{H}(t)|\psi\rangle . \tag{22}$$

This completes the basic set of postulates that allows the description of quantum systems (for distinguishable particles). However, not all physical systems can be adequately described by these rules. A system that includes classical uncertainties can be seen as a statistical mixture of quantum states. The proper way to describe these systems is with the density operator $\hat{\rho}$. These operators must obey a few properties: (i) $Tr(\hat{\rho}) = 1$; (ii)$\hat{\rho}$ is Hermitian; (iii) its eigenvalues are non-negative. In particular, given that the density operator is Hermitian, there must be a spectral decomposition

$$\hat{\rho} = \sum_i p_i |\psi_i\rangle \langle\psi_i| , \tag{23}$$

where p_k represents the probability of finding the system in a certain state $|\psi_i\rangle$.

We must emphasize that the density operator is not in the Hilbert space but rather “acts” upon its vectors. Albeit that, it still represents the system state and is part of its own vectorial space with a defined internal product, the Hilbert-Schmidt space, with dimension N^2, for a Hilbert space of dimension N.

With these definitions of the density operator, we can still represent pure states, when it is possible to write $\hat{\rho}$ as a projector, $\hat{\rho} = |\psi\rangle\langle\psi|$. In this case, it is easy to see that $Tr(\hat{\rho}^2) = 1$. On the other hand, for a mixed state, or a non-pure state, $Tr(\hat{\rho}^2) < 1$.

The elements of the density operator have distinct meanings: the diagonal terms are the populations associated with the probability of finding the system in a certain state of the basis; the off-diagonal terms are called coherences and they represent the superposition of states.

One can obtain the temporal dynamics of the density operator through the Schrödinger equation. For simplicity, consider a time-independent hamiltonian:

$$\hat{\rho} = \sum_i p_i \left|\psi(t)\right\rangle \left\langle\psi(t)\right|, \tag{24}$$

$$= \sum_i p_i e^{-\frac{i}{\hbar}\hat{H}t} \left|\psi_0\right\rangle \left\langle\psi_0\right| e^{\frac{i}{\hbar}\hat{H}t}; \tag{25}$$

$$\therefore \frac{d\hat{\rho}}{dt} = -\frac{i}{\hbar}\hat{H}\hat{\rho} + \frac{i}{\hbar}\hat{\rho}\hat{H}, \tag{26}$$

$$= -\frac{i}{\hbar}\left[\hat{H}, \hat{\rho}\right]. \tag{27}$$

This is the Liouville-von Neumann equation and it applies to closed systems. However, the typical systems we want to address in this thesis are atoms interacting with light, which are naturally open systems. A very clear example of that is the coupling between the atomic states and vacuum modes that induces spontaneous decay [51]. The alternative approach, under a few considerations, is the Lindblad equation, from which we may derive the dynamics of open quantum systems. However, a faster (and more suited to the scope of this work) approach is to add these decay terms phenomenologically

$$\frac{d\hat{\rho}}{dt} = -\frac{i}{\hbar}\left[\hat{H}, \hat{\rho}\right] + \left.\frac{\partial\hat{\rho}}{\partial t}\right|_{relax}. \tag{28}$$

Once these terms are added we have the optical Bloch equations [52], that is, the equations of motion for an atomic system interacting with an electromagnetic field.

As an example, that sets the path of the following sections models, let us obtain the optical Bloch equations of a three-level system interacting with two input fields. There are three possible arrangements for such a system: a cascade system, in which there is a ground, an intermediate, and an excited state; the Λ system, with two ground states and a shared excited state; the V state, which is the opposite of the Λ, that is, two excited states and a common ground state. These systems are depicted in Fig. 4.

The total hamiltonian of the system is:

$$\hat{H} = \hat{H}_0 + \hat{H}_{int}, \tag{29}$$

Figure 4 – Possible arrangements for a three-level system: (a) cascade; (b) Λ; (c) V configuration.

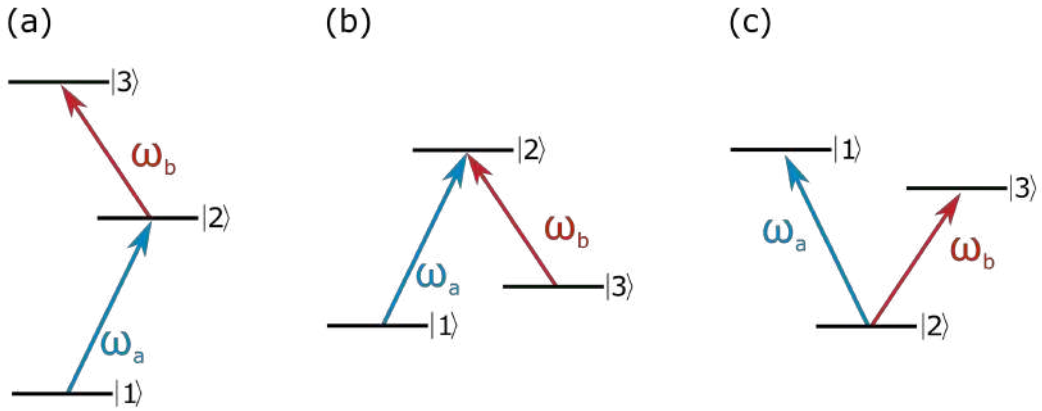

Source: The author (2023).

where $\hat{H}_0$ is the free atom hamiltonian given by

$$\hat{H}_0 = \hbar \left[\omega_1 |1\rangle \langle 1| + \omega_2 |2\rangle \langle 2| + \omega_3 |3\rangle \langle 3| \right], \tag{30}$$

while for the interaction hamiltonian we consider only the electric dipole term:

$$\hat{H}_{int} = -\sum_j e\vec{r} \cdot \mathbf{E}_j, \tag{31}$$

where $j = a, b$. The electric fields can be written as:

$$\mathbf{E}_a = \left[\varepsilon_a(t) e^{-i(\omega_a t - \mathbf{k}_a \cdot \mathbf{r} + \phi_a)} + c.c. \right] \mathbf{e}_a; \tag{32}$$

$$\mathbf{E}_b = \left[\varepsilon_b(t) e^{-i(\omega_b t - \mathbf{k}_b \cdot \mathbf{r} + \phi_b)} + c.c. \right] \mathbf{e}_b, \tag{33}$$

where $\varepsilon_{a,b}$ are the electric field amplitudes; $\omega_{a,b}$ are the angular frequencies of each input field; $\mathbf{k}_{a,b}$ are the wavevectors; $\phi_{a,b}$ represent the phases; and $\mathbf{e}_{a,b}$ are the polarization unit vectors. A few remarks are due at this point. First, given the choice of our representation of these fields with their complex amplitudes, the real representation of the field must have a multiplicative factor of 2, that is, $E_j \approx 2\cos\left(\omega_j t - k_j z + \phi_j\right)$. Moreover, we are considering that the fields have wavevectors in the z-direction, eliminating transversal components. We will see that our experimental setup will not always obey

this consideration. Finally, for most of this thesis, we will neglect the phase of the input fields, including now. However, in the last section, this phase plays a crucial role in understanding the relevant phenomena.

We define the Rabi frequency and the transition dipole moment as:

$$\Omega_j \equiv \frac{\mu_{np}\varepsilon_j}{\hbar}; \tag{34}$$

$$\mu_{np} \equiv e\left\langle n\left|\mathbf{r}\cdot\mathbf{e}_j\right|p\right\rangle. \tag{35}$$

Our first task is to calculate all the elements of the interaction hamiltonian. First, notice that all elements in the main diagonal are zero, for there is no dipole interaction of a level with itself. To calculate the off-diagonal terms we move to a rotating frame, which eliminates one of the complex components to avoid fast-spinning terms in the next steps of the derivation. We are doing this simplification at this point to avoid carrying the cumbersome complex notation. The interaction hamiltonian is then

$$\hat{H}_{int} = -\hbar\begin{pmatrix} 0 & \tilde{\Omega}_a^* e^{i\omega_a t} & 0 \\ \tilde{\Omega}_a e^{-i\omega_a t} & 0 & \tilde{\Omega}_b e^{-i\omega_b t} \\ 0 & \tilde{\Omega}_b^* e^{i\omega_b t} & 0 \end{pmatrix}. \tag{36}$$

We incorporated the spatial part of the electric field into the Rabi frequencies, that is $\tilde{\Omega}_j = \Omega_j e^{ik_j z}$. Finally, to write down the total hamiltonian, we shift the energy levels by the energy of level $|1\rangle$

$$\hat{H} = -\hbar\begin{pmatrix} 0 & \tilde{\Omega}_a^* e^{i\omega_a t} & 0 \\ \tilde{\Omega}_a e^{-i\omega_a t} & -\omega_{21} & \tilde{\Omega}_b e^{-i\omega_b t} \\ 0 & \tilde{\Omega}_b^* e^{i\omega_b t} & -\omega_{31} \end{pmatrix}, \tag{37}$$

where we used the definition $\omega_{np} = \omega_n - \omega_p$.

Let us use the Liouville-von Neumann equation (see Eq. 27) to obtain the density-matrix elements. For now, we will overlook the relaxation terms. By using the completeness relations of the system:

$$\dot{\rho}_{np} = \frac{i}{\hbar}(\rho_{n1}H_{1p} + \rho_{n2}H_{2p} + \rho_{n3}H_{3p} - \rho_{1p}H_{n1} - \rho_{2p}H_{n2} - \rho_{3p}H_{n3}) \tag{38}$$

Given that, the populations and coherences are:

$$\dot{\rho}_{11} = \frac{i}{\hbar}(\cancel{\rho_{11}H_{11}} + \rho_{12}H_{21} + \cancel{\rho_{13}H_{31}} - \cancel{\rho_{11}H_{11}} - \rho_{21}H_{12} - \cancel{\rho_{31}H_{13}}); \tag{39}$$

$$\dot{\rho}_{22} = \frac{i}{\hbar}(\rho_{21}H_{12} + \cancel{\rho_{22}H_{22}} + \rho_{23}H_{32} - \rho_{12}H_{21} - \cancel{\rho_{22}H_{22}} - \rho_{32}H_{23}); \tag{40}$$

$$\dot{\rho}_{33} = \frac{i}{\hbar}(\cancel{\rho_{31}H_{13}} + \rho_{32}H_{23} + \cancel{\rho_{33}H_{33}} - \cancel{\rho_{13}H_{31}} - \rho_{23}H_{32} - \cancel{\rho_{33}H_{33}}); \tag{41}$$

$$\dot{\rho}_{21} = \frac{i}{\hbar}((\rho_{22} - \rho_{11})H_{21} + \rho_{21}(H_{11} - H_{22}) - \rho_{31}H_{23} + \cancel{\rho_{23}H_{31}}); \tag{42}$$

$$\dot{\rho}_{31} = \frac{i}{\hbar}(-\cancel{\rho_{11}H_{31}} - \rho_{21}H_{32} + \rho_{31}(H_{11} - H_{33}) + \rho_{32}H_{21} + \cancel{\rho_{33}H_{31}}); \tag{43}$$

$$\dot{\rho}_{23} = \frac{i}{\hbar}(-\cancel{\rho_{21}H_{13}} + (\rho_{22} - \rho_{33})H_{23} + \rho_{23}(\rho_{22} - \rho_{33}) - \rho_{13}H_{21}). \tag{44}$$

The missing off-diagonal terms are the complex conjugate of the ones presented. Rearranging and substituting the hamiltonian elements:

$$\dot{\rho}_{11} = -i\left(\rho_{12}\tilde{\Omega}_a e^{-i\omega_a t} - \rho_{21}\tilde{\Omega}_a^* e^{i\omega_a t}\right); \tag{45}$$

$$\dot{\rho}_{22} = -i\left(\rho_{21}\tilde{\Omega}_a^* e^{i\omega_a t} - \rho_{12}\tilde{\Omega}_a e^{-i\omega_a t} + \rho_{23}\tilde{\Omega}_b^* e^{i\omega_b t} - \rho_{32}\tilde{\Omega}_b e^{-i\omega_b t}\right); \tag{46}$$

$$\dot{\rho}_{33} = -i\left(\rho_{32}\tilde{\Omega}_b e^{-i\omega_b t} - \rho_{23}\tilde{\Omega}_b^* e^{i\omega_b t}\right); \tag{47}$$

$$\dot{\rho}_{21} = -i\left((\rho_{22} - \rho_{11})\tilde{\Omega}_a e^{-i\omega_a t} + \rho_{21}\omega_{21} - \rho_{31}\tilde{\Omega}_b e^{-i\omega_b t}\right); \tag{48}$$

$$\dot{\rho}_{31} = -i\left(-\rho_{21}\tilde{\Omega}_b^* e^{i\omega_b t} + \rho_{31}\omega_{31} + \rho_{32}\tilde{\Omega}_a e^{-i\omega_a t}\right); \tag{49}$$

$$\dot{\rho}_{23} = -i\left((\rho_{22} - \rho_{33})\tilde{\Omega}_b e^{-i\omega_b t} + \rho_{23}(-\omega_{21} + \omega_{31}) - \rho_{13}\tilde{\Omega}_a e^{-i\omega_a t}\right). \tag{50}$$

At this point, we introduce the slow variables of the system to later eliminate explicit time dependence. Let us define the slow coherences:

$$\rho_{12} = \sigma_{12}e^{i\omega_a t}; \tag{51}$$

$$\rho_{13} = \sigma_{13}e^{i(\omega_a - \omega_b)t}; \tag{52}$$

$$\rho_{32} = \sigma_{32}e^{i\omega_b t}. \tag{53}$$

These choices of frequencies in which the system frame may rotate are intentional, as we are looking for a very simple description of the interaction in the low-intensity regime. We can use the equations that follow to approximate higher-order responses. A more rigorous (and complicated) treatment would be to write these coherences as a Floquet expansion, allowing the system to oscillate in any combination of the input fields frequencies [53].

With these definitions, we rewrite the density-matrix elements:

$$\dot{\rho}_{11} = -i\sigma_{12}\tilde{\Omega}_a + i\sigma_{21}\tilde{\Omega}_a^*; \tag{54}$$

$$\dot{\rho}_{22} = -i\sigma_{21}\tilde{\Omega}_a^* + i\sigma_{12}\tilde{\Omega}_a - i\sigma_{23}\tilde{\Omega}_b^* + i\sigma_{32}\tilde{\Omega}_b; \tag{55}$$

$$\dot{\rho}_{33} = -i\sigma_{32}\tilde{\Omega}_b + i\sigma_{23}\tilde{\Omega}_b^*; \tag{56}$$

$$\dot{\sigma}_{21} = i\delta_a\sigma_{21} - i\left(\rho_{22} - \rho_{11}\right)\tilde{\Omega}_a + i\sigma_{31}\tilde{\Omega}_b; \tag{57}$$

$$\dot{\sigma}_{31} = i\left(\Delta - \omega_{31}\right)\sigma_{31} + i\sigma_{21}\tilde{\Omega}_b^* - i\sigma_{32}\tilde{\Omega}_a; \tag{58}$$

$$\dot{\sigma}_{23} = i\left(\delta_b - \omega_{31}\right)\sigma_{23} - i\left(\rho_{22} - \rho_{33}\right)\tilde{\Omega}_b + i\sigma_{13}\tilde{\Omega}_a. \tag{59}$$

We have defined the detunings as

$$\delta_a \equiv \omega_a - \omega_{21}; \tag{60}$$

$$\delta_b \equiv \omega_b - \omega_{23}; \tag{61}$$

$$\Delta \equiv \omega_a - \omega_b. \tag{62}$$

At this point, our description of the atom-light interaction is still missing the decay rates. To add them properly we must choose which type of three-level system we want to address. For this example, let us detail the case of the Λ system (see Fig. 4(b)), in which the population of the excited state can decay to each one of the ground states. Population decay rates will be represented by Γ_{np} while coherence decay rates will be γ_{np}. Hence, the final set of optical Bloch equations is

$$\dot{\rho}_{11} = -i\sigma_{12}\tilde{\Omega}_a + i\sigma_{21}\tilde{\Omega}_a^* + \Gamma_{21}\rho_{22}; \tag{63}$$

$$\dot{\rho}_{22} = -i\sigma_{21}\tilde{\Omega}_a^* + i\sigma_{12}\tilde{\Omega}_a - i\sigma_{23}\tilde{\Omega}_b^* + i\sigma_{32}\tilde{\Omega}_b - (\Gamma_{21} + \Gamma_{23})\,\rho_{22}; \tag{64}$$

$$\dot{\rho}_{33} = -i\sigma_{32}\tilde{\Omega}_b + i\sigma_{23}\tilde{\Omega}_b^* + \Gamma_{23}\rho_{22}; \tag{65}$$

$$\dot{\sigma}_{21} = (i\delta_a - \gamma_{21})\,\sigma_{21} - i\,(\rho_{22} - \rho_{11})\,\tilde{\Omega}_a + i\sigma_{31}\tilde{\Omega}_b; \tag{66}$$

$$\dot{\sigma}_{31} = (i\Delta - i\omega_{31} - \gamma_{31})\,\sigma_{31} + i\sigma_{21}\tilde{\Omega}_b^* - i\sigma_{32}\tilde{\Omega}_a; \tag{67}$$

$$\dot{\sigma}_{23} = (i\delta_b - i\omega_{31} - \gamma_{23})\,\sigma_{23} - i\,(\rho_{22} - \rho_{33})\,\tilde{\Omega}_b + i\sigma_{13}\tilde{\Omega}_a. \tag{68}$$

We chose a very general form for the decay rates. However, different processes may require different decay terms, for example, the decay rate that could be introduced due to the finite time of interaction between the input field and the atoms.

The treatment we have built so far assumes that all the atoms in a sample can be described by the same set of equations. However, there are scenarios in which some groups of atoms might have different interactions than others. The most common effect that causes this is Doppler-broadening, a type of inhomogeneous broadening. In this case, the detuning is a function of the atom's velocity, which on the other hand is given by the Maxwell-Boltzmann distribution for an atomic vapor. We treat the Doppler-broadening in sections 3 and 4 in more detail.

Let us look for solutions to the set of Eqs. 63-68 in the steady-state. In this case, the time derivatives are set to zero and we are left with a system of linear equations. It is possible to solve them analytically [54], but the solution is quite cumbersome. We opt at this moment to solve them numerically using Gaussian elimination. To do so, we write the set of Eqs. 63-68 in a matrix form and then solve for the density-matrix elements using a linear algebra suite (*Wolfram Mathematica 12.0*). The program containing this solution is in appendix A.

An interesting phenomenon that this system allows us to explore is electromagnetically induced transparency (EIT), a phenomenon in which the transmission of light through an optically dense medium is suppressed by the application of a control laser beam. It occurs in atomic systems such as the one we are modeling in this example. Interference between the two input fields exciting the atoms creates a "dark state" which

Figure 5 – Transmission signal as a function of the probe field detuning. (a) $\Omega_a = 0.5\Gamma$, (b) $\Omega_a = 5\Gamma$. The two graphs are normalized independently.

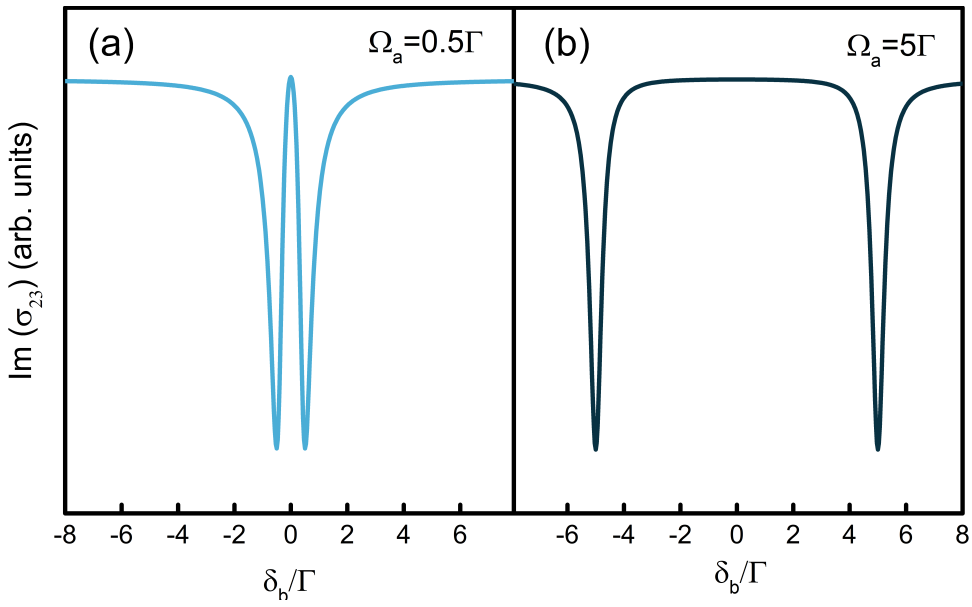

Source: The author (2023).

leads to a suppression of the probe light transmission through the medium. It was first observed in the late 1980s [55, 56] and it has since been abundantly studied.

Consider then that the a field (control) has a fixed detuning $\delta_a = 0$ in the transition $|1\rangle \rightarrow |2\rangle$, and we scan the frequency of the b field (probe) in the transition $|3\rangle \rightarrow |2\rangle$. Moreover, we consider $\Gamma_{21} = \Gamma_{23} = \Gamma$. The b field is set to be very weak ($\Omega_b = 0.01\Gamma$). Finally, for a thin sample, that is, with a length smaller than the Rayleigh length of the input lasers, we can approximate the imaginary part of the coherence σ_{23} as the transmission of the b field. We detail this particular approximation in section 5 where we will use it again. The other decay rates come from Refs. [46, 45]. With all of these considerations, we plot the transmission $T_b \approx \text{Im}(\sigma_{23})$ as a function of the detuning δ_b in Fig. 5.

In Fig. 5(a) the control field has a Rabi frequency equal to half the natural linewidth, that is, $\Omega_a = 0.5\Gamma$. Near resonance, the probe field is absorbed as expected. However, on resonance, there is a narrow peak indicating that the probe field is no longer absorbed, showing the EIT phenomenon. On the hand, in Fig. 5(b) we increased the Rabi frequency of the control field tenfold, rendering a completely different transmission curve. The once thin peak that indicated the EIT phenomenon is no longer present and we see a doublet structure. This is a characteristic signature of the Autler-Townes

splitting, our main focus in section 3. For now, it is sufficient to say that for strong fields, the excited level is split into two different levels. These two levels are separated enough to distinguish the excitation routes, eliminating the interference once responsible for the EIT and rendering two well-separated peaks. The transition between EIT and AT splitting is still nowadays a topic of interest [57, 58]. A final comment is about how the two peaks are separated by $2\Omega_a$. This separation might change considerably depending on the Doppler-broadening and the geometric arrangement of the experiment, as we detail in the following section.

This simple example described here sets the first steps of the modeling of the actual experimental results of this thesis. We will in the following sections introduce phenomena connected to the Doppler broadening, the geometry of the nonlinear process, or even the stochastic phase of the input fields. Overall, the route to obtaining the equations of motion and eventually the final output signals follow the procedure shown here but with the proper adaptations to each situation.

3 COHERENT BLUE LIGHT GENERATION IN A DOPPLER-BROADENED FOUR-WAVE MIXING PROCESS

In this section, we present our results on the coherent blue light (CBL) generation via four-wave mixing (FWM) in a hot vapor of rubidium atoms using a combination of a cw diode laser and a 1 GHz femtosecond pulse train. Special atention is directed towards two aspects of the problem: an analysis of the Autler-Townes (AT) splitting of the CBL signal [59] and an interference effect between FWM excitation routes [60].

We obtain the CBL signal by scanning the cw laser frequency or the repetition rate of the pulsed laser. In both scenarios, there is an AT splitting with a large separation in the doublet structure due to the configuration of copropagating fields. We will see that this is in opposition to the typical result found in the literature for AT splitting which scales with the Rabi frequency. Moreover, if one scans the repetition rate of the femtosecond pulse train in a specific region of values, the spectra present a narrow peak, which we interpret as a sign of the interfering pathways of excitation. We model both results, the interference pattern and the AT splitting, employing the density matrix formalism to write the Bloch equations and solve them numerically. For the interference effect, the solution shows that the narrow peak appears only when both lasers are resonant with one- and two-photon transitions for the same atomic velocity group. As for the AT splitting, we use the model to detail cases beyond the experimental setup, comparing, for instance, the fluorescence and the FWM signal for homogeneously and non-homogeneously broadened systems. We also study how the AT splitting behaves if one scans the strong or the weak laser beam.

3.1 Optical pulse train

For the experiment described in this section, we use a combination of continuous and pulsed laser sources. In order to proceed, we first provide some details about the pulsed laser and how it interacts with the atomic vapor. A mode-locked pulsed laser is a sequence of optical pulses with a well-defined phase relationship separated by a constant time interval. These lasers are said to be mode-locked and can produce a

series of extremely short, intense pulses of light at a very high repetition rate. These pulses are typically on the order of picoseconds or femtoseconds in duration and can be generated at repetition rates up to several gigahertz.

Mode-locked lasers are used in a variety of applications, including spectroscopy, time and frequency metrology, and optical communication [61]. The basic principle of mode-locking is to create a feedback loop within the laser cavity that locks the phase of the laser's output field to a specific value. This can be achieved by using a nonlinear element, such as a saturable absorber or a Kerr cell, to modulate the gain of the laser. When the gain of the laser is modulated in this way, it creates a series of pulses that are evenly spaced in time.

One of the key features of mode-locked lasers arises in the frequency domain since they generate a series of equally spaced frequency components, known as a frequency comb. A frequency comb is a periodic array of equally spaced frequencies that can be used as a very precise frequency ruler. One of the main advantages of frequency combs is their ability to provide a highly precise and stable frequency reference, when locked into a frequency pattern. This makes them ideal for applications where high accuracy and stability are required, such as in spectroscopy and time and frequency metrology [62]. In spectroscopy, frequency combs can be used to precisely measure the absorption or emission spectrum of a sample, and to detect extremely small differences in the frequencies of the absorbed or emitted light.

Frequency combs are also employed in optical communication systems to transmit large amounts of data over long distances. In these systems, the frequency comb is used to generate a series of optical carriers at different frequencies, transmitting data with a technique known as wavelength division multiplexing (WDM) [63]. In turn, WDM systems are used to transmit multiple optical signals over a single fiber by using different wavelengths for each signal and are widely common in modern communication systems.

In our experiment, we have a mode-locked Ti:sapphire laser (BR Labs Ltda), which emits 100 fs pulses at a 1 GHz repetition rate, with a maximum output average power of 500 mW, and a 20 nm bandwidth centered near 776 nm. It is helpful to analyze

Figure 6 – Diagrammatic representation of a pulse train in the time domain and its respective Fourier transform.

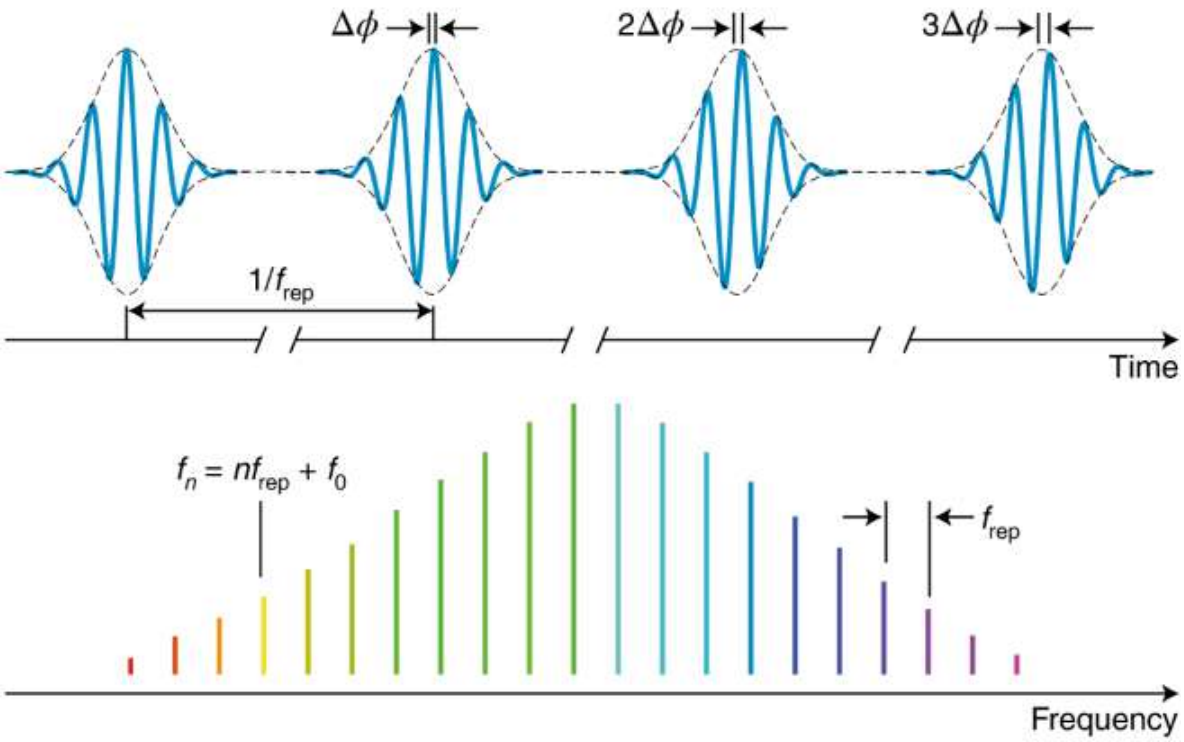

Source: Ref. [62].

the mathematical description of such a laser source. Consider the electric field [64]:

$$E_{fs}(t) = \sum_{n=0}^{N-1} \varepsilon_{fs}(t - nT_R) e^{-i(\omega_{fs}t - n\omega_{fs}T_R + n\Delta\phi)}, \tag{69}$$

where, $\varepsilon_{fs}(t)$ is the pulse envelope of the fs field; T_R is the repetition period; N is the number of pulses; ω_{fs} is the frequency of the carrier wave; and $\Delta\phi$ is the phase difference between each pulse, introduced by optical elements within the laser cavity.

This train of ultrashort pulses can be thought of as a frequency comb if one describes the electric field amplitude in the frequency domain. Therefore, taking the Fourier transform of Eq. 69 renders:

$$\tilde{E}_{fs}(\omega) = \tilde{\varepsilon}_{fs}(\omega - \omega_{fs}) \sum_{m=0}^{N-1} e^{-im(\omega T_R - \Delta\phi)}. \tag{70}$$

A representation of the pulses and frequency modes is provided Fig. 6. Notice that, in this representation, the modes are depicted as thin lines. The actual width of each frequency mode is $\approx 1/NT_R$. Therefore, the modes are thinner as the number of

pulses increases. In the limit $N \to \infty$:

$$\tilde{E}_{fs}(\omega) = 2\pi\tilde{\varepsilon}_{fs}(\omega - \omega_{fs}) f_R \sum_{m=-\infty}^{\infty} \delta(\omega - \omega_m), \tag{71}$$

in which

$$\omega_m = 2\pi(f_0 + m f_R), \tag{72}$$

where we consider $\Delta\phi f_R = 2\pi f_0$; the repetition rate is defined as $1/T_R \equiv f_R$; ω_m is the frequency of the mth mode of the frequency comb; and f_0 is the so-called offset frequency.

Finally, the number of modes in the frequency comb is of special interest. In our case, for $f_R = 1$ GHz and 100 fs pulses, there are about 10^4 frequency modes in our laser. This repetition rate is measured with a photodiode and phase locked to a signal generator (E8663B-Agilent), with 1 Hz resolution, using a cavity mirror mounted on a piezoelectric transducer (PZT) allowing to scan f_R. The carrier-envelope-offset frequency, f_0, is free running.

In terms of application, we are interested in employing this type of pulsed laser to perform spectroscopic measurements. In particular, when a frequency comb with such a high repetition rate interacts with an atomic medium, the necessary conditions for the coherent accumulation [65] are fulfilled since the atomic relaxation time is much larger than the time interval between pulses. In addition, for this 1 GHz repetition rate, only one or two modes lie within the Doppler width, which allows the treatment of the pulsed laser as a series of continuous modes that interact with the atoms. This is critical to the results we present here and how we model them. For instance, some works perform spectroscopy taking advantage of this, distinguishing the different hyperfine levels and investigating the coherent processes induced by the train of ultrashort pulses [66, 67].

In fact, one can employ different types of spectroscopy using a combination of this high-repetition-rate pulsed laser and a cw laser. That is, the repetition rate of the fs laser is fixed and the different atomic velocity groups are selected as the frequency of the diode laser is scanned. This technique is called velocity-selective spectroscopy [68]. On the other hand, we can scan the repetition rate itself and fix the diode frequency, leading to a case in which a specific group of atoms is probed each time.

3.2 CBL experimental setup

Our initial goal with this experiment was to extend a previous study of the CBL generated in rubidium vapor, now using our 1 GHz pulse train instead of the previous 100 MHz pulse train [67]. This change in parameters, increasing the frequency separation between the optical modes, allows us to easily distinguish the blue signal generated by each mode of the frequency comb. Consequently, the results resemble those obtained using two cw diode lasers [69]. However, we will show that the combination of pulsed and continuous lasers allows the observation of a few novel effects, such as the interference between excitation routes.

A diagrammatic representation of the experiment is depicted in Fig. 7, together with the relevant energy levels in the center. For simplicity we label the levels $5S_{1/2}$, $5P_{3/2}$, $5D_{5/2}$, and $6P_{3/2}$ as $|1\rangle$, $|2\rangle$, $|3\rangle$, and $|4\rangle$, respectively. We use a mode-locked Ti:sapphire laser, with the parameters already described, together with a diode laser stabilized in temperature and with a linewidth of about 1 MHz. This linewidth is much smaller than the hot Rb Doppler linewidth (of hundreds of MHz). The cw laser has a transverse mode TEM_{00} with a 0.7 mm beam waist, while the fs laser has a beam waist of 0.6 mm, both measured at the Rb cell position with a CCD camera.

The two beams have parallel circular polarizations obtained with polarizing beam-splitters (PBS) and quarter-wave plates. These beams are aligned in a copropagating configuration and pass through a 5 cm long cell containing natural Rb heated up to $\approx 100\,^{o}$C. Throughout the measurements, the average power of the fs laser is fixed at 250 mW ($\approx$ 7 W/cm^2) while the power of the diode laser varied from 0.070 up to 4.5 mW (1.4 to 90 mW/cm^2), both values acquired at the cell entrance. With a set of lenses, we focused both beams in the center of the cell to increase the intensity, collecting them after the Rb cell with another lens.

The two copropagating beams, at 780 nm (cw) and 776 nm (fs), drive each step of the two-photon transition $5S_{1/2} \rightarrow 5P_{3/2} \rightarrow 5D_{5/2}$ of ^{85}Rb. Since these input beams have circular polarizations, there is a significant optical pumping whitin the Zeeman sublevel structure. Hence, the excitation process only happens in states with the highest m_F. Moreover, if the repetition rate of the pulsed laser is chosen very carefully, there

Figure 7 – Experimental setup with relevant energy levels of ^{85}Rb. BS, L, M, PBS, PMT, and SAS indicate beam-splitter, lens, mirror, polarizer beam-splitter, photomultiplier, and saturated absorption spectroscopy, respectively.

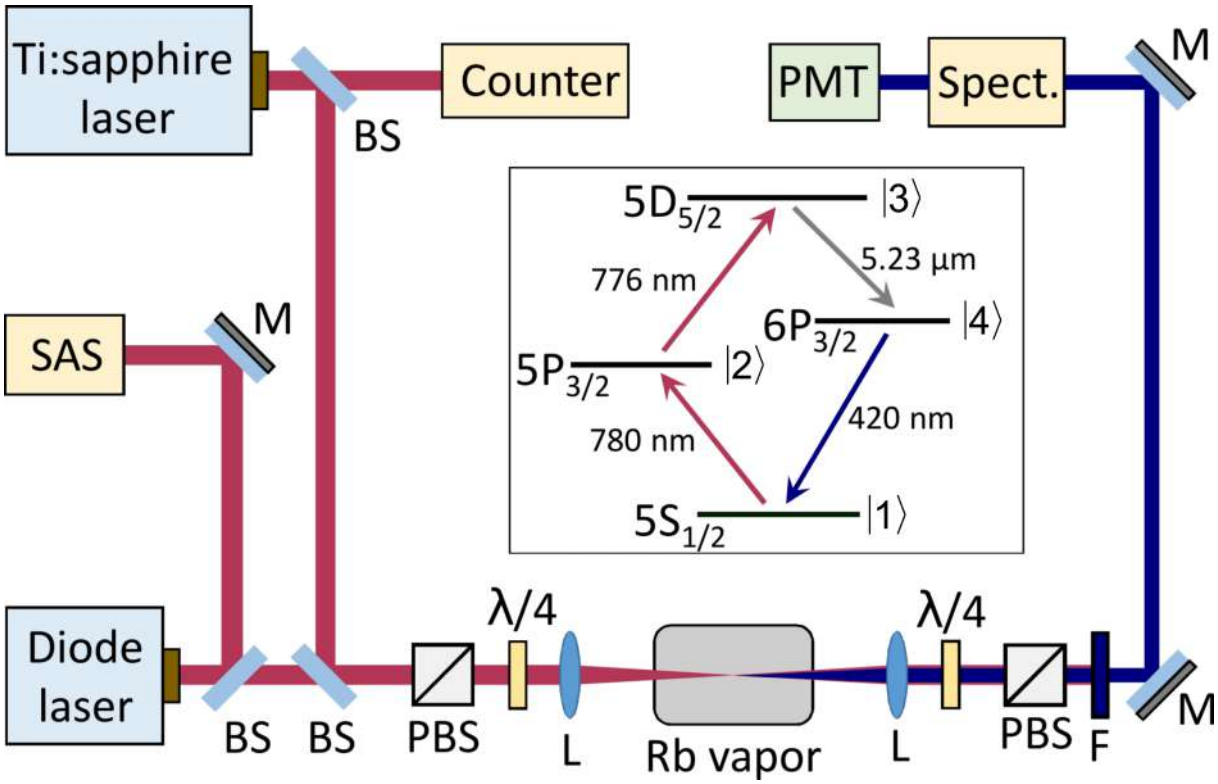

Source: Ref. [60].

will also be a frequency mode in the first transition $5S_{1/2} \rightarrow 5P_{3/2}$, but in this initial description, we do not consider this case.

The combination of both lasers exciting the two-photon transition, together with quantum fluctuations, is sufficient to induce a parametric process [70]. Hence, there is an induced coherence between the levels $5S_{1/2}$ and $6P_{3/2}$, leading to the generation of new light beams at 5.23 μm (mid-infrared) and 420 nm (blue). The infrared field undergoes the process of amplified spontaneous emission (ASE) but it cannot be detected as it is absorbed by the pyrex cell that holds the vapor. Our main focus is on the blue signal generated through the FWM process. This CBL signal is selected using a blue bandpass filter and diffraction gratings to, only then, be sent into a photomultiplier tube and recorded by an oscilloscope.

Figure 8 – Simplified scheme of the saturated absorption spectroscopy. OI, BS and ND are optical isolators, beam-splitters, and neutral density filters, respectively.

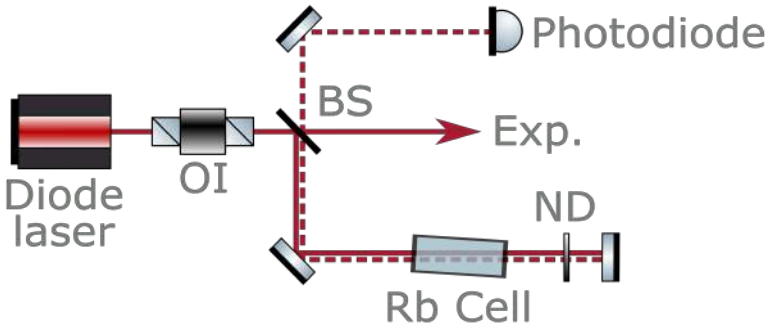

Source: The author (2023).

3.2.1 Saturated absorption spectroscopy

In Fig. 7 we show that part of the light of the diode laser is taken to a saturated absorption spectroscopy (SAS) experiment. Let us detail this experimental technique and its importance to our experiments.

The diode laser frequency can be tuned in a range of about 10 GHz by changing the injection current of the laser head. Therefore, we can choose which rubidium isotope we want to study. However, most of our results are with ^{85}Rb, since this isotope renders larger signals. It is crucial to monitor the frequency of the diode laser and to do so we use the results of SAS.

The SAS setup is shown in the simplified scheme of Fig. 8. Only a small fraction of the laser power is necessary to perform the SAS, so we use a microscope slide to divide the beam into two parts. The stronger beam goes to the CBL experiment, while the weaker is used in the SAS.

This experimental method, a well-known type of Doppler-free spectroscopy, uses a pair of counter-propagating beams to distinguish the hyperfine levels of an atomic vapor. These beams are called pump and probe, the latter being less intense, and they interact, in our system, with a sample of rubidium atoms. Both vapor cells, the reference one in the SAS setup and the one in the CBL setup, contain the two stable isotopes of rubidium in natural abundance, i.e. 72.2% of ^{85}Rb and 27.8% of ^{87}Rb.

Separately, the pump and probe beam absorption lines in the atomic vapor are

Figure 9 – Saturated absorption spectroscopy of the Rb. The zero of the horizontal axis corresponds to the closed transition $|F = 2\rangle \rightarrow |F' = 3\rangle$ of ^{87}Rb. The inset graph is a zoom of this last transition with the crossover between $|F' = 1\rangle$ and $|F' = 3\rangle$ circled.

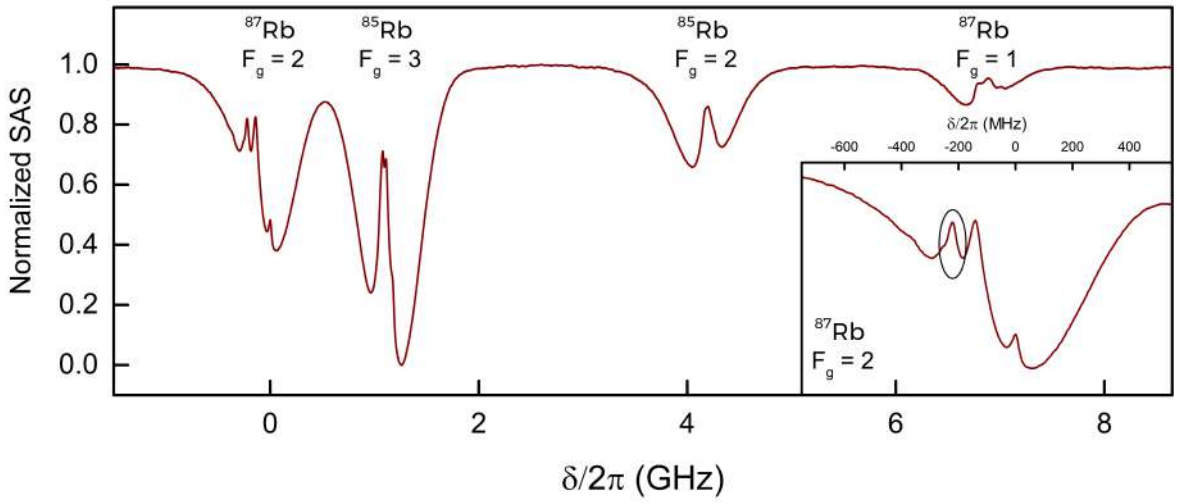

Source: The author (2023).

broadened by the Doppler effect. However, when both lasers have the correct frequency of one of the hyperfine levels and interact with the same velocity group of atoms, the probe beam is less absorbed resulting in a peak in the transmission measurement, as shown in Fig. 9. Notice that there are four absorption dips in this result because each isotope has two hyperfine ground states. Inside each one of these dips, there are six peaks, meaning that on six occasions the pump and probe beams were interacting with the same atoms.

Due to angular momentum selection rules, only three transitions are allowed from the hyperfine ground states. Thus, only in three out of these six peaks, both beams are interacting with the same hyperfine level. The other three peaks are crossover transitions, i.e. the pump beam is resonant with one hyperfine level while the probe interacts with a different one, for the same group of atoms.

3.3 Autler-Townes splitting

In the previous sections, we have presented the basic tools and experimental setup for the generation of the CBL signal. We focus now on the experimental results regarding the dynamic Stark shift observed in this signal, under particular conditions. Furthermore, we aim to understand why this phenomenon does not present itself in the

typical way seen in the literature.

The dynamic Stark shift, also known as the AC Stark effect, is a phenomenon that causes the splitting of energy levels in a transition driven by a strong field that is near resonant. This effect can be observed in fluorescent spectroscopy as the Mollow triplet [71, 72], which is caused by the splitting of the "bare" atom states into two "dressed" states with a separation that is proportional to the Rabi frequency. In three-level systems, this effect is known as Autler-Townes (AT) splitting [28]. In this case, the Stark-shifted levels stimulated by a strong laser field are probed by a weak field in a different transition, resulting in a double peak structure in the weak field transmission curve. In our experiment, the diode laser serves as the strong field in the first transition, while the optical modes of the fs laser act as the weak field (power per mode $\approx 50\mu$W) in the second transition of this three-level ladder system.

The Autler-Townes doublet has been extensively studied in atomic and molecular spectroscopy for various purposes. For example, the AT splitting has been used to measure transition dipole moments and lifetimes of highly excited states [73, 74], to store information in quantum memories [75], and to study microwave propagation in transmission lines [76]. However, in our experiment, we aim to understand why the dynamic Stark shift does not present itself in the usual way seen in the literature.

In a typical three-level cascade system, counterpropagating laser beams are used to explore the almost Doppler-free configuration when the wavelength difference between the two transitions is small. Early studies investigating the AT splitting in a Doppler-broadened medium were conducted in the 1970s [77, 78, 79]. In these cases, it can be challenging to analyze the system analytically, especially in the high-intensity regime. Therefore, numerical methods are often used to study the system, such as the work of Ahmed and Lyyra [80], which investigates the impact of the Doppler width on the observation of the AT splitting for co- and counter-propagating beams. They show that the presence of the AT splitting in the fluorescence depends not only on the Rabi frequency but also on the ratio between the wavenumbers of the coupling and probe laser beams. In particular, the AT doublet is difficult to observe in the copropagating beams configuration, as it does not cancel the Doppler broadening. However, as our results demonstrate, the AT doublet can be distinguished in the CBL signal using a

copropagating setup. In addition, we want to explore how the AT manifests itself in the CBL under two different frequency scanning scenarios: scanning either the repetition rate of the pulsed laser or the cw laser frequency.

Overall, the Autler-Townes effect is an important and widely studied phenomenon that has a wide range of applications in a variety of fields. By understanding the underlying physics of the effect and developing new techniques to control and manipulate the Autler-Townes sublevels, it is possible to harness the full potential of this effect and to advance our understanding of atomic and molecular systems.

3.3.1 Experimental results

Let us begin the discussion of the experimental results with the scenario in which we scan the repetition rate of the fs laser. By proceeding in this manner we change the spacing of the optical modes delivered by the femtosecond laser. We show in Fig. 10 the intensity of the CBL as a function of the Ti:sapphire optical mode detuning (δ_{23}) (bottom axis) or repetition rate (top axis), for different intensities of the diode laser. The diode laser was almost resonant with the closed transition $5S_{1/2}, F = 3 \rightarrow 5P_{3/2}, F = 4$ for the zero velocity group, though its frequency may have varied slightly from curve to curve as we did not use a frequency lock. Instead, we turned off any current modulation in the laser head using the SAS curve as a reference. However, this may have caused the frequency to drift slightly. These measurements were taken with the Rb cell at a temperature of 74 ^{o}C, which corresponds to an atomic density of approximately 10^{12} atoms/cm^3 [81]. Based on measurements of the laser power before and after the Rb cell, we estimate that the intensity of the diode laser at the center of the cell ranged from I_{12} = 1.27 to 14.5 mW/cm^2, while the intensity per optical mode of the Ti:sapphire laser was approximately $I_{23} \approx$0.42 mW/cm^2.

As the power of the strong field increases, we observe a doublet structure in the results shown in Fig. 10. The separation between the peaks depends on the power of the diode laser as well. This structure is typically caused by the energy level splitting resulting from the dynamic Stark shift. However, in this case, the frequency separation is much larger than what would be expected based on the Rabi frequency of the strong field. Normally, the frequency separation scales linearly with the Rabi frequency (or the

Figure 10 – CBL as a function of the optical mode detuning in the $|2\rangle \rightarrow |3\rangle$ transition, for diode laser intensities from 1.27 mW/cm^2 up to 14.5 mW/cm^2 (estimate at the middle of the cell). Bottom axis: detuning of the optical mode nearest to resonance. Top axis: the correspondent repetition rate variation from $f_R = 990.410$ MHz.

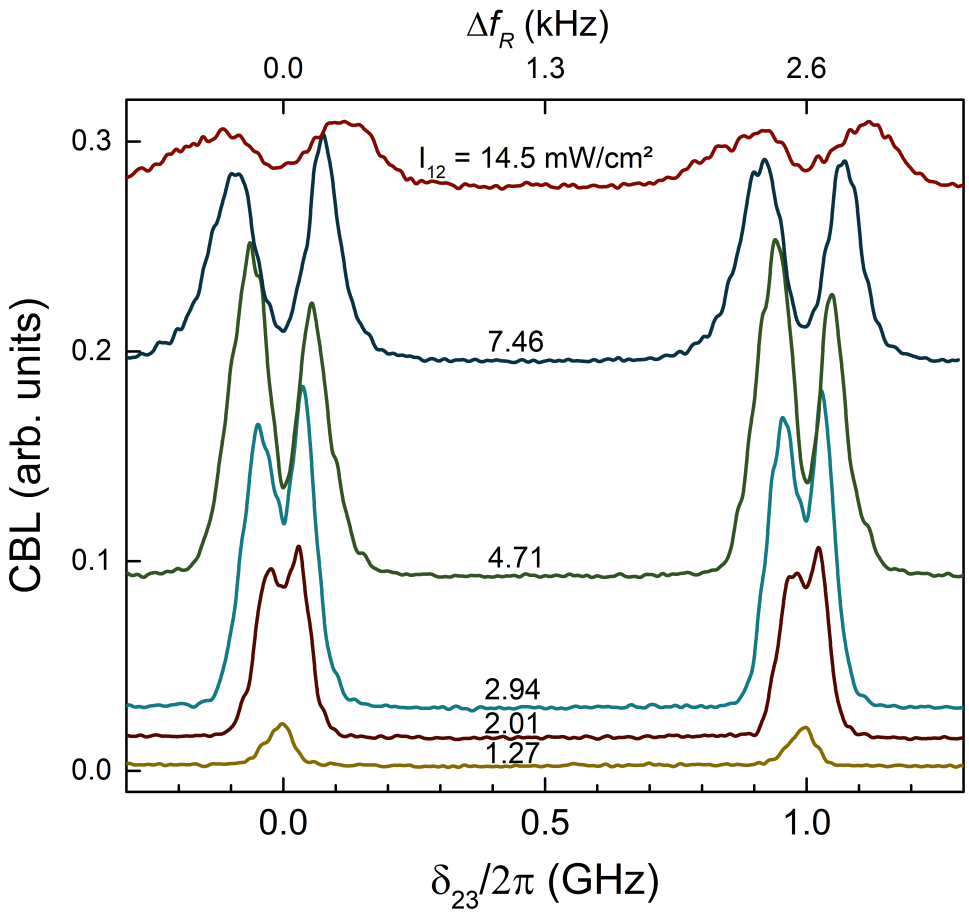

Source: Ref. [59].

square root of the laser power) and is of the order of the Rabi frequency itself. In the results shown in Fig. 10, the frequency separation is hundreds of MHz, while the Rabi frequency of the diode laser (strong field) is only in the tens of MHz. In the following sections, we will use a theoretical model to try to explain these characteristics. It is important to note that, even though this is a more typical setup with the strong laser fixed in frequency and the weak laser scanning, the copropagating configuration of the experiment does not eliminate the effects of Doppler broadening. It is much more common to study the AT splitting using counter-propagating configurations, as these lead to Doppler-free results.

In addition to the doublet structure, our model will also address the asymmetry in the double peak shape and the behavior of the signal amplitude as a function of the strong laser power. The asymmetry may be connected to the fact that the diode laser

was not locked in frequency and may have drifted slightly. The signal amplitude appears to have a saturation behavior, as the curve with the highest laser power is much smaller than the others.

To calibrate the horizontal axis of this graph we remember that, for a resonant mode of the frequency comb ($\delta_{23} = 0$, for the zero velocity atoms), the transition frequency ω_{23} must match an integer multiple of the repetition rate (see Eq. 72). Therefore

$$\frac{\omega_{23}}{2\pi} = m f_R. \tag{73}$$

If we treat m as a continuous variable, then a small change Δm implies in

$$\Delta f_R = -\frac{\omega_{23}}{2\pi m^2}\Delta m, \tag{74}$$

$$= -\frac{2\pi}{\omega_{23}} f_R^2 \Delta m. \tag{75}$$

For neighboring modes ($\Delta m = 1$), the change in the repetition rate is $|\Delta f_R| \approx 2.5$ kHz. With this, we can connect the variations in the repetition rate with the changes in the optical frequency. Note that each curve in Fig. 10 includes a pair of doublets that correspond to the CBL signal generated by two adjacent modes of the frequency comb. We can use the frequency difference between these two doublets to calibrate the bottom axis (optical frequency), with a repetition rate of approximately 990.4 MHz, and consequently, calibrate the top axis (repetition rate variation).

In Fig. 11, we present the results for the second frequency scanning scenario, where the frequency of the diode laser (strong field) is varied while the fs laser (weak field) has a fixed frequency. In this case, the repetition rate is locked, but the offset frequency of the pulse trains is free running. The characteristics of these results are similar to the previous ones. Again, as the power of the strong field increases, a double peak structure appears. Now, we see a contribution from only one mode of the frequency comb. The asymmetry in these results is more pronounced and could be caused by two factors: differences in diode laser absorption across the three hyperfine transitions of the Rb D_2 line, and the mode of the Ti:sapphire laser not being precisely on resonance due to the drifting offset laser frequency. The first factor could be addressed by using large

Figure 11 – Normalized CBL as a function of the diode laser detuning, for a fixed Ti:sapphire laser intensity and diode laser intensities ranging from I_{12} =1.52 up to 10.6 mW/cm^2 (estimate at the middle of the cell). The calibration of the diode laser detuning is obtained with saturated absorption spectroscopy (top curve).

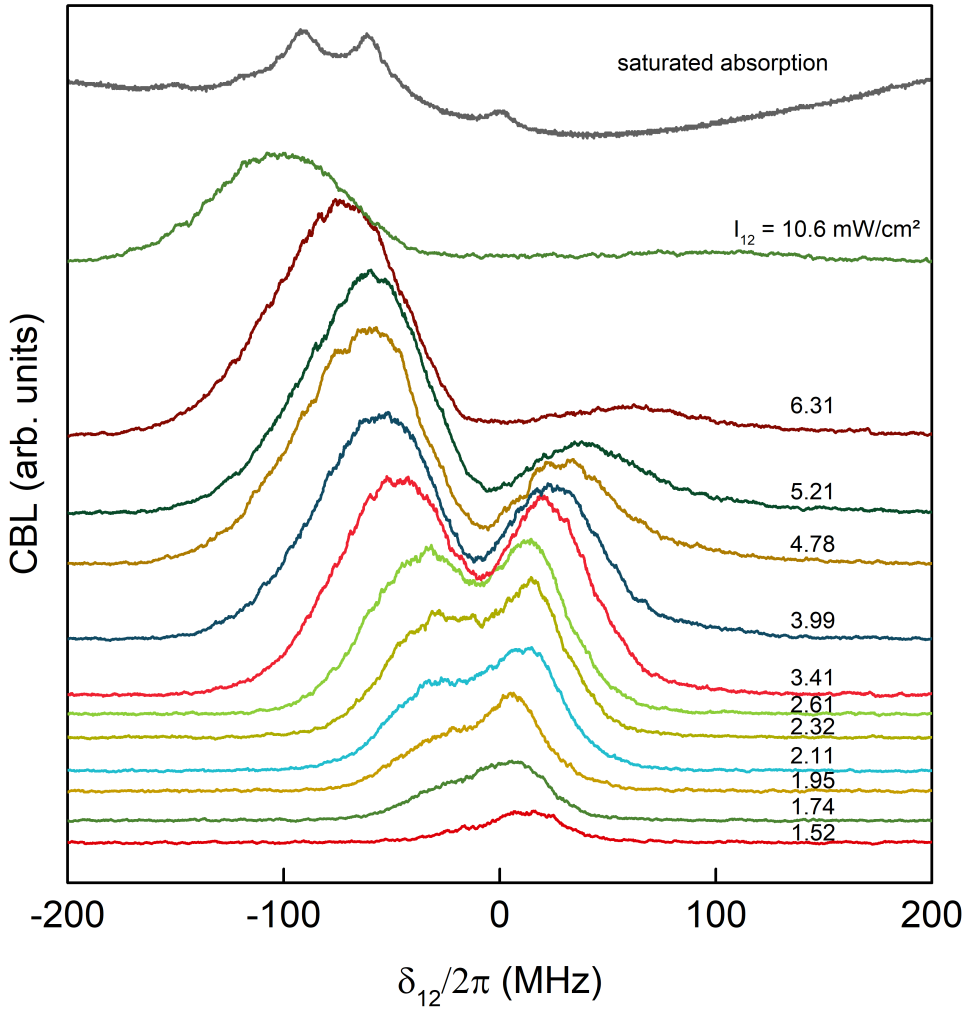

Source: Ref. [59].

magnetic fields as proposed in Refs.[82, 83]. We will show in the theoretical subsection that even a small detuning can change the symmetry of the FWM signal. As for the splitting of the doublet, we again see a linear dependence on the square root of the diode laser power, and a frequency separation that is at least one order of magnitude larger than the Rabi frequency of the strong field (see Fig. 20). This is the main feature we will attempt to explain in the following subsection.

3.3.2 Theoretical model

In this subsection, we aim to model our experimental results and identify the physical mechanisms responsible for the characteristics we observed. To do this, we

consider a four-level system based on the rubidium excitation route $5S_{1/2} \rightarrow 5P_{3/2} \rightarrow 5D_{5/2} \rightarrow 6P_{3/2}$, labeled as $|1\rangle$, $|2\rangle$, $|3\rangle$, and $|4\rangle$, respectively (see Figs. 7 and 12). Our focus is on the CBL generated near the $|4\rangle \rightarrow |1\rangle$ transition (420 nm) when three input fields with Rabi frequencies Ω_{12}, Ω_{23}, and Ω_{34} copropagate through Doppler-broadened rubidium atoms. We assume that the interaction between the atomic system and the fs laser satisfies the conditions for coherent accumulation, as the atomic relaxation time is much longer than the time interval between pulses. Additionally, our frequency comb has a repetition rate such that only one or two modes can interact simultaneously with the velocity groups. Therefore, our theoretical treatment will only consider cw fields.

The electric fields present in the Hamiltonian can be written as

$$\mathbf{E}_l(\mathbf{r},t) = \boldsymbol{\varepsilon}_l \mathscr{E}_l e^{-i(\mathbf{k}_l \cdot \mathbf{r} - \omega_l t)} + c.c, \tag{76}$$

where $\boldsymbol{\varepsilon}_l$ is the polarization vector, $\mathscr{E}_l$ is the field amplitude, $\mathbf{k}_l$ is the wavevector, ω_l is the frequency of each field, and $c.c.$ represents the complex conjugate. The Rabi frequency for the $|j\rangle \rightarrow |k\rangle$ transition is defined as $\Omega_{jk} = \frac{\mu_{jk}\mathscr{E}_l}{\hbar}$, where $\mu_{jk} = \langle j|\left(\hat{\boldsymbol{\mu}} \cdot \boldsymbol{\varepsilon}_l\right)|k\rangle$, with $j \neq k$, is the transition dipole matrix element. For simplicity, we will ignore the spatial part of the fields in our calculations, as we are only interested in the spectral response of the FWM process that leads to CBL generation.

There are a few approaches we can take to understand the energy level splitting observed in our results. One approach is to use the dressed state formalism, which naturally introduces new energy levels. In this case, the field in the $|1\rangle \rightarrow |2\rangle$ transition is intense, causing the Stark effect to split the energy level structure and create new resonances associated with the dressed states $|1;\pm\rangle$ and $|2;\pm\rangle$ (see Fig. 12). These new states have an energy shift given by [49]:

$$\omega_{1\pm} = -\frac{\delta_{12}}{2} \pm \frac{1}{2}\sqrt{4\Omega_{12}^2 + \delta_{12}^2}, \tag{77a}$$

$$\omega_{2\pm} = +\frac{\delta_{12}}{2} \pm \frac{1}{2}\sqrt{4\Omega_{12}^2 + \delta_{12}^2}, \tag{77b}$$

where δ_{ij} is the detuning of the field regarding the $|i\rangle \rightarrow |j\rangle$ transition.

This formalism might ease some of our analysis and notation. However, we choose a different path. We will solve numerically the Bloch equations using the atom

Figure 12 – Stark-shifted rubidium level diagram considering a strong field in the $|1\rangle \rightarrow |2\rangle$ transition. Ω_{ij} and δ_{ij} are the Rabi frequency and the detuning of the field regarding the $|i\rangle \rightarrow |j\rangle$ transition, respectively.

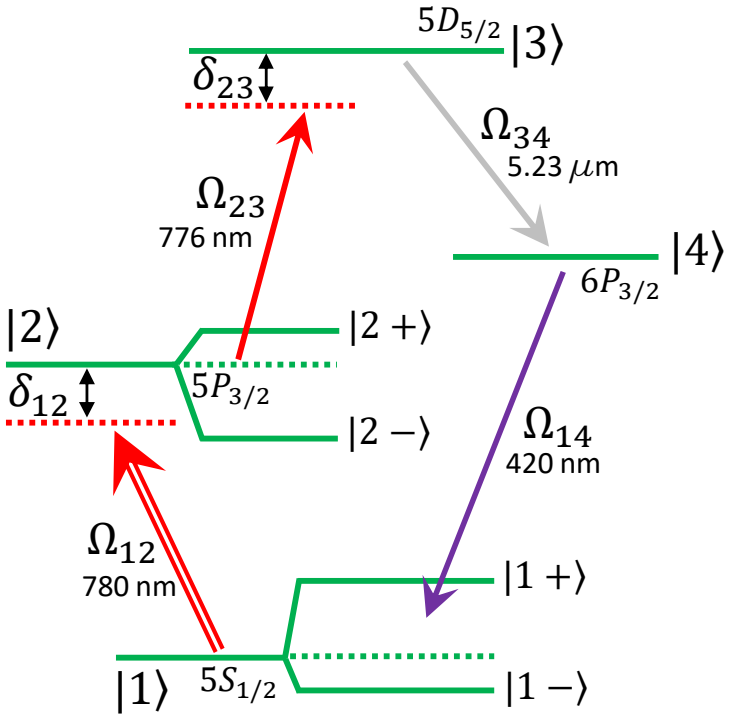

Source: Ref. [59].

states basis, in a similar procedure of the previous section. We begin the analysis employing the density-matrix formalism with Liouville's equation (see Eq. 27). In this four-level case, the matrix representation of the hamiltonian $\hat{H}$, in the rotating frame, is

$$\hat{H} = \hbar \begin{pmatrix} 0 & -\Omega'_{12} & 0 & -\Omega'_{14} \\ -\Omega'^{*}_{12} & \omega_{21} & -\Omega'_{23} & 0 \\ 0 & -\Omega'^{*}_{23} & \omega_{31} & -\Omega'_{34} \\ -\Omega'^{*}_{14} & 0 & -\Omega'^{*}_{34} & \omega_{41} \end{pmatrix}. \tag{78}$$

In this notation, $\Omega'_{jk} \equiv \Omega_{jk} e^{i\omega_\eta t}$, in which ω_η is the frequency of the laser in a particular transition. The density-matrix elements should be similar to the example in section 2. However, we add the velocity component v, in the direction of the propagation of the lasers, to the detuning terms. Hence, we write the Bloch equations as

$$\dot{\rho}_{11} = -i\Omega_{12}\sigma_{12} + c.c. - i\Omega_{14}\sigma_{14} + c.c + \Gamma_{22}\rho_{22} + \Gamma_{41}\rho_{44}, \tag{79a}$$

$$\dot{\rho}_{22} = i\Omega_{12}\sigma_{12} + c.c. - i\Omega_{23}\sigma_{23} + c.c. - \Gamma_{22}\rho_{22} + \Gamma_{32}\rho_{33}, \tag{79b}$$

$$\dot{\rho}_{33} = i\Omega_{23}\sigma_{23} + c.c. - i\Omega_{34}\sigma_{34} + c.c. - (\Gamma_{32} + \Gamma_{34})\rho_{33}, \tag{79c}$$

$$\dot{\rho}_{44} = -i\Omega_{34}\sigma_{23} + c.c. + i\Omega_{14}\sigma_{14} + c.c. + \Gamma_{34}\rho_{33} - \Gamma_{41}\rho_{44}, \tag{79d}$$

$$\dot{\sigma}_{12} = [i(\delta_{12} - k_{12}v) - \gamma_{12}]\,\sigma_{12} + i\Omega_{14}\sigma_{42} - i\Omega_{23}\sigma_{13} + i\Omega_{12}(\rho_{22} - \rho_{11}), \tag{79e}$$

$$\dot{\sigma}_{23} = [i(\delta_{23} - k_{23}v) - \gamma_{23}]\,\sigma_{23} + i\Omega_{12}\sigma_{13} - i\Omega_{43}\sigma_{24} + i\Omega_{23}(\rho_{33} - \rho_{22}), \tag{79f}$$

$$\dot{\sigma}_{14} = [i(\delta_{14} - k_{14}v) - \gamma_{14}]\,\sigma_{14} + i\Omega_{12}\sigma_{24} - i\Omega_{43}\sigma_{13} + i\Omega_{14}(\rho_{44} - \rho_{11}), \tag{79g}$$

$$\dot{\sigma}_{43} = [i(\delta_{43} - k_{43}v) - \gamma_{43}]\,\sigma_{43} + i\Omega_{14}\sigma_{13} - i\Omega_{23}\sigma_{42} + i\Omega_{43}(\rho_{33} - \rho_{44}), \tag{79h}$$

$$\begin{aligned}\dot{\sigma}_{13} &= [i(\delta_{12} + \delta_{23} - (k_{12} + k_{23})v) - \gamma_{13}]\,\sigma_{13} + \\ &+ i\Omega_{12}\sigma_{23} + i\Omega_{14}\sigma_{43} - i\Omega_{23}\sigma_{12} - i\Omega_{43}\sigma_{14},\end{aligned} \tag{79i}$$

$$\begin{aligned}\dot{\sigma}_{24} &= [i(\delta_{14} - \delta_{12} - (k_{14} - k_{12})v) - \gamma_{24}]\,\sigma_{24} + \\ &+ i\Omega_{12}\sigma_{14} + i\Omega_{23}\sigma_{34} - i\Omega_{14}\sigma_{21} - i\Omega_{43}\sigma_{23}.\end{aligned} \tag{79j}$$

where γ_{jk} represent the relaxation rates of the coherences, Γ_{jk} is the population spontaneous relaxation rate from a $|k\rangle$ state to a $|j\rangle$ state, δ_{jk} and k_{jk} are the detuning and wavenumber of the field associated to the Rabi frequency Ω_{jk}, and $\sigma_{jk} \equiv \rho_{jk}e^{-i\omega_\eta t}$ is the slow envelope of the coherence ρ_{jk}.

Out of all elements of the density matrix, we are interested in the coherence σ_{14} and the population of the state $|3\rangle$, ρ_{33}. The square modulus of σ_{14} connects with the FWM signal while the upper state population represents the fluorescence emitted by the atoms. To compare the results with the experimental data, one must take into account the contribution of all velocity groups of the hot vapor:

$$\bar{\rho}_{33} = \int_{-\infty}^{\infty} \rho_{33}(v) f(v) dv, \tag{80a}$$

$$\bar{\sigma}_{14}, = \int_{-\infty}^{\infty} \sigma_{14}(v) f(v) dv. \tag{80b}$$

where $f(v)$ is the Maxwell-Boltzmann velocity distribution.

In order to obtain the results presented in the following sections, we solved the Bloch equations (Eqs. 79) numerically using the fourth-order Runge-Kutta method

Table 1 – Numerical parameters for the theoretical model.

Decay rates (MHz)	
Γ_{22}	$2\pi \times 6.06$
Γ_{33}	$2\pi \times 0.66$
Γ_{44}	$2\pi \times 1.3$
Γ_{32}	$0.65\Gamma_{33}$
Γ_{34}	$0.35\Gamma_{33}$
γ_{12}	$\Gamma_{22}/2$
γ_{23}	$(\Gamma_{33}+\Gamma_{22})/2$
γ_{34}	$(\Gamma_{33}+\Gamma_{44})/2$
γ_{14}	$\Gamma_{44}/2$
γ_{13}	$\Gamma_{33}/2$
γ_{24}	$(\Gamma_{44}+\Gamma_{22})/2$
Wavelengths (nm)	
λ_{12}	780
λ_{23}	776
λ_{34}	5300
λ_{14}	420

Source: Ref. [46, 45].

over a time period of $t = 0$ to $t = 2\ \mu s$ (code available in Ref. [84]). This integration time is approximately the average transit time of the atoms through laser beams with a diameter of 0.2 mm. The initial conditions we used were $\rho_{11}(0) = 1$ and $\rho_{22}(0) = \rho_{33}(0) = \rho_{44}(0) = \sigma_{ij}(0) = 0$. This calculation is computationally intensive, so we used three graphics processing units (*Nvidia RTX 2070 Super*) to solve the differential equations simultaneously for all velocity groups. The numerical parameters we used in all our computations are listed in Table 1. The decay rates and wavelengths come from Ref. [46, 45]. To simulate the amplified spontaneous emission that occurs in the $5D \rightarrow 6P$ transition [69], we set a small Rabi frequency value for the 5.23 μm field (Ω_{34} = 1 rad/s) to act as a seed in the FWM process. Additionally, we fixed the frequency of this field on resonance ($\delta_{34} = 0$) and, as a result, $\delta_{14} = \delta_{12} + \delta_{23} - \delta_{34}$ due to energy conservation.

3.3.2.1 Velocity dependence of the fluorescence and CBL

Before including the contribution of all atoms and therefore introducing Doppler broadening, it may be helpful to examine the dependence of the fluorescence and CBL signal on each atomic velocity group. As in the experiment, we consider two frequency scanning scenarios, where either the frequency of the weak beam (Ω_{23}) or the frequency

Figure 13 – (a) ρ_{33} as a function of δ_{23} and v, considering $\Omega_{12}/(2\pi) = 12$ MHz, $\Omega_{23}/(2\pi) = 0.6$ MHz and $\delta_{12} = 0$. (b) ρ_{33} for three velocity groups. (c) ρ_{33} integrated over the Maxwell-Boltzmann distribution.

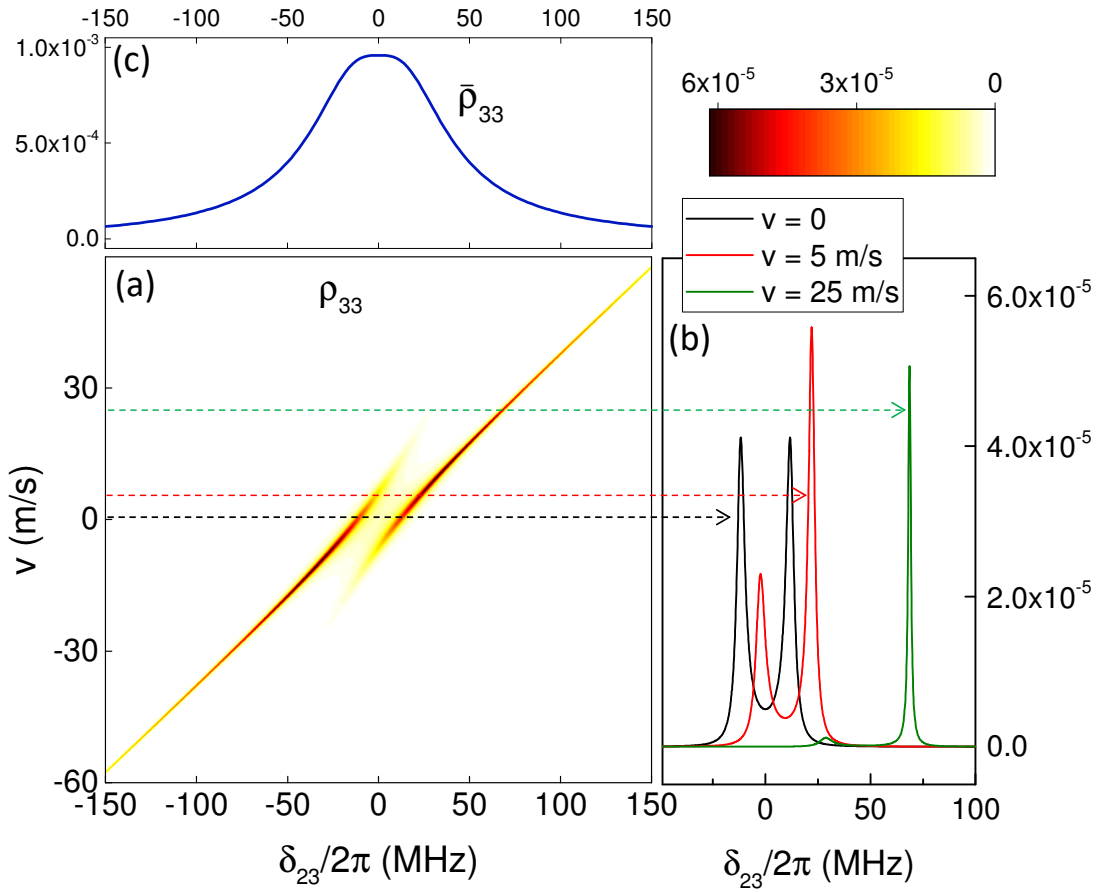

Source: Ref. [59].

of the strong beam (Ω_{12}) is varied.

First, let us consider the case where we scan the frequency of the weak beam Ω_{23} while the strong beam is in resonance with the $|1\rangle \rightarrow |2\rangle$ transition ($\delta_{12} = 0$) for the zero velocity group. In Fig. 13(a), we present the population of the upper state ρ_{33} as a function of δ_{23} for various velocity groups. The fluorescence signal is proportional to this term in the density matrix, so all the analysis regarding this signal will be based on ρ_{33}.

We highlight the behavior of the population ρ_{33} for three specific velocity groups in Fig. 13(b), where it is possible to see the doublet structure due to the dynamic Stark shift. If we consider $k_{12} \approx k_{23} \equiv k$, then the peaks of the doublets shown in Fig. 13(b) arise when the two-photon condition is satisfied. Therefore, we solve the equation

$\delta_{23} - kv + \omega_{2\pm} = 0$ and find that ([77])

$$\delta_{23} = \frac{3kv}{2} \pm \frac{1}{2}\sqrt{4\Omega_{12}^2 + k^2v^2}. \tag{81}$$

Whenever $v \neq 0$, the doublet is asymmetric as the red curve in Fig. 13(b) indicates. Moreover, the nearest side-band from the resonance is always smaller [85]. Even though specific velocity groups might have a level splitting, the Doppler-broadening hides the AT effect, as it is possible to observe in Fig. 13(c). This result is also in agreement with the discussion in Ref. [77]: one should observe a larger power broadening without any splitting in the fluorescence signal. Consequently, it is unlikely to observe the splitting in experiments that detect only fluorescence. However, as we will show, the FWM can reveal this effect in the CBL signal, even after the Doppler integration.

In Fig. 14, we present a similar analysis for the coherence σ_{14}, where we first examine the response of each velocity group and then obtain the total response of the Doppler-broadened medium. We are interested in the FWM signal, so we look at the squared modulus of σ_{14} rather than the coherence itself. The color map in Fig. 14(a) shows a doublet structure, similar to Fig. 13(a), but the overall curve shape is different. To understand this curve in more detail, we can look at specific velocity groups in Fig. 14(b). The peak positions of each of these curves are dictated by Eq. (81), linking their origin to the FWM process.

It is important to note that we present the squared modulus of σ_{14} for each velocity group in Fig. 14(a) and (b). However, if the phases between each velocity group are relevant, we must first integrate the coherence σ_{14} with the Maxwell-Boltzmann distribution, and only then take its squared modulus, as shown in the blue curve of Fig. 14(c). There are situations, which we explore in the following subsection, where we can neglect these phases and integrate the squared modulus of the coherence directly, but for modeling the AT splitting, it is crucial to perform these calculations in the correct order. As discussed in Ref. [86], the macroscopic field polarization from different ensembles of atoms within the atomic velocity groups can interfere, leading to a modification of the FWM spectra. To illustrate the difference between the two ways of calculating the signal, we present the dashed curve in Fig. 14(c), where we first take the

Figure 14 – (a) $|\sigma_{14}(v)|^2$ as a function of δ_{23}, for many velocity groups, considering $\Omega_{12}/2\pi = 12$ MHz, $\Omega_{23}/2\pi = 0.6$ MHz and $\delta_{12} = 0$. (b) $|\sigma_{14}(v)|^2$ for three velocity groups. (c) Blue: σ_{14} integrated over the Maxwell-Boltzmann distribution and then squared; Dashed line: $|\sigma_{14}|^2$ integrated over the Maxwell-Boltzmann distribution.

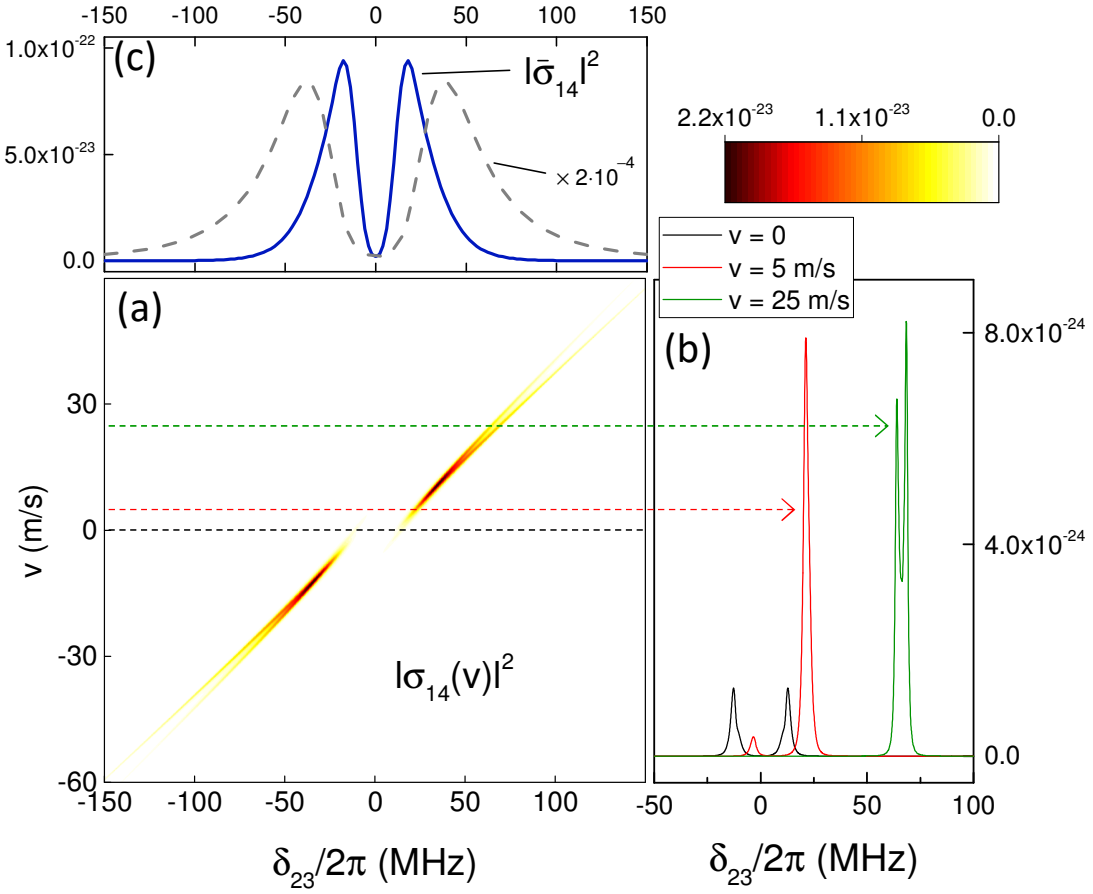

Source: Ref. [59].

squared modulus of the coherence and then integrate it. It is clear that, although the splitting is present, the frequency distance between the peaks is larger than in the blue curve

The comparison between Figs. 13(b) and 14(b) renders interesting results. One can see that the behavior of the coherence σ_{14} is significantly different from the population ρ_{33} when it comes to the nonzero velocity groups (see the green and red curves). Once the velocity increases, there is a dramatic difference in the coherence response near resonance. The AC Stark effect takes place and splits the level structure for each velocity group, as in the red curve of Fig. 14(b). However, the peak near resonance is very small. Once all the groups add up in the Doppler integration, they contribute to the FWM signal in the blue curve of Fig. 14(c) with a doublet-like structure. The same argument applies to the population ρ_{33}. However, in this case, the difference between

the peak's amplitude is not as dramatic as with the coherence, so once the groups add up, the splitting is gone.

Let us analyze the second frequency sweeping scheme. This is an unusual case, in which we investigate the presence of Stark shift as a function of the strong field detuning, δ_{12}. That is, the same field that splits the energy level is the one we scan. Using again Eq. (77b) and the resonance of two photons with the frequency of the weak field fixed at the resonance ($\delta_{23} = 0$), we obtain the following equation for the peak position, considering $v \neq 0$:

$$\delta_{12} = \frac{2k^2v^2 - \Omega_{12}^2}{kv}. \tag{82}$$

The analysis is very similar for this case. We examine the behavior of the upper population ρ_{33} as a function of the detuning δ_{12}, while keeping the Rabi frequencies Ω_{12} and Ω_{23} constant at $2\pi \times 12$ MHz and $2\pi \times 0.6$ MHz, respectively, and setting the detuning δ_{23} to zero. The results are shown in Figs. 15(a) and (b). It is interesting to note that the two-photon resonance condition is never satisfied for a velocity of $v = 0$. However, for very small velocities ($v < 3$ m/s), a far detuned Ω_{12} field is necessary to achieve two-photon resonance. The black and red curves in Fig. 15(b) correspond to a non-resonant situation, where the Ω_{23} field does not resonate with the Stark-shifted sidebands $\omega_{2\pm}$. In contrast, the green curve in Fig. 15(b) corresponds to an exact two-photon resonance, which results in a higher, narrow peak. Since Equation (82) has a single solution, there is not a doublet-like structure. When the Doppler integration is performed, the contribution of the non-resonant two-photon transition near $\delta_{12} = 0$ for many velocity groups is sufficient to produce a large value of $\bar{\rho}_{33}$ near resonance, which hides the Autler-Townes (AT) splitting, as can be seen in Fig. 15(c).

The copropagating setup is a key factor in explaining the absence of the Autler-Townes (AT) splitting in the upper population of a Doppler medium. In this geometric arrangement, an experimental fluorescence measurement would not show the characteristic two peaks of the AT doublet. This is because the observation of the AT splitting depends on the relationship between the wavevectors and intensities of the incident beams, as noted by Feneuille and Schweighofer [77]. In contrast, in the typical

Figure 15 – (a) ρ_{33} as a function of δ_{12} and v, considering $\Omega_{12}/(2\pi) = 12$ MHz, $\Omega_{23}/(2\pi) = 0.6$ MHz and $\delta_{23} = 0$. (b) ρ_{33} for three velocity groups. (c) ρ_{33} integrated over the Maxwell-Boltzmann distribution.

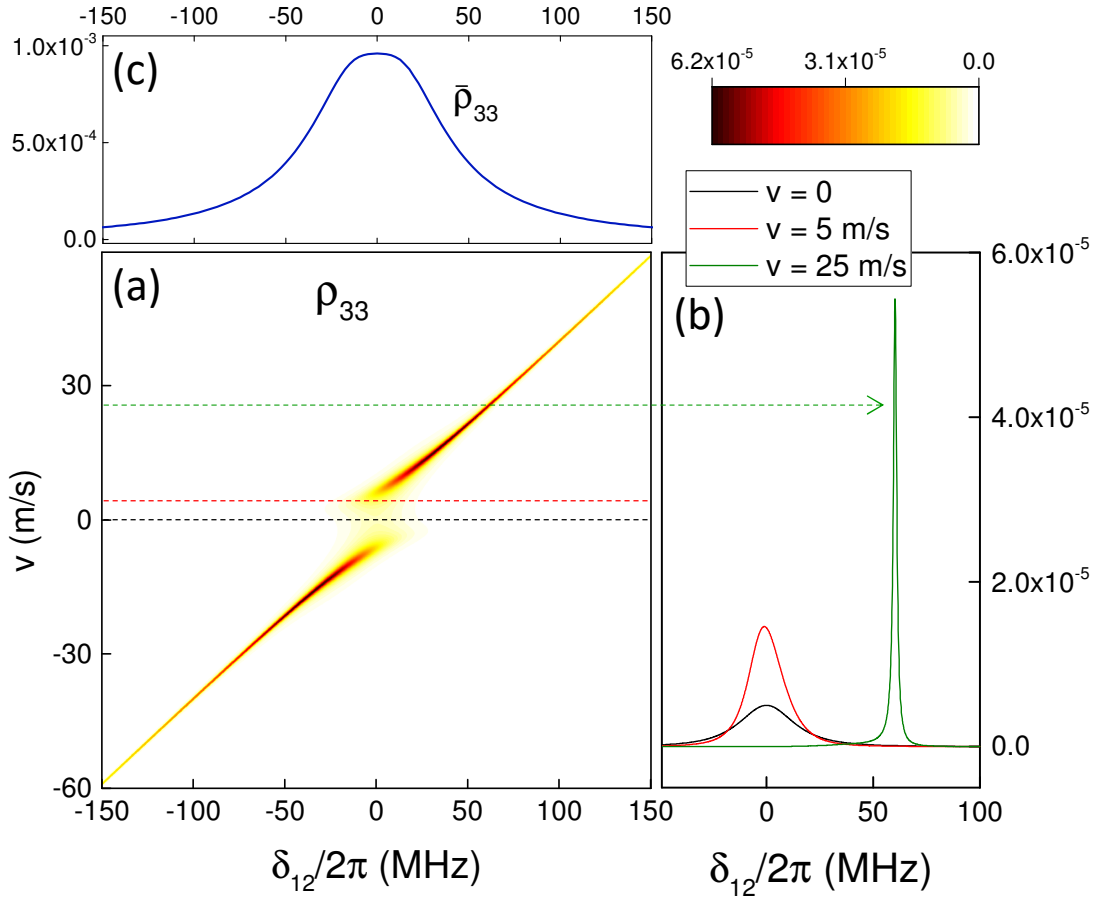

Source: Ref. [59].

counterpropagating setup, the AT splitting can be observed regardless of which beam is sweeping, the strong or the weak [87]. However, if the atoms are at rest, the behavior is the same for copropagating and counterpropagating beams.

We present the results for the coherence σ_{14} in Fig. 16, using the same parameters as in Fig. 15. As with ρ_{33}, we examine the squared modulus of σ_{14}. In comparison to ρ_{33}, σ_{14} is even more sensitive to the velocities of the atoms, leading to a small value near $v = 0$, as shown in Figs. 16(a) and (b). When the Doppler integration is performed, the doublet structure becomes dominant, resulting in a dip in the squared modulus of the integrated coherence, $|\bar{\sigma}_{14}|^2$, as shown by the blue curve in Fig. 16(c). This dip is a consequence of the Stark shift combined with a non-satisfied two-photon transition for low velocities.

It is important to notice that in this frequency-sweeping regime, the phase between velocity groups is not as relevant to the frequency distance between the

two peaks as it was for the weak field frequency-sweeping results. The dashed line of Fig. 16(c), obtained first by taking the squared modulus of the coherence and then integrating it, is slightly wider than the blue curve. Nevertheless, the following results have the same calculation procedure as the blue curves of Figs. 14(c) and 16(c).

We must emphasize that, while for copropagating beams, the results for fluorescence and FWM are different whether it is the strong or the weak beam that is scanning, for a configuration of counterpropagating beams, the AT splitting can be observed both in fluorescence and in FWM, no matter which laser beam is being swept [88].

It appears that different physical mechanisms contribute to the presence of the doublet structure in the FWM signal and the lack of it in the fluorescence when the Doppler integration is performed for the two frequency sweeping mechanisms. We will delve deeper into these mechanisms and highlight their differences in the following subsection.

3.3.2.2 Doppler integration

For a group of atoms with a velocity of $v = 0$, there are an infinite number of combinations of laser frequencies that satisfy the two-photon resonance condition for the transition $|1\rangle \rightarrow |3\rangle$. These combinations are given by the equation $\delta_{12} + \delta_{23} = 0$. However, as shown in Fig 17, where $|\sigma_{14}|^2$ is plotted as a function of the laser detunings δ_{12} and δ_{23}, this coherence is dominated by the two-photon transition when one-photon resonances are also present ($\delta_{12} = \delta_{23} = 0$). The color map in Fig. 17 is plotted on a logarithmic scale.

The integration of the Maxwell-Boltzmann distribution of velocities introduces additional possibilities, as shown in Fig. 18(a). This figure displays the square modulus of $|\bar{\sigma}_{14}|^2$ for the same intensities as in Fig. 17, but with the integration of the coherence with the Maxwell-Boltzmann distribution as previously discussed. The configuration where $\delta_{12} = \delta_{23} = 0$ still dominates, but for copropagating beams, $|\bar{\sigma}14|^2$ is much higher when $\delta_{12} = \delta_{23}$ compared to $\delta_{12} = -\delta_{23}$. This is because there is always a group of atoms with velocities around δ_{23}/k_{23} that are simultaneously in one- and two-photon resonance when $\delta_{12} = \delta_{23}$ is selected since $k_{23} \approx k_{12}$ for the rubidium energy levels.

Figure 16 – (a) $|\sigma_{14}(v)|^2$ as a function of δ_{12}, for many velocity groups, considering $\Omega_{12}/2\pi = 12$ MHz, $\Omega_{23}/2\pi = 0.6$ MHz and $\delta_{23} = 0$. (b) $|\sigma_{14}(v)|^2$ for three velocity groups. (c) Blue: σ_{14} integrated over the Maxwell-Boltzmann distribution and then squared; Dashed line: $|\sigma_{14}|^2$ integrated over the Maxwell-Boltzmann distribution.

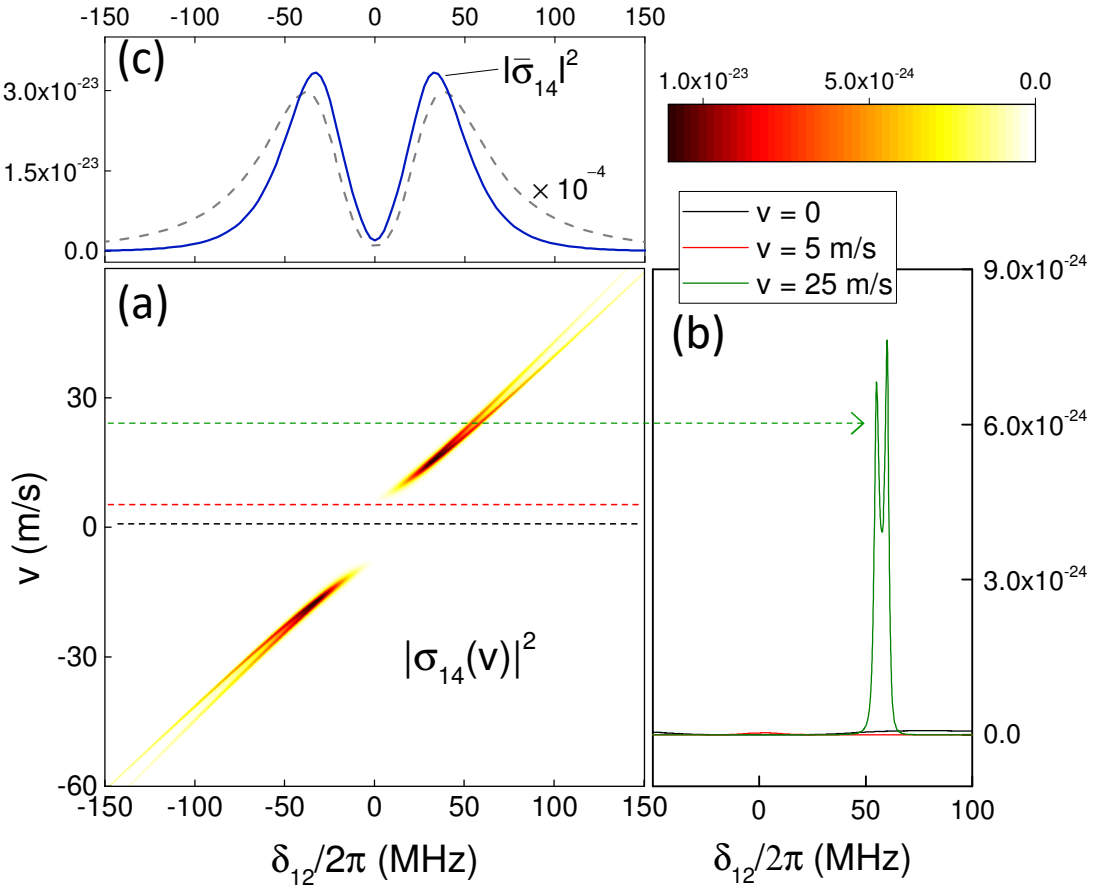

Source: Ref. [59].

Now, consider an increase in the Rabi frequency of the field in the lower transition ($|1\rangle \rightarrow |2\rangle$). There is a significant impact in the FWM due to the Stark shift, as Fig. 18(b) shows. In this figure, we plot $|\bar{\sigma}14|^2$ as a function of δ_{12} and δ_{23} when the lower transition is driven by a strong field ($\Omega_{12}/2\pi = 12$ MHz) and the weaker field ($\Omega_{23}/2\pi = 0.6$ MHz) stimulates the upper transition $|2\rangle \rightarrow |3\rangle$. It can be seen that the single peak in Fig. 18(a) splits into two peaks located above the line $\delta_{12} = -\delta_{23}$. As a result, there is a doublet structure in the typical configuration (weak beam varying its frequency with the strong beam on resonance) and in the opposite situation (strong beam scanning with the weak beam fixed on resonance), as shown in Figs. 18(c) and (d).

Additionally, the asymmetry observed in the experimental data can be explained by considering the velocity group of atoms that the fixed frequency laser is resonant with. If the fixed frequency laser is resonant with a different velocity group that is, δ_{23} or

Figure 17 – Coherence $|\sigma_{14}|^2$ as a function of δ_{12} and δ_{23}, for a group of atoms with $v = 0$ in a weak field regime: $\Omega_{12} = \Omega_{23} = 2\pi \times 0.6$ MHz. Logarithmic scale.

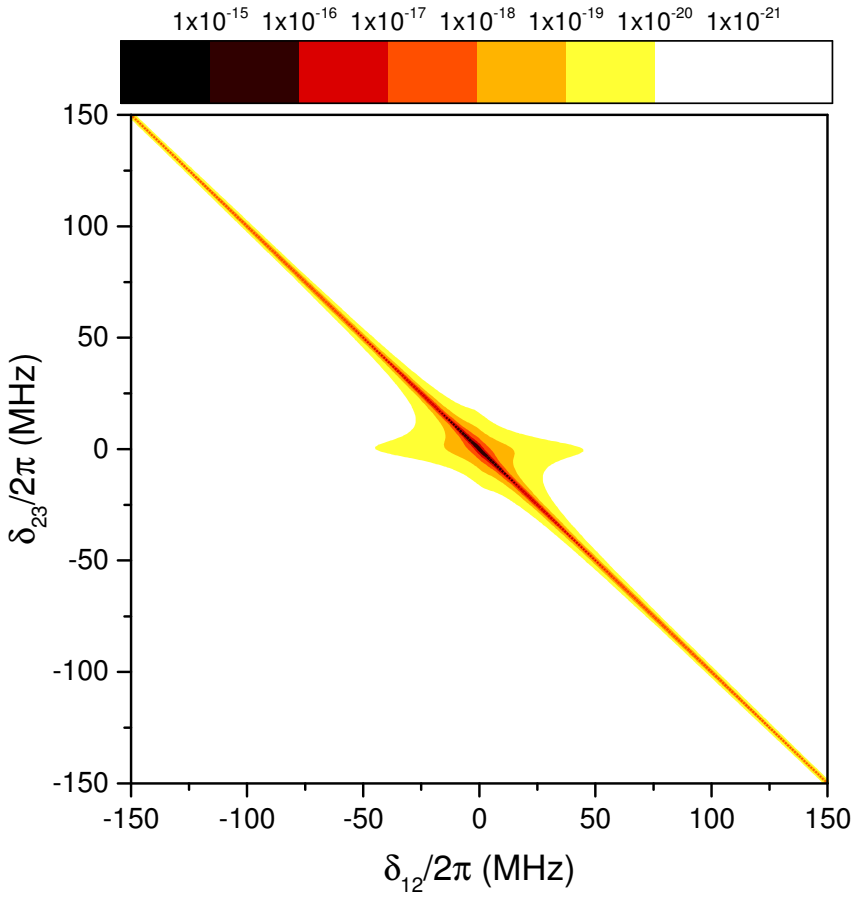

Source: Ref. [59].

$\delta_{12} \neq 0$, the signal becomes asymmetric, regardless of the frequency scanning scheme.

It is important to remember the results from the previous subsection. The Autler-Townes splitting appears for each velocity group in both scanning configurations in the coherence $|\sigma_{14}(v)|^2$, but the final FWM spectra can only be obtained after proper Doppler integration. Therefore, the splitting observed in the FWM is not solely due to the Stark effect but is also connected to the Doppler integration as the velocity groups contribute differently to the final FWM output (see Figs. 14(c) and 16(c)).

It is interesting that this particular combination of effects only manifests itself as a double peak structure in the FWM. We hypothesize that it is connected to the scaling of the FWM with the one- and two-photon coherences. In a perturbative analysis, a more intuitive way to view the system, is that fluorescence (or absorption) scales linearly with the one- and two-photon coherences (σ_{12}, σ_{23}, and σ_{13}), while the FWM signal scales with the square of these same coherences. This behavior should hold in our numerical

solution with all orders of interaction.

However, it is important to note that this manifestation of the AT effect is unusual. The typical interpretation of the separation between peaks in the FWM signal as the actual energy difference between split levels does not apply here. Our results from the previous subsection show that each velocity group has its energy split, even if this split behaves differently depending on which field is scanning. We argue that, when added together, the contributions of all atoms near resonance are very small compared to the contribution far from resonance, forming the doublet-like structure of Fig. 18(b). The frequency separation between the peaks is about one order of magnitude greater than the Rabi frequency, while the actual energy split for each group must be of the order of the Rabi frequency.

In Figs. 19(a) and (b), we further investigate the relationship between the FWM signal ($|\bar{\sigma}_{14}|^2$) and the intensity of the lower transition beam, Ω_{12}, for the two frequency scanning setups. In both cases, the splitting increases linearly, but with different slope coefficients. For the scenario where the weak beam is sweeping, the splitting is approximately $1.9\Omega_{12}$, which is very close to the Autler-Townes splitting for a single group of atoms with $v = 0$ ($2\Omega_{12}$). On the other hand, if the strong beam frequency varies, the splitting is much higher, at approximately $4.2\Omega_{12}$. We can interpret this greater separation by looking at the results in Fig. 16(b) for this scanning configuration. It is clear that the contribution to $|\bar{\sigma}_{14}|^2$ from one of the AT doublet peaks, which is closer to resonance, is negligible. Therefore, this greater separation corresponds to the distance between the most distant peaks of the resonance due to two AT doublets of different velocity groups. The experimental results do not show a significant difference between the two frequency scanning configurations. However, small changes in the model parameters may improve the agreement.

The peak amplitude of the doublet also behaves differently in the two frequency scanning configurations: it saturates when the weak beam is sweeping its frequency, while it reaches a maximum and then decreases when the strong beam is sweeping. These different behaviors are due to distinct physical mechanisms at play in the two configurations. In the typical experiment, with the weak beam sweeping, the strong field in the lower transition splits the intermediate level into two due to the Stark effect.

Figure 18 – $|\bar{\sigma}_{14}|^2$ as a function of δ_{12} and δ_{23}, for (a) $\Omega_{12}/2\pi = 0.6$ MHz and (b) $\Omega_{12}/2\pi = 12$ MHz. (c) and (d): $|\bar{\sigma}_{14}|^2$ for δ_{12} or δ_{23} constant, as indicated by the dashed curves in (b). The green curve in (c) and the black curve in (d) are the same as presented in figures 14(c) and 16(c), respectively.

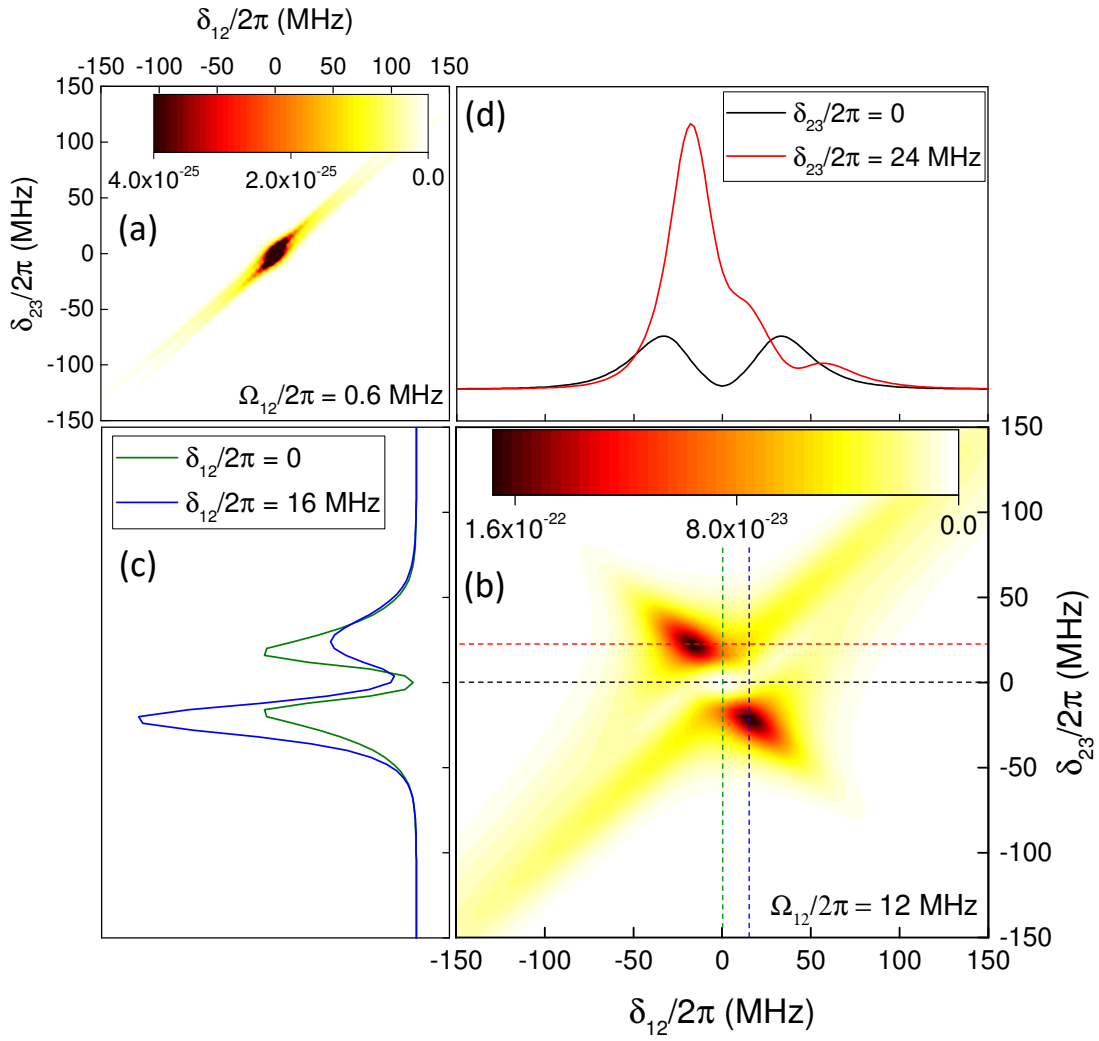

Source: Ref. [59].

The weak beam in the upper transition then probes these split levels. Since we are considering a closed system, there will always be atoms that can satisfy the two-photon resonance and induce the FWM process. In the other frequency scanning setup, the weak beam has a fixed frequency, so eventually, the strong beam will lead to splitting so large that a two-photon resonance can no longer occur, resulting in a decrease in the signal.

3.3.3 CBL amplitude and frequency separation in the AT splitting

We have discussed the experimental results and developed a model to understand the mechanisms behind this unusual manifestation of the dynamic Stark shift. The

Figure 19 – $|\bar{\sigma}_{14}|^2$ as a function of Ω_{12} and (a) δ_{23} or (b) δ_{12}.

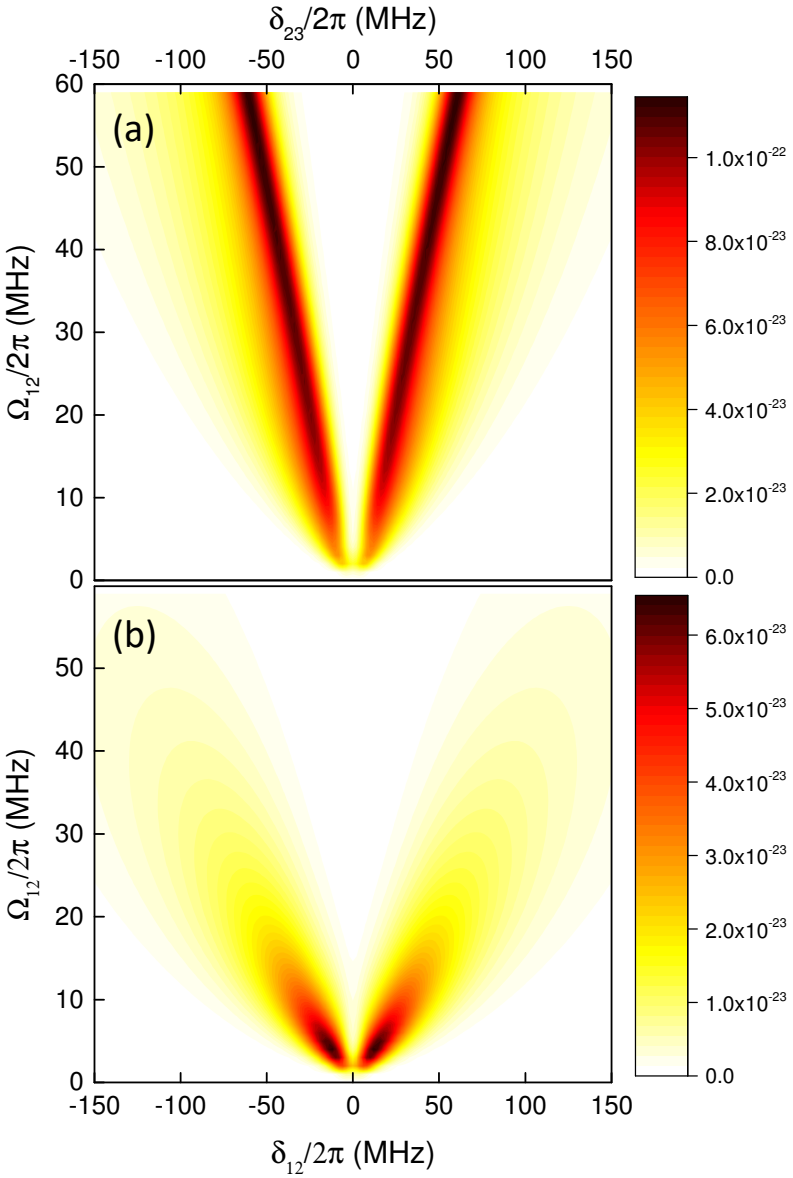

Source: Ref. [59].

final point to consider is whether the theory can produce spectra with similar amplitude and frequency separation between the peaks as in the experiment. Let us start by analyzing the signal amplitude. In Fig. 20(a), we present the experimental results for this parameter as a function of the square root of the diode laser intensity. It is clear that there is an amplitude decay for high-intensity beams in both frequency scanning regimes. However, our theoretical model (Fig. 20(b)) cannot predict the experimental behavior when the weak beam is scanning. As we discussed previously, if we consider a closed system, there will always be atoms with the proper velocity to satisfy the two-photon condition. This type of intensity saturation behavior of the FWM signal was

observed in a pure four-level system [89]. However, in the experiment we describe here, three possible hyperfine transitions can be induced by the diode laser. In the weak beam frequency scanning regime, the diode laser is fixed on a cyclic transition, and therefore, the system is closed. But if the diode laser is strong enough, it will pump atoms to the open transitions, meaning that the system will no longer be closed as the atoms fall into a different fundamental hyperfine level of rubidium [90]. To include this possibility in the model in a simple way, we introduce a 1 MHz decay rate in the population ρ_{22}, allowing for the loss of about 1/6 of the atoms when solving the Bloch equations. This results in the peak amplitude as a function of the strong beam Rabi frequency shown in Fig. 20(c). This way, the model achieves a behavior compatible with the experiment and reveals that the observed decay of the signal in the two frequency scanning configurations has different mechanisms behind it for each situation: optical pumping for other hyperfine levels and far detuning from resonance.

Another feature we highlighted in the experimental results was the frequency separation between the peaks of the signal or the “splitting” of the doublet. The experimental splitting appears to be the same for both frequency scanning setups, as shown in Fig. 20(d). However, our theoretical model not only predicts a difference in the splitting between the two scanning regimes but also gives lower values, as shown in Fig. 20(e). Once again, if we consider that the system is open due to the high intensity of the strong field, these results do improve, as shown in Fig. 20(f). A final consideration is the error bar of the experimental frequency measurement. Each scanning regime uses a different, and therefore, more or less precise, calibration parameter. If the diode laser is scanning, we use the saturation absorption curve, while for the Ti:sapphire scanning, the repetition of the signal, due to two consecutive frequency modes, gives the time-frequency conversion factor. Therefore, there could be a difference between the experimental splittings, but it could be masked by a systematic error in the time-frequency conversion.

3.4 Interference between excitation pathways

Until this point, we have described an experimental setup in which two copropagating beams, a continuous field at 780 nm, and an optical mode of a frequency comb at 776 nm, drive the steps of a two-photon transition from $5S_{1/2}$ to $5P_{3/2}$ to $5D_{5/2}$ in ^{85}Rb.

Figure 20 – Experimental and theoretical curves for amplitude and splitting of the doublet as a function of square root intensity or Rabi frequency of the strong field. Red circles/lines: weak beam scanning (δ_{23}); Green triangles/lines: strong beam scanning (δ_{12}). (a) and (d) are the experimental results. (b) and (e) are the theoretical results for a closed system, while (c) and (f) are the same results for an open system.

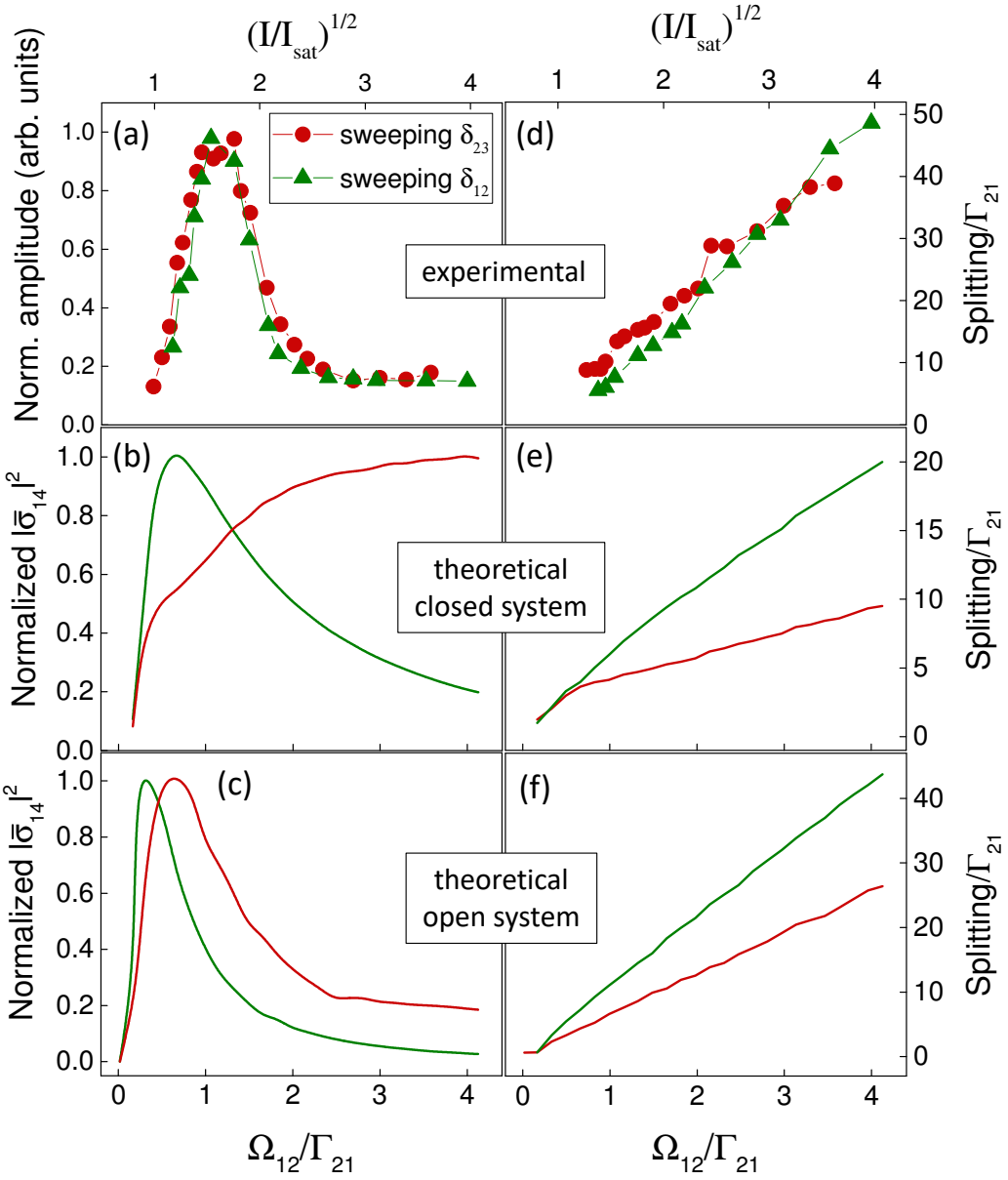

Source: Ref. [59].

However, if the repetition rate of the pulsed laser is carefully chosen, something else can occur: another optical mode can have a frequency near the first transition $5S_{1/2}$ to $5P_{3/2}$ and then induce the FWM process without the participation of the continuous wave laser 22. This is the case we want to discuss now.

In this scenario, we are interested in the frequency scanning scheme in which the repetition rate of the fs laser varies while the diode laser has a fixed frequency. In particular, we scan the repetition rate around $f_R^0 = 987749.886$ MHz at a temperature of $T = 74^o$C. With these specific parameters, we present the CBL signal in Fig. 21 as a function of the repetition rate of the frequency comb. Recall that for a change of $\approx$ 2.5 kHz in the repetition rate the optical frequency variation is equal to an integer multiple of f_R (see Eq. 75), meaning that in Fig. 21 the range δf_R encloses two adjacent modes of the pulsed laser, similarly to Fig. 10.

In this graph, we present the curves for three different values of the diode laser intensity, showcasing the doublet structure due to the dynamic Stark shift with the features we have previously discussed. However, there is an additional intriguing feature present: a narrow peak that appears superimposed on the broader AT peaks, as indicated by the arrows in Fig. 21. This narrow peak is observed depending on the value of the repetition rate, and a close-up of the doublet structure on the right of the curve (II) is displayed in the upper curve of Fig. 21.

Our task now is to verify if this narrow peak is caused by the fact that, for this particular repetition rate, there are two resonant modes of the pulsed laser, one in the first transition, and another in the second transition. To do this, we use our theoretical model considering that the first two transitions can be driven by different routes: (i) two modes of the frequency comb, ω_n and ω_m (*fs-fs* pathway) and/or (ii) by the continuous wave laser and one of the frequency comb modes, ω_d and ω_m (*cw-fs* pathway).

As before, we solve the set of Bloch equations non-perturbatively considering each excitation route separately. This time, instead of using the fourth-order Runge-Kutta method, we experimented with applying a cofactor expansion method on the system's matrix similarly to the example of section 2, which yields similar results. Our variable of interest is still the coherence σ_{14}. After obtaining the full solution for the elements of the

Figure 21 – Coherent blue light intensity as a function of the repetition rate variation (δf_R), for different intensities of the diode laser as indicated in each curve. The diode frequency is fixed near the closed transition and δf_R = 0 for f_R = 987.749 886 MHz. The upper curve is a zoom of the right structure in the curve (II).

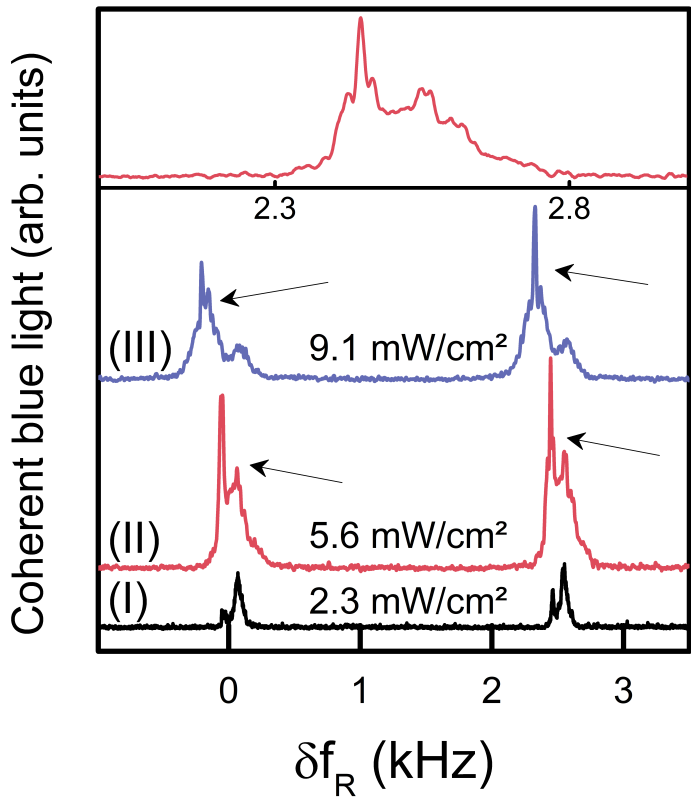

Source: The author (2023).

Figure 22 – Theoretical model considering the two resonant lasers in the first transition

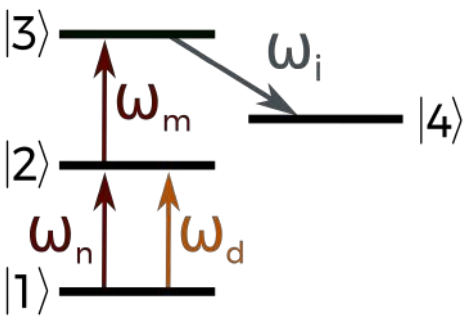

Source: The author (2023).

Figure 23 – Theoretical results scanning the repetition rate for a fixed diode frequency. $\left|\rho_{14}^{dm}\right|^2$ is the result for the *cw-fs* pathway, while $\left|\rho_{14}^{nm}\right|^2$ accounts for the *fs-fs* pathway considering the same repetition rate of Fig. 21. The green and dashed curves are the two possible ways of adding these coherence pathways.

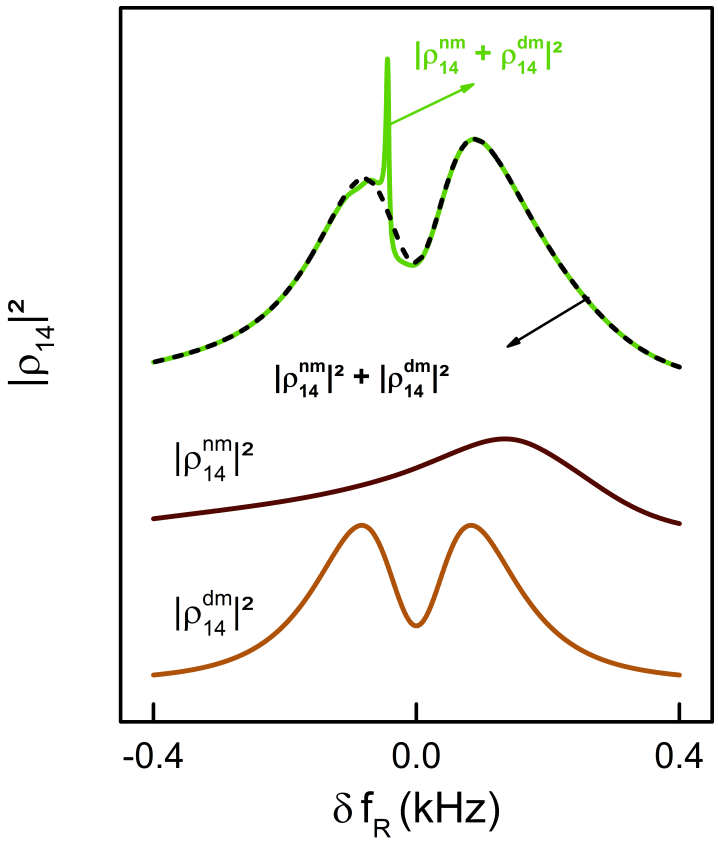

Source: The author (2023).

density matrix, we perform Doppler integration. As an extra approximation, we neglect the phase between velocity groups, that is, we first take the squared modulus of the coherence and then integrate it. This speeds up the calculations and these phases are not crucial for answering the current problem.

In the bottom two curves of Fig. 23, we plot the CBL signal for each excitation route. The parameters are the same as in previous sections, with the same specific repetition rate as the experiment. To consider only the *cw-fs* pathway, we fix the field in the $|1\rangle \rightarrow |2\rangle$ transition. On the other hand, for the *fs-fs* pathway, we scan the first two fields, keeping the frequency difference given by the experimental repetition rate.

The *cw-fs* pathway gives a result similar to previous sections. In contrast, the *fs-fs* result is quite different. Since both fields that induce the first two transitions are scanning, a much broader spectrum arises. This is due to the AT effect caused by the frequency comb mode ω_n, but it is blurred by the other scanning mode. The maximum intensity of

the CBL generated in this case occurs when the system meets the double-resonance condition [91]:

$$f_R = \frac{\omega_{23} - \omega_{12}}{2\pi(m-n)}, \tag{83}$$

where *m* and *n* are integer numbers that determine a pair of comb modes that satisfies the resonant condition for both excitation steps: $|1\rangle \rightarrow |2\rangle$ and $|2\rangle \rightarrow |3\rangle$.

To get the final signal, we must add the two possible coherence pathways. This operation can be done in two ways. Either we assume that these processes are independent, taking the square modulus of each coherence and adding them (dashed curve in Fig. 23) or we say that these coherences may interfere. If that is the case, we must first add the coherences and then take the square modulus of this sum. This leads to the green curve in Fig. 23, with the narrow peak over the AT doublet, just as it is in the experiment.

The narrow interference peak appears to shift from the resonance regarding the $v = 0$ group. It does so because the frequency comb ω_n and the diode laser field must be simultaneously in resonance with the $|1\rangle \rightarrow |2\rangle$ transition for the same group of atoms. For the repetition rate used both in experiment and theory, this condition is satisfied for a group of atoms with some velocity.

It is possible to shift the narrow peak by tuning the repetition rate, as we show in Fig. 24 using our theoretical model. These changes must be in a certain range to ensure that there is still a group of atoms interacting simultaneously with both lasers (the cw laser and two modes of the frequency comb) [92]. If the change in repetition rate is 463.998 kHz (Eq. 83), another pair of modes will be able to produce the same interference pattern, i.e, with similar frequency position and amplitude.

The linewidth of the observed narrow interference peak, of about 10 MHz, is mainly limited by experimental conditions such as the repetition rate scanning. In opposition, the theoretical model shows that the peak has a linewidth of about 1 MHz, a result that appears to be connected with the lifetime of the $5D_{5/2}$ state [93].

Since this is an interference process, the phase must play an important role [94]. While the theory assumes that the lasers are in phase, there was no phase control in the

Figure 24 – Theoretical results scanning the repetition rate for a fixed diode frequency with different repetition rates.

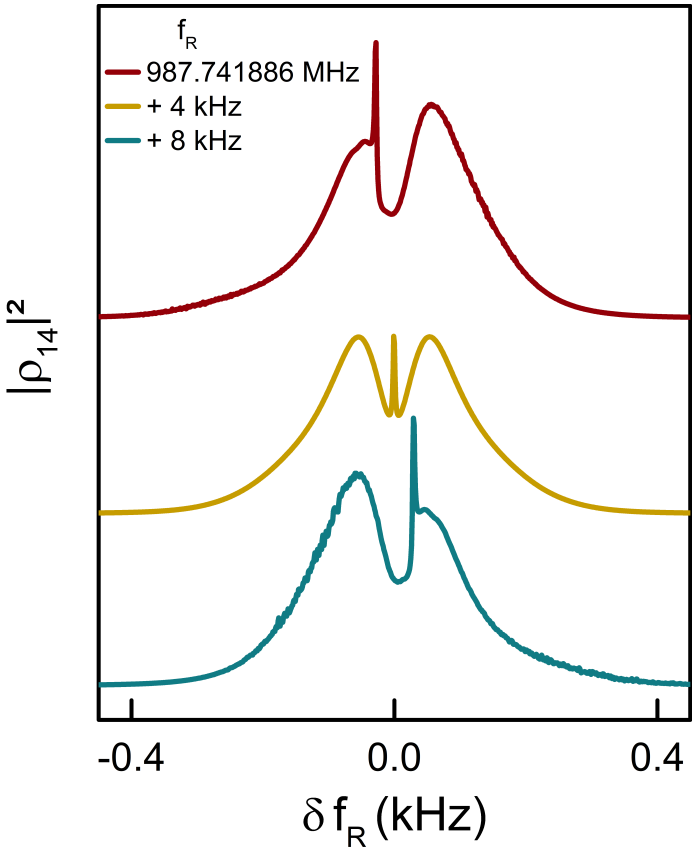

Source: The author (2023).

experiment. This means that we were unable to observe the full range of interference effects, including both constructive and destructive signals (peaks and dips). However, we believe that by locking the phase of the lasers and carefully adjusting the optical path of one of them, it would be possible to shift the narrow peak.

Our numerical analysis suggests that it may also be possible to observe this type of interference using only continuous-wave (cw) lasers. Specifically, we believe that using at least three cw lasers and carefully engineering the frequency scan to vary the frequency of two of them simultaneously could simulate the role played by the mode-locked laser. While using a pulsed laser with a high repetition rate makes it easier to find this interference pattern, it may still be possible to achieve the same results using cw lasers with careful planning.

The results described in this section were published in two regular articles in the Physical Review A [59, 60]:

M. P. M. de Souza, A. A. C. de Almeida, and S. S. Vianna, ‘’Interference effect and Autler-Townes splitting in coherent blue light generated by four-wave mixing”, Phys. Rev. A 99, 043410 (2019).

M. P. M. de Souza, A. A. C. de Almeida, and S. S. Vianna, ‘’Dynamic Stark shift in Doppler-broadened four-wave mixing”, Phys. Rev. A 105, 053128 (2022).

4 DEGENERATE FOUR-WAVE MIXING IN ATOMIC VAPOR: FREQUENCY SHIFT AND PHASE-MATCHING

In this section, we focus on a particular configuration of degenerate four-wave mixing (FWM) that will be our subject henceforth. We investigate an experimental setup with two symmetrical nonlinear signals being generated in rubidium vapor through the copropagating interaction of two laser beams with wave vectors $\mathbf{k}_a$ and $\mathbf{k}_b$. These signals are detected simultaneously in the $2\mathbf{k}_a - \mathbf{k}_b$ and $2\mathbf{k}_b - \mathbf{k}_a$ directions. We observe a single peak in each signal when the input fields are resonant with the ^{85}Rb $5S_{1/2}(F = 3) \rightarrow 5P_{3/2}(F = 4)$ transition. There are reports in the literature of experiments in which all fields are almost resonant with the same optical transition, with the degenerate FWM signals studied considering a pure [95, 96] or degenerate two-level system [97], with one strong field, and arbitrary polarizations of the drive fields [98, 99].

The typical experimental setup for inducing these degenerate FWM processes is with a counterpropagating beam configuration, used to explore the phase-matching obtained when the generated beam is phase-conjugated with the probe beam. In contrast, in our experiment, we employ a copropagating beam configuration and simultaneously detect the transmission of the incident beams and the generated FWM signals. There are also previous published results using a similar scheme with two FWM fields detected simultaneously, but with a non-degenerate system. In this case, the result is that the generated fields with different frequencies, like Stoke and anti-Stokes processes, can be correlated or anticorrelated depending on the incident beams [38]. In our experiment, the degeneracy of the nonlinear process combined with incident beams of the same intensity leads to two symmetric signals, both in space and frequency, regardless of which beam is being scanned.

Although the two signals in our experiment are generated by two separate FWM processes, they provide information about the dynamics of an ensemble of atoms that simultaneously interact with the same drive fields. In a spatially uniform atomic medium, the coherent superposition of the generated fields at different positions along the nonlinear medium must satisfy the well-known phase-matching condition. This condition not only determines the propagation direction of the outgoing FWM field in

terms of the wave vectors of the incident waves but also the frequencies at which the signals will be maximal. Recent studies in a non-degenerate three-level system have shown that the phase-matching condition is crucial for achieving high efficiency in the FWM signal when the excitation fields are detuned from the atomic transition [29]. In that case, with counterpropagating beams, the predominant contributions are attributed to electromagnetically induced absorption (EIA) grating effects [100].

One interesting result in this work is the small frequency separation between the two FWM peaks revealed by the excitation spectra. While it is well known that phase-matching conditions can determine the characteristics of the new fields generated in this nonlinear process, the frequency shift observed in our results is unusual, as it goes in the opposite direction compared to usual cases, where the phase-matching is controlled only by the refractive indices of the field whose frequency is being scanned. Given that we detect the two signals simultaneously, we can distinguish a frequency shift towards the red or blue from each peak associated with the FWM signals, depending on how the beam whose frequency is being swept contributes to the observed signal. Understanding how to effectively control the properties of the atomic media in which the nonlinear process takes place is of widespread interest, not only for fundamental aspects of atom-light interaction but also due to the potential for application in quantum communication and quantum information processing.

To provide supporting arguments for our claims, we have developed a theoretical model using the same basic tools detailed so far. The theoretical results indicate that, for a correct description of the frequency position of each peak, we must solve the Bloch equations including higher-order terms. Moreover, it is crucial to obtain the correct spectra to write the phase-matching conditions including a variable refractive index for both lasers, in which the scanning laser experiences an anomalous window in the refractive index near resonance.

4.1 Experimental setup and results

Let us begin the description of our experimental procedure by presenting a simplified scheme of the setup in Fig. 25(a) together with the hyperfine structure of the

D_2 line of ^{85}Rb. We use two independent cw diode lasers, E_a and E_b, to drive the two FWM processes. These beams E_a and E_b, with wave-vectors $\mathbf{k}_a$ and $\mathbf{k}_b$, respectively, have orthogonal and linear polarizations and they converge inside a 5 cm long cell containing a natural concentration of rubidium atoms at an angle $2\theta \approx 40$ mrad (see Fig. 25(b)). The rubidium cell was heated to $\sim 55\ ^{o}$C to increase the atomic density. Both beams are tuned on the same Doppler line of ^{85}Rb starting in the hyperfine ground state $F = 3$, as shown in the inset of Fig. 25(a). Finally, we use a SAS signal to control and monitor the frequency of each laser.

The acquired data is composed of the four signals: transmission of both incidents beams T_a and T_b and the two FWM signals in the $2\mathbf{k}_a - \mathbf{k}_b$ and $2\mathbf{k}_b - \mathbf{k}_a$ directions, as shown in Fig. 25(b). In this type of forward geometry and with a degenerate process, the clean detection of the signals can be a challenge. There is no longer the option of using bandpass filters as we did in the previous section since all four signals have the same wavelength. In this situation, the main difficulty is that scattered light from one beam may reach the detection position of another beam. To deal with this we take advantage of the linear and orthogonal polarization of the signals and use polarizing beamsplitters before each detector. The incident beams are typically strong allowing the use of regular photodiode detectors to acquire T_a and T_b. On the other hand, the FWM signals are very weak, so we use avalanche photodiodes (*Thorlabs APD120A*) to detect them. Moreover, we use masks to align the input beams within the sample, together with guide laser beams in the direction of the generated signal.

The measurements are carried out by scanning the frequency of one laser through the three allowed hyperfine transitions of rubidium, while the other laser has a fixed frequency. The intensity of the input lasers at the cell entrance is 10-100 times the saturation intensity of the cyclic transition $5S_{1/2}(F = 3) \rightarrow 5P_{3/2}(F = 4)$. The absorption is increased due to the temperature of the vapor, but not enough to completely absorb the fields E_a and E_b, so we are operating in a high-intensity regime.

A typical experimental result is in Fig. 26(a), with the transmission of the two beams T_a and T_b and the two generated FWM signals, $2\mathbf{k}_a - \mathbf{k}_b$ and $2\mathbf{k}_b - \mathbf{k}_a$, as a function of the detuning ($\delta_a/2\pi$) of the scanning field E_a. We chose the intensities of the input fields E_a and E_b at the cell entrance to be approximately the same ($I \sim$50 mW/cm^2)

Figure 25 – (a) Experimental setup with relevant energy levels of ^{85}Rb. PBS and HWP indicate polarizing beamsplitter and half wave-plate, $\mathbf{k}_a$ and $\mathbf{k}_b$ are the wave-vectors of the E_a and E_b beams and $2\mathbf{k}_a - \mathbf{k}_b$ and $2\mathbf{k}_b - \mathbf{k}_a$ indicate the directions of the two detected FWM signals. (b) Schematic representation of phase-matching for the generation of the two FWM signals.

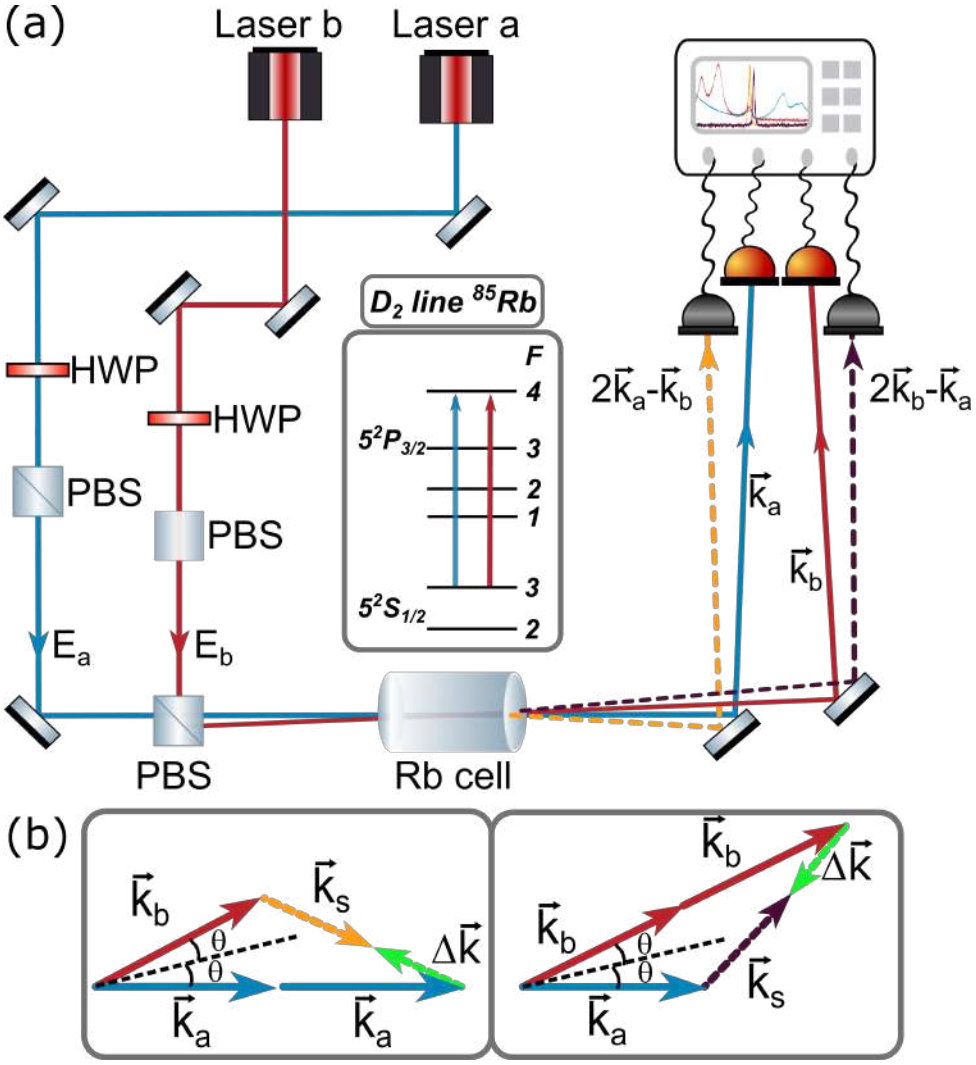

Source: Ref. [101].

and the frequency of E_b beam was fixed near the center of the Doppler broadened spectrum. It is important to state that the fixed-frequency laser was not locked in frequency. However, since we are dealing with an atomic vapor, as long as the laser is inside the Doppler-broadened frequency range there will be atomic velocity groups to interact with the laser. In this graph, all curves are independently normalized to ease the comparison and we define the frequency detuning to the $5S_{1/2}(F=3) \rightarrow 5P_{3/2}(F=4)$ closed transition.

One notices in the transmission signals that there are three peaks in each curve. The frequency difference between these peaks matches the hyperfine transitions from

Figure 26 – (a) Experimental result presenting the transmission of the two incident beams and the two generated FWM signals as a function of δ_a. (b) Boxes I and II show the transitions from the ground state ^{85}Rb $F = 3$, involved on each peak of the transmission signals.

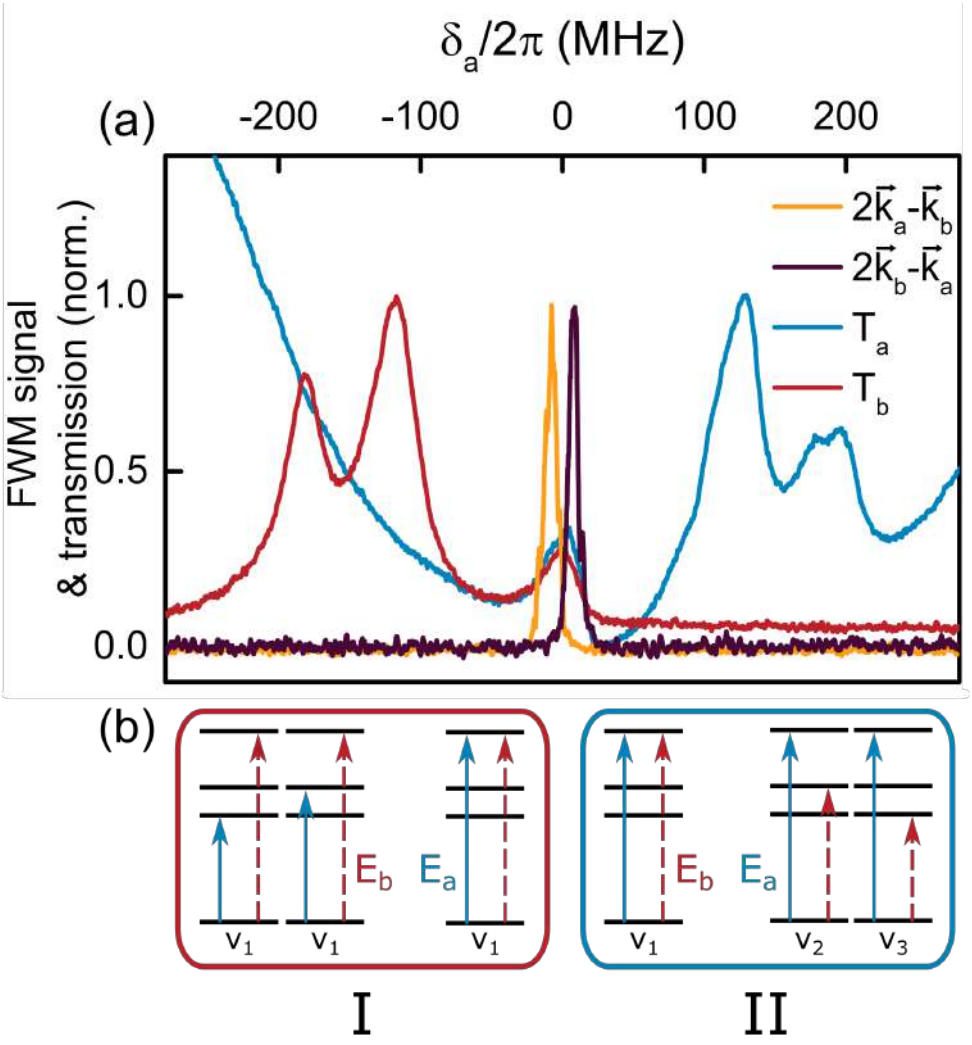

Source: Ref. [101].

the ground state $F = 3$ of ^{85}Rb. Moreover, these peaks only appear in the spectra due to the simultaneous interaction of the two incident fields with the atomic medium. The presence of these sub-Doppler peaks comes from the so-called velocity selective optical pumping (VSOP) [102], and they have been studied when the transmission of a weak beam is measured in the presence of a strong fixed frequency field. In our experiment, the configuration is slightly different, as we measure the transmission of the two beams with both of them strong.

The peaks in the transmission curve of the fixed frequency laser appear in the order of increasing energy as if the hyperfine energy structure is being directly probed. However, this is not the case for the transmission of the scanning frequency laser. This

can be explained by considering the different groups of atoms with different velocities that interact with the lasers. The field E_b causes a closed transition ($5S_{1/2}(F=3) \rightarrow 5P_{3/2}(F=4)$) for a group of atoms with velocity v_1, as shown by the dashed lines in the box I of Fig. 26(b). As the frequency of E_a is scanned, it induces each one of the allowed transitions, resulting in a reduction in the absorption of the field E_b at specific frequencies, leading to the peaks in the T_b curve.

On the other hand, for the transmission signal T_a the field E_b now selects three groups of atoms with velocities v_1, v_2 and v_3, promoting the transition to the excited states $F=4$, $F=3$ and $F=2$, respectively. Once again, as we scan E_a, it will have the resonance frequency of the closed transition, as box II indicates in Fig. 26(b). For each velocity group, the optical pumping due to E_b lowers the absorption of E_a and generates the three peaks in the opposite order of increasing energy [103, 102, 68].

We obtain an FWM signal due to a degenerate process when both fields interact with the velocity group v_1. In this case, as shown in Fig. 26(b), the two incident fields induce a closed transition to the excited state $F=4$. Additionally, there is a noticeable frequency shift between the two FWM signals in Fig. 26(a). This shift is somewhat unexpected because both processes are nearly identical, meaning that the output signals should not have different frequency positions in the spectrum. We hypothesize that this shift is caused by phase-matching conditions enclosing a steep variation of the refractive index due to the interaction of the medium with both incident beams. This kind of behavior of the refractive index has also been observed in some coherent effects such as EIA [104]. We provide further support for this hypothesis in the subsection on theoretical results.

In some of our experimental configurations, we could also observe the presence of the EIA phenomenon. We present one of the transmission curves and the two correspondent FWM signals in Fig. 27. In this case, the ratio between the intensities of the incident beams is ≈ 3, with E_a being more powerful. In Fig. 27(a), we scan the frequency of the field E_a while E_b has a fixed frequency and vice versa for Fig. 27(b).

Since the FWM signals are related to the same incident fields, involving only an interchange of the role of each beam, they present the same intensity relation given

Figure 27 – Measurements of T_a and FWM signals as a function of the frequency detuning of the scanning beam, for a ratio intensity of incident beams of three. (a) Curves for E_a scanning and E_b fixed in frequency. (b) Curves for E_b scanning and E_a fixed in frequency. Insets, zoom of the peak corresponding to the cyclic transition on the T_a curve in each measurement.

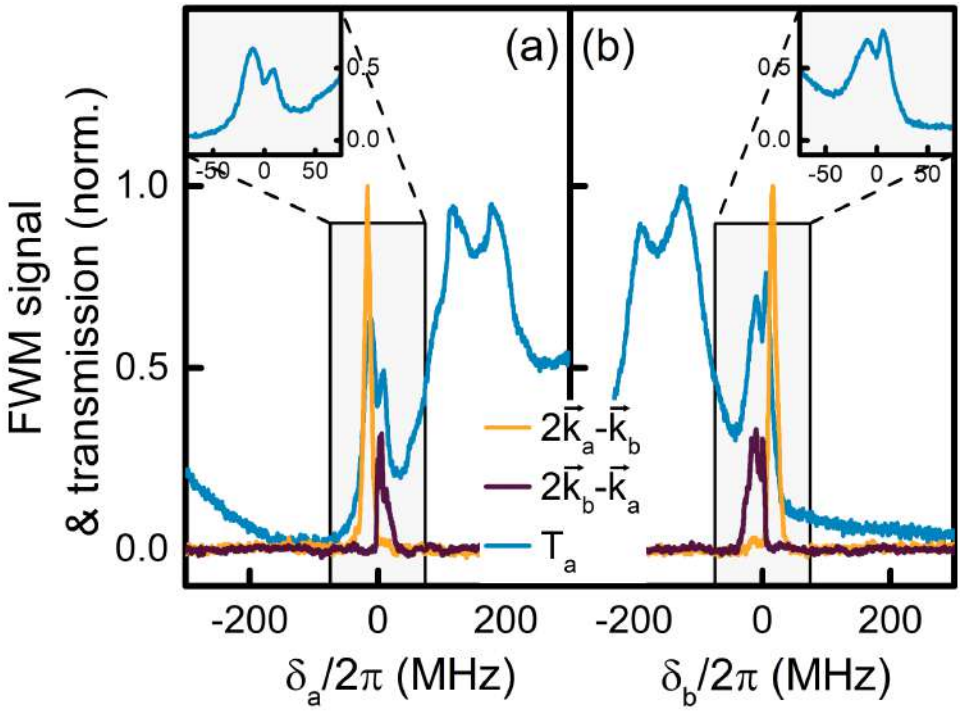

Source: Ref. [101].

by the incident beams. Hence, we normalize the FWM signals using the highest value between them to ease the interpretation of the graph. As in Fig. 26(a), these generated signals appear again with a small frequency separation. However, in Fig. 27, we notice an interchange in the frequency positions depending on which beam is scanning. The relative frequency position of the signal $2\mathbf{k}_a - \mathbf{k}_b$ remains the same concerning the peak corresponding to the cyclic transition in T_a curve (see Figs. 26 and 27). The same occurs for the $2\mathbf{k}_b - \mathbf{k}_a$ signal in relation to the peak corresponding to the cyclic transition in T_b curve.

An interesting feature of Fig. 27 is in the insets: the presence of a narrow absorption dip inside the cyclic transition peak in the T_a curve. This absorption dip occurs in the middle of the two nonlinear signals which indicates that both lasers are resonant with the closed transition. The narrow dip is the signature of an EIA-type process [105] and it is easier to observe when one of the beams is more intense than the other, as in Fig. 27.

EIA is a nonlinear optical effect that occurs in the presence of two resonant driving fields interacting with the same ground-state hyperfine level of an atomic sample. If the system ground state has a lower total angular momentum than the excited state, then the system might exhibit a narrow peak in an absorption spectrum indicating the EIA phenomenon. In this sense, EIA is an analog phenomenon to EIT, but with the opposite effect. It was first observed in atomic vapors by Akulshin et al. in 1998 [24] and has since been an object of several studies since then.

EIA has several interesting and useful applications in a variety of fields, especially for techniques that rely on steep variations of the absorption or the refractive index of an atomic medium. In our experimental configuration, this phenomenon can also be detected in a regime where both lasers are strong [106], like in the following results. There is also an EIA dip in the other two peaks of the transmission curves, although they are quite smaller.

Finally, to complete our experimental analysis, we examine the FWM spectra for four different intensities of the incident laser beams. To obtain these measurements, we scan the frequency of one of the fields (E_a) while keeping the frequency of the other field (E_b) fixed. As the intensity of the input laser increases, we observe a power-broadening effect in the FWM signals, as well as an increase in the frequency separation between them. However, this increase in frequency separation appears to saturate for intensities above 200 mW/cm^2. Additionally, we noticed an asymmetry in the signal that becomes more pronounced at higher intensities. These findings are depicted in Fig. 28.

4.2 Theoretical model

We follow a similar procedure to model the FWM process as we did in the previous section. Naturally, there are some adaptations to this particular experimental scenario. The first is that the energy level structure is different as we are dealing with a degenerate process. One could then assume that a simple two-level system would fit to model this type of FWM process. However, this is not the case due to the polarizations of the input fields. They have linear and orthogonal polarizations and therefore can be

Figure 28 – Behavior of the two FWM signals at different intensities of the beams E_a and E_b at the entrance of the Rb cell. All curves are normalized.

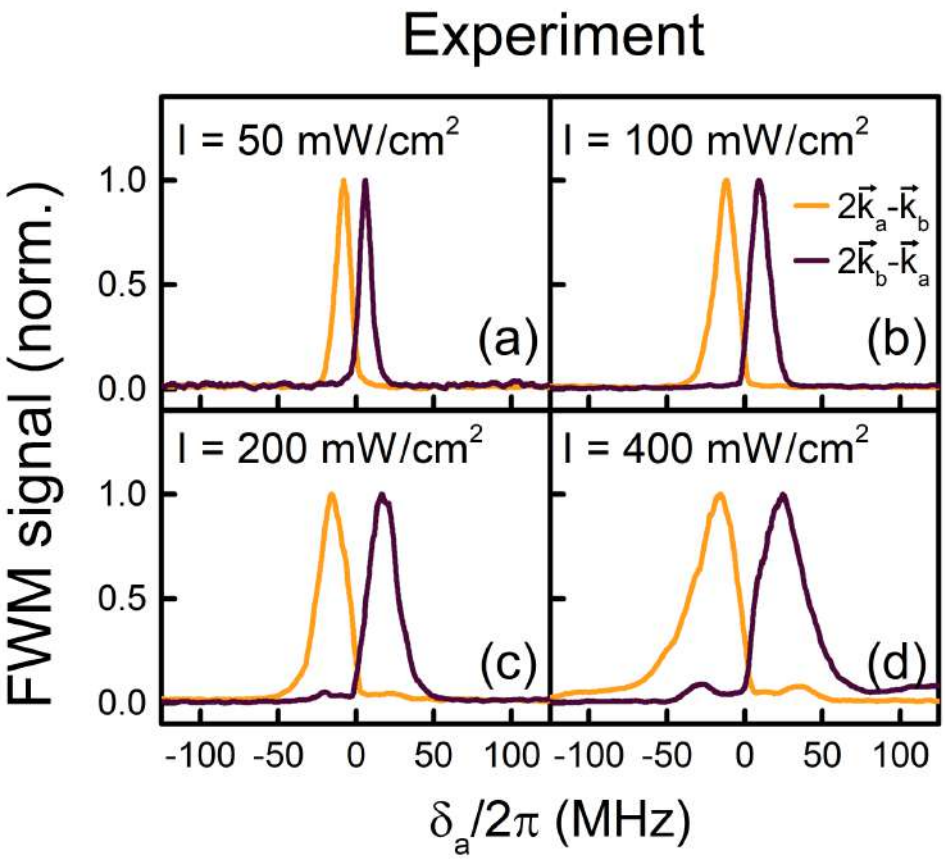

Source: Ref. [101].

written on a circular basis as

$$\begin{aligned}\mathbf{E}_a &= \left[\varepsilon_a(t)e^{-i(\omega_a t - k_a z)} + c.c.\right]\frac{(\hat{\sigma}^+ + \hat{\sigma}^-)}{\sqrt{2}};\\ \mathbf{E}_b &= \left[\varepsilon_b(t)e^{-i(\omega_b t - k_b z)} + c.c.\right]\frac{(i\hat{\sigma}^+ - i\hat{\sigma}^-)}{\sqrt{2}},\end{aligned} \tag{84}$$

where ε_l is the amplitude of the electric field; ω_l is the optical frequency, and $\mathbf{k}_l$ is the associated wave-vector.

We chose to write the polarization vector in the circular base as it highlights how these fields interact with Zeeman sublevels. This means that our quantization axis is in the direction of propagation. Naturally, we are considering for now that the beams are copropagating, as the angle between them in the experiment is very small.

The circular components can only induce σ transition in the Zeeman sublevels,

Figure 29 – Zeeman sublevels of $|F = 2\rangle \rightarrow |F' = 3\rangle$ and the allowed transitions for the experimental input laser beams. Blue arrows indicate σ^- transitions while red arrows indicate σ^+ transitions.

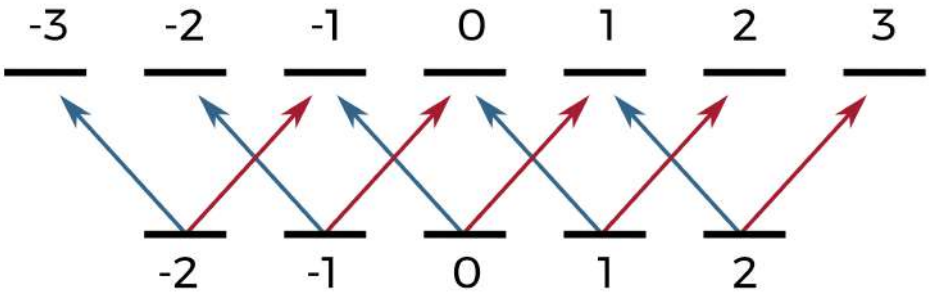

Source: The author (2023).

due to the selection rules. We detail these levels within the closed transition $|F = 2\rangle \rightarrow |F' = 3\rangle$ in Fig. 29 together with the possible transitions the input beams can induce.

As a consequence of this energy-level structure, FWM generation could be modeled by an effective three-level system. Notice that if the choice in the quantization axis is different the energy level structure might be different, even though the final result is the same. For instance, if one chooses as the quantization axis the polarization direction of one of the input beams. Then this input beam would induce π transitions and the basic level structure for generating the FWM process would be a four-level system. However, we choose to work with a three-level system as it leads to a smaller set of coupled Bloch equations.

The same three-level system can be replicated throughout the Zeeman sublevels, leading to several FWM processes happening simultaneously. These multiple processes must add with the appropriate phases to build up the final signal with proper linear polarization. Therefore, the basic systems behind each component of the two FWM signals we want to study are presented in Fig. 30.

Finally, notice that the theoretical treatment would be much simpler if we could use a two-level system. However, this scenario would only be possible if in the experiment the input laser fields had only parallel circular components, as we did in the previous section. On the other hand, this would lead to a much harder detection in the experiment, as all four acquired signals would have the same polarization and the scattered light would not be easily filtered out by the polarizers in the experiment. So we chose this compromise to achieve better experimental results.

Figure 30 – Three-level theoretical model with (a) and (b) being the processes that generate the two circular components of the signal, with frequency ω_s, in the $2\mathbf{k}_a - \mathbf{k}_b$ direction; (c) and (d) are analogous to the $2\mathbf{k}_b - \mathbf{k}_a$ direction.

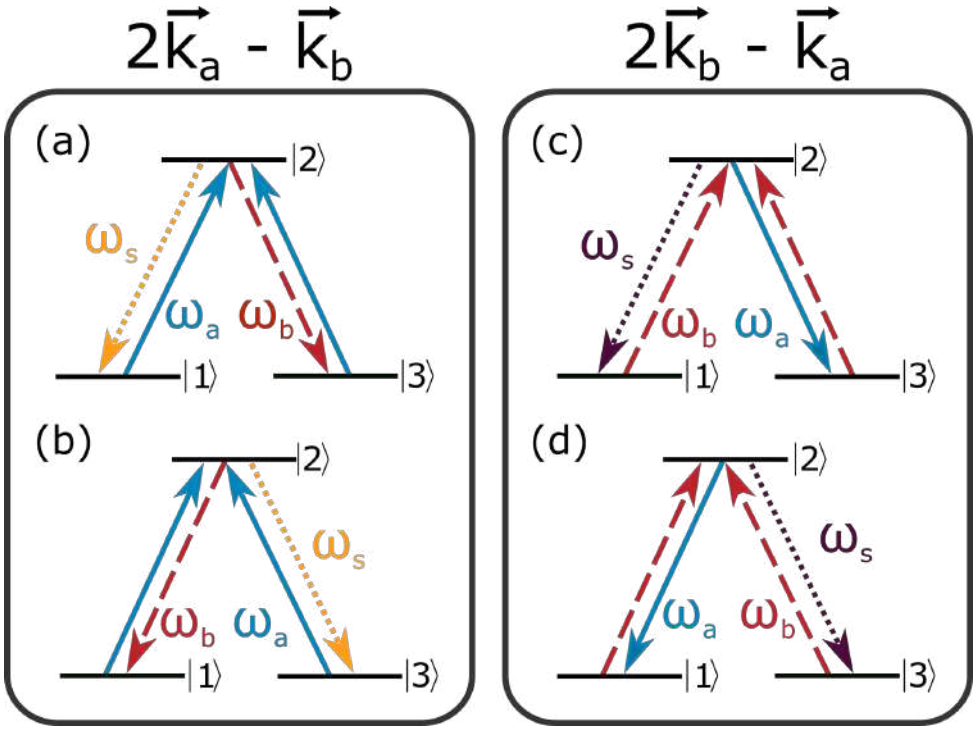

Source: Ref. [101].

Since our main hypothesis for the frequency shift between the FWM signals is connected to the phase-matching conditions, only solving the set of coupled Bloch equations as in the previous section will not be sufficient. We must consider the propagation of the fields within the atomic sample. To do so, we must solve the Bloch equations self-consistently with the Maxwell equations. The FWM signals of interest are in the $2\mathbf{k}_a - \mathbf{k}_b$ and $2\mathbf{k}_b - \mathbf{k}_a$ directions, so we calculate the induced coherence ρ_{13} between the two ground states $|1\rangle$ and $|3\rangle$ in all orders of the incident fields and then add the interaction with one of the fields, either E_a or E_b, to generate the ρ'_{21} or ρ'_{23} coherences at the frequencies $\omega_s = 2\omega_a - \omega_b$ and $\omega_s = 2\omega_b - \omega_a$, respectively. For each direction, both coherences ρ'_{21} and ρ'_{23} contribute to the generated signal, each one behind a certain circular component of the signal, as shown in Figs. 30(a) and (b).

The joint contribution of the two coherences to the FWM signal in each direction can be considered equivalent to the scattering of the two circular components of each field E_a or E_b by the coherence ρ_{13}. As the fields co-propagate at a small angle, the scattered fields will travel in different directions.

Figure 31 – Simplified three-level theoretical model with a single field in each transition.

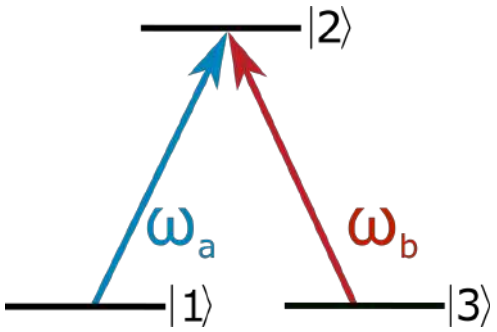

Source: The author (2023).

We can model both signals generated in the experiment with the same set of equations. Therefore, we choose to derive the equations that describe the $2\mathbf{k}_a - \mathbf{k}_b$ process. A further approximation is to treat transition with only field, effectivelly modelling the system from Fig. 31. We then extrapolate the expressions for each FWM signal from this set of equations. In this case, the Bloch equations, obtained with a similar hamiltonian of section 2, with the rotating wave approximation, and in the steady state, can be written as:

$$
\begin{aligned}
\rho_{11} &= \frac{-i\sigma_{12}\Omega_a + i\sigma_{21}\Omega_a^* + \Gamma_{21}\rho_{22} + \gamma'\rho_{11}^0}{\gamma'};\\
\rho_{22} &= \frac{i\sigma_{12}\Omega_a - i\sigma_{21}\Omega_a^* - i\sigma_{23}\Omega_b^* + i\sigma_{32}\Omega_b}{\Gamma_{21} + \Gamma_{23} + \gamma'};\\
\rho_{33} &= \frac{i\sigma_{23}\Omega_b^* - i\sigma_{32}\Omega_b + \Gamma_{23}\rho_{22} + \gamma'\rho_{33}^0}{\gamma'};\\
\sigma_{12} &= \frac{-i(\rho_{11} - \rho_{22})\Omega_a^* - i\sigma_{13}\Omega_b^*}{i\delta_a + \gamma_{12} + \gamma'};\\
\sigma_{13} &= \frac{-i\sigma_{12}\Omega_b + i\sigma_{23}\Omega_a^*}{i\delta_a - i\delta_b + \gamma_{13} + \gamma'};\\
\sigma_{32} &= \frac{-i(\rho_{33} - \rho_{22})\Omega_b^* - i\sigma_{13}\Omega_a^*}{i\delta_b + \gamma_{32} + \gamma'}.
\end{aligned}
\tag{85}
$$

The σ_{jk} terms are the coherences in the rotating frame, whereas Γ_{jk} are the decay rates of the populations; the Rabi frequency has been redefined to include the spatial phase $\Omega_l = \tilde{\Omega}_l e^{i\mathbf{k}_l\cdot\mathbf{r}}$; δ_l is the detuning of each laser to the $|j\rangle \rightarrow |k\rangle$ transition; ρ_{jj}^0 are the populations in the absence of the fields and represent the terms that compensate the loss of atoms from the interaction region with an arrival of new atoms in the ground state at a rate γ'. The missing coherence equations are the complex conjugate of the

ones presented.

One may obtain the coherence σ_{13} through algebraic manipulations, although the final expressions are intricate [54]. We will write the beginning of this analytical solution, but the final expressions will be achieved with the help of a linear algebra suite (see the *Mathematica* notebook in the Appendix B). We begin isolating the σ_{13} equation from Eq. 85 and substituting the one-photon coherences

$$\sigma_{13} = \frac{-i\sigma_{12}\Omega_b + i\sigma_{23}\Omega_a^*}{i\delta_a - i\delta_b + \gamma_{13} + \gamma'};$$
$$\sigma_{13} = \frac{-i\left(\frac{-i(\rho_{11}-\rho_{22})\Omega_a^* - i\sigma_{13}\Omega_b^*}{i\delta_a+\gamma_{12}+\gamma'}\right)\Omega_b + i\left(\frac{-i(\rho_{33}-\rho_{22})\Omega_b^* - i\sigma_{13}\Omega_a^*}{i\delta_b+\gamma_{32}+\gamma'}\right)\Omega_a^*}{i\delta_a - i\delta_b + \gamma_{13} + \gamma'}.$$

After simplification, we may write the coherence of interest with a dependency on the population terms of the density matrix. The population terms are obtained through a Gaussian elimination of the system of equations

$$\sigma_{13} = \frac{-\tilde{\Omega}_a^*\tilde{\Omega}_b\left[\frac{(\rho_{11}-\rho_{22})}{(i\delta_a+\gamma_{12}+\gamma')} + \frac{(\rho_{33}-\rho_{22})}{(-i\delta_b+\gamma_{23}+\gamma')}\right]e^{-i(\mathbf{k}_a-\mathbf{k}_b)\cdot\mathbf{r}}}{i\delta_a - i\delta_b + \gamma_{13} + \gamma' + \frac{|\Omega_b|^2}{i\delta_a+\gamma_{12}+\gamma'} + \frac{|\Omega_a|^2}{-i\delta_b+\gamma_{23}+\gamma'}}. \tag{86}$$

With the complete set of solutions of the Bloch equations, we write the coherences σ'_{21} and σ'_{23}. These terms are connected with the FWM field with frequency $\omega_s = 2\omega_a - \omega_b$ and wave-vector $\mathbf{k}_s$ in the direction of $2\mathbf{k}_a - \mathbf{k}_b$. We can extrapolate them from the set of Eqs. 85 in the form of

$$\sigma'_{21} = \frac{i(\rho_{11}-\rho_{22})\tilde{\Omega}_s e^{ik_s z}}{-i(2\delta_a - \delta_b) + \gamma_{12} + \gamma'} + \frac{i\tilde{\sigma}_{31}\tilde{\Omega}_a e^{i(2k_a-k_b)z}}{-i\delta_a + \gamma_{12} + \gamma'}; \tag{87}$$
$$\sigma'_{23} = \frac{i(\rho_{33}-\rho_{22})\tilde{\Omega}_s e^{ik_s z}}{-i(2\delta_a - \delta_b) + \gamma_{32} + \gamma'} + \frac{i\tilde{\sigma}_{31}\tilde{\Omega}_a e^{i(2k_a-k_b)z}}{-i\delta_a + \gamma_{32} + \gamma'}, \tag{88}$$

where the coherence $\tilde{\sigma}_{31}$ is the complex conjugate of Eq. 86 without the spatial dependency. Henceforth, we neglect the transversal components in the spatial terms, projecting the fields in the $\hat{z}$ direction, taken to be the bisector between the incident fields (see Fig. 25(b)), i.e., $\mathbf{k}_l \cdot \mathbf{r} \approx k_l z$. Moreover, it is worth noting that this procedure

of considering all the important contributions to σ_{13} that can affect the response of the medium is present in some studies of EIT [23] and EIA [25],

If one assumes the phase-matching conditions to be satisfied, i.e. $\Delta\mathbf{k} = 2\mathbf{k}_a - \mathbf{k}_b - \mathbf{k}_s = 0$ then the final FWM signals would be proportional to the square of the sum $\sigma'_{21} + \sigma'_{23}$. However, as we discussed, we need to propagate the fields within the sample to obtain the observed experimental features, namely asymmetry and frequency separation. Let us find then the generated electric field $E_s(z,t) = \varepsilon_s(z,t)\, e^{-i(\omega_s t - k_s z)} + c.c.$. Consider the wave equation (see Eq. 16)

$$\frac{\partial^2 E_s(z,t)}{\partial z^2} - \frac{1}{c^2}\frac{\partial^2 E_s(z,t)}{\partial t^2} = \frac{1}{\varepsilon_0 c^2}\frac{\partial^2 P_s(t)}{\partial t^2}, \tag{89}$$

where P is the macroscopic polarization, that is, the dipole moment per unit volume. In this last step, we also neglected the transversal spatial derivatives. The polarization is given in terms of the off-diagonal elements of the density matrix [49]

$$P_s(t) = N\mathrm{Tr}(\hat{\rho}\hat{\mu}) = N(\mu_{12}\rho_{21} + \mu_{32}\rho_{23} + c.c.), \tag{90}$$

where N is the number density of atoms. The polarization P can be written in terms of a complex amplitude that oscillates with the frequency of the field

$$P_s(t) = \mathscr{P} e^{-i\omega_s t} + c.c. \tag{91}$$

We can then rewrite the wave equation keeping only the terms that oscillate with $e^{-i\omega_s t}$

$$\frac{\partial^2}{\partial z^2}\left[\varepsilon_s(z,t)\, e^{-i(\omega_s t - k_s z)}\right] - \frac{1}{c^2}\frac{\partial^2}{\partial t^2}\left[\varepsilon_s(z,t)\, e^{-i(\omega_s t - k_s z)}\right] = \frac{1}{\varepsilon_0 c^2}\frac{\partial^2}{\partial t^2} N(\mu_{12}\rho_{21} + \mu_{32}\rho_{23}). \tag{92}$$

Let us treat each term individually

$$\frac{\partial^2}{\partial z^2}\left[\varepsilon_s(z,t)\,e^{-i(\omega_s t-k_s z)}\right] = -k_s^2\varepsilon_s(z,t)\,e^{-i(\omega_s t-k_s z)} + 2ik_s e^{-i(\omega_s t-k_s z)}\frac{\partial}{\partial z}\varepsilon_s(z,t) \tag{93}$$

$$+ e^{-i(\omega_s t-k_s z)}\cancel{\frac{\partial^2}{\partial z^2}\varepsilon_s(z,t)}; \tag{94}$$

$$\frac{\partial^2}{\partial t^2}\left[\varepsilon_s(z,t)\,e^{-i(\omega_s t-k_s z)}\right] = -\omega_s^2\varepsilon_s(z,t)\,e^{-i(\omega_s t-k_s z)} - 2i\omega_s e^{-i(\omega_s t-k_s z)}\cancel{\frac{\partial}{\partial t}\varepsilon_s(z,t)}^{0} \tag{95}$$

$$+ e^{-i(\omega_s t-k_s z)}\cancel{\frac{\partial^2}{\partial t^2}\varepsilon_s(z,t)}^{0}\quad; \tag{96}$$

$$\frac{1}{\varepsilon_0 c^2}\frac{\partial^2}{\partial t^2}N(\mu_{12}\rho_{21}+\mu_{23}\rho_{32}) = -\frac{N\omega_s^2}{\varepsilon_0 c^2}(\mu_{12}\sigma_{21}+\mu_{32}\sigma_{23})\,e^{-i\omega_s t}. \tag{97}$$

In the spatial derivative, we use the slowly varying amplitude approximation to neglect the second-order derivative

$$\left|\frac{\partial^2\varepsilon_s(z,t)}{\partial z^2}\right| \ll \left|k_s\frac{\partial\varepsilon_s(z,t)}{\partial z}\right|. \tag{98}$$

As for the time derivatives, we are treating the system in a steady state so they all go to zero. By collecting all the terms and substituting them back into the wave equation we get

$$\begin{aligned} -k_s^2\varepsilon_s(z)\,e^{ik_s z} + 2ik_s e^{ik_s z}\frac{\partial}{\partial z}\varepsilon_s(z) + \frac{\omega_s^2}{c^2}\varepsilon_s(z)\,e^{ik_s z} &= -\frac{N\omega_s^2}{\varepsilon_0 c^2}(\mu_{12}\sigma_{21}+\mu_{32}\sigma_{23}); \\ 2ik_s\frac{\partial}{\partial z}\varepsilon_s(z) &= -\frac{N\omega_s^2}{\varepsilon_0 c^2}(\mu_{12}\sigma_{21}+\mu_{32}\sigma_{23})\,e^{-ik_s z}; \\ \frac{\partial}{\partial z}\tilde{\Omega}_s(z) &= \frac{i|\mu|^2 N\omega_s}{2\varepsilon_0\hbar c}(\sigma_{21}+\sigma_{23})\,e^{-ik_s z}. \end{aligned} \tag{99}$$

where $\tilde{\Omega}_s$ is the Rabi frequency of the FWM field and we consider $\mu_{12}=\mu_{32}=\mu$ since the system is symmetrical. Finally, we substitute the coherences of Eq. 87 into the wave

equation

$$\begin{aligned}\frac{\partial}{\partial z}\tilde{\Omega}_s(z) =& \frac{i|\mu|^2 N\omega_s}{2\varepsilon_0\hbar c}\left(\frac{i(\rho_{11}-\rho_{22})\tilde{\Omega}_s}{-i(2\delta_a-\delta_b)+\gamma_{12}+\gamma'}+\frac{i\tilde{\sigma}_{31}\tilde{\Omega}_a e^{i\Delta kz}}{-i\delta_a+\gamma_{12}+\gamma'}\right.\\ &\left.+\frac{i(\rho_{33}-\rho_{22})\tilde{\Omega}_s}{-i(2\delta_a-\delta_b)+\gamma_{32}+\gamma'}+\frac{i\tilde{\sigma}_{31}\tilde{\Omega}_a e^{i\Delta kz}}{-i\delta_a+\gamma_{32}+\gamma'}\right);\\ =&-\frac{|\mu|^2 N\omega_s}{2\varepsilon_0\hbar c}\left(\left[\frac{(\rho_{11}-\rho_{22})}{-i(2\delta_a-\delta_b)+\gamma_{12}+\gamma'}+\frac{(\rho_{33}-\rho_{22})}{-i(2\delta_a-\delta_b)+\gamma_{32}+\gamma'}\right]\tilde{\Omega}_s\right.\\ &\left.+\left[\frac{\tilde{\sigma}_{31}\tilde{\Omega}_a}{-i\delta_a+\gamma_{12}+\gamma'}+\frac{\tilde{\sigma}_{31}\tilde{\Omega}_a}{-i\delta_a+\gamma_{32}+\gamma'}\right]e^{i\Delta kz}\right);\\ =&X^{(1)}\tilde{\Omega}_s+X^{(3)}e^{i\Delta kz},\end{aligned} \tag{100}$$

where we used the couplings $X^{(1)}$ and $X^{(3)}$ that are proportional the the first-order and third-order susceptibilities. We define them as

$$X^{(1)} \equiv -\frac{|\mu|^2 N\omega_s}{2\varepsilon_0\hbar c}\left[\frac{(\rho_{11}-\rho_{22})}{-i(2\delta_a-\delta_b)+\gamma_{12}+\gamma'}+\frac{(\rho_{33}-\rho_{22})}{-i(2\delta_a-\delta_b)+\gamma_{32}+\gamma'}\right]; \tag{101}$$

$$X^{(3)} \equiv -\frac{|\mu|^2 N\omega_s}{2\varepsilon_0\hbar c}\left[\left[\frac{\tilde{\sigma}_{31}\tilde{\Omega}_a}{-i\delta_a+\gamma_{12}+\gamma'}+\frac{\tilde{\sigma}_{31}\tilde{\Omega}_a}{-i\delta_a+\gamma_{32}+\gamma'}\right]\right]. \tag{102}$$

We solve this differential equation for the Rabi frequency of the FWM field in the non-depleted input approximation, i.e., we assume that the input fields E_a and E_b are strong enough to allow us to neglect their absorption. To find the solution, we first define $\Omega_s' \equiv \Omega_s e^{-i\Delta kz}$. Then

$$\frac{\partial\Omega_s}{\partial z} = \frac{\partial}{\partial z}\Omega_s' e^{i\Delta kz} = X^{(3)}e^{i\Delta kz} + X^{(1)}\Omega_s; \tag{103}$$

$$\cancel{e^{i\Delta ky}}\frac{\partial}{\partial z}\Omega_s' + i\Delta k\Omega_s'\cancel{e^{i\Delta kz}} = X^{(3)}\cancel{e^{i\Delta kz}} + X^{(1)}\Omega_s'\cancel{e^{i\Delta ky}}; \tag{104}$$

$$\frac{\partial}{\partial z}\Omega_s' = X^{(3)} + \left(X^{(1)} - i\Delta k\right)\Omega_s'. \tag{105}$$

The general solution is

$$\Omega_s' = c_1 e^{\left(X^{(1)}-i\Delta k\right)z} - \frac{X^{(3)}}{\left(X^{(1)}-i\Delta k\right)}. \tag{106}$$

To determine the constant c_1 we impose the condition $\Omega_s(z=0)=0$, which is a fair condition since no signal must be generated at the very beginning of the sample. Therefore we find that

$$c_1 = \frac{X^{(3)}}{\left(X^{(1)} - i\Delta k\right)}, \tag{107}$$

and consequently, the final solution is

$$\Omega_s = \frac{X^{(3)}}{\left(X^{(1)} - i\Delta k\right)} \left(e^{X^{(1)}z} - e^{i\Delta k z}\right). \tag{108}$$

Notice that if we neglect the first-order coupling, the FWM intensity after propagating through a sample with length L is modulated by the well-known $\mathrm{sinc}^2(\Delta kL)$ [49].

We must turn our attention to the phase-matching conditions at this point. In an FWM process, phase-matching conditions refer to requirements that must be met for the FWM process to occur efficiently. These conditions arise from the momentum and energy conservation and may depend on the wavelengths and polarizations of the incident fields, as well as the properties of the nonlinear medium in which the FWM process takes place.

Several factors can affect the phase-matching conditions in an FWM process. Some of the most important factors include: the refractive indices of the nonlinear medium, as they determine the phase velocities of the incident fields; The dispersion of the nonlinear medium or how the refractive index changes with frequency; and the polarization of the incident fields as different polarizations can couple differently to the nonlinear medium.

In our case, we may calculate the phase-matching conditions in detail using Fig. 25(b). Let us consider that $\Delta k = |\Delta \mathbf{k}|$ hence, for both FWM processes, generated in the $2\mathbf{k}_a - \mathbf{k}_b$ and $2\mathbf{k}_b - \mathbf{k}_a$ directions, and with the field E_b with a fixed frequency while we

scan the field E_a,

$$\begin{aligned}
\Delta k_{2\mathbf{k}_a-\mathbf{k}_b} &= |\mathbf{k}_a+\mathbf{k}_a+\mathbf{k}_b+\mathbf{k}_s| \\
&= 2k_a cos(\theta) - k_b cos(\theta) - k_s cos(3\theta) \\
&= \frac{2n_a\omega_a}{c}cos(\theta) - \frac{n_b\omega_b}{c}cos(\theta) - \frac{n_b\omega_s}{c}cos(3\theta) \\
&= \frac{2n_a\omega_a}{c}cos(\theta) - \frac{n_b\omega_b}{c}cos(\theta) - \frac{n_b(2\omega_a-\omega_b)}{c}cos(3\theta) \\
&= \frac{2n_a\omega_a}{c}cos(\theta) - \frac{n_b\omega_b}{c}cos(\theta) - \frac{2n_b\omega_a}{c}cos(3\theta) + \frac{n_b\omega_b}{c}cos(3\theta) \\
&= \frac{2\omega_a}{c}(n_a cos(\theta) - n_b cos(3\theta)) - \frac{n_b\omega_b}{c}(cos(\theta) - cos(3\theta)) \\
\Delta k_{2\mathbf{k}_b-\mathbf{k}_a} &= |\mathbf{k}_b+\mathbf{k}_b+\mathbf{k}_a+\mathbf{k}_s| \\
&= 2k_b cos(\theta) - k_a cos(\theta) - k_s cos(3\theta) \\
&= \frac{2n_b\omega_b}{c}cos(\theta) - \frac{n_a\omega_a}{c}cos(\theta) - \frac{n_b\omega_s}{c}cos(3\theta) \\
&= \frac{2n_b\omega_b}{c}cos(\theta) - \frac{n_a\omega_a}{c}cos(\theta) - \frac{n_b(2\omega_b-\omega_a)}{c}cos(3\theta) \\
&= \frac{2n_b\omega_b}{c}cos(\theta) - \frac{n_a\omega_a}{c}cos(\theta) - \frac{2n_b\omega_b}{c}cos(3\theta) + \frac{n_b\omega_a}{c}cos(3\theta) \\
&= \frac{2n_b\omega_b}{c}(cos(\theta) - cos(3\theta)) - \frac{\omega_a}{c}(n_a cos(\theta) - n_b cos(3\theta)).
\end{aligned} \tag{109}$$

We write only the phase-matching in the bisector direction between the incident fields, since the perpendicular direction might be neglected as θ is small. This leads to a rather symmetrical result. We also consider the index of refraction for the generated signal as the index of the field with a fixed frequency.

To model the refractive indexes n_a or n_b we use the real part of the electric susceptibilities of the transition with which each laser is resonant. Since these susceptibilities are connected to the coherences that we extract solving the Bloch equations to all orders, we may write the refractive indexes for both beams in the $2\mathbf{k}_a-\mathbf{k}_b$ process as

$$\begin{aligned}
n_a &= 1 + \frac{N\mu_{21}^2}{2\hbar\varepsilon_0}\frac{\mathrm{Re}(\sigma_{21})}{\Omega_a}; \\
n_b &= 1 + \frac{N\mu_{23}^2}{2\hbar\varepsilon_0}\frac{\mathrm{Re}(\sigma_{23})}{\Omega_b}.
\end{aligned} \tag{110}$$

The refractive index as a function of the detuning of the E_a field is plotted in Fig. 32(a) for a stationary atom. The numerical parameters to plot these curves, and

Figure 32 – (a) refractive index for both input fields; (b) Phase-matching conditions for both FWM signals. All curves are in function of the detuning of the a field.

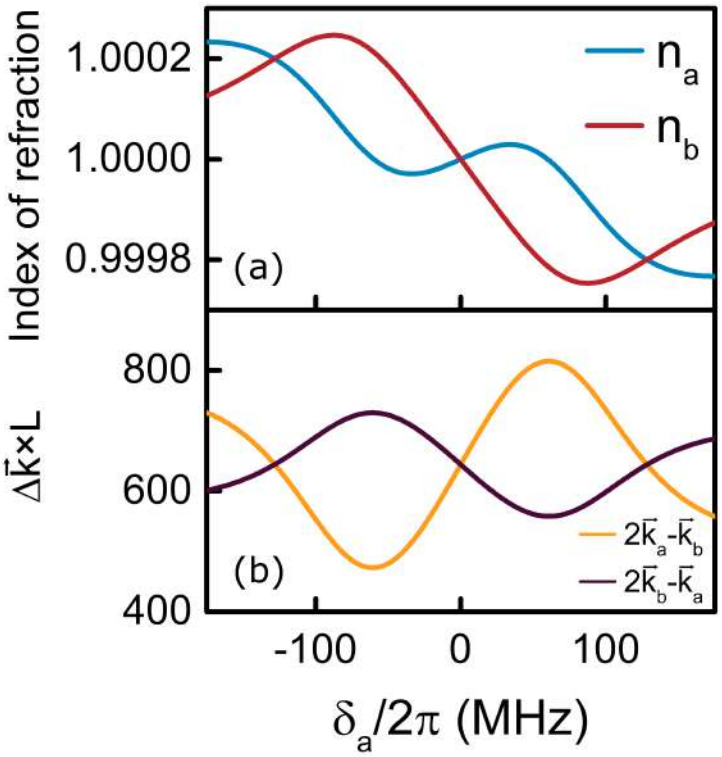

Source: Ref. [101].

the ones that follow, come from Ref. [46]. Only the coherence decay rate between the ground states γ_{13} is not available in this reference and it was assumed to be much smaller than the other decay rates of the system. Notice that n_b exhibits the expected behavior of increasing with frequency, with an anomalous dispersion window around the resonance. The interesting thing is that n_b is the refractive index of the field with a fixed frequency, meaning that this is a manifestation of the interaction of the beams, intermediated by the atomic medium. On the other hand, n_a does not display a typical behavior: in its anomalous dispersion window, there is a small interval in which the refractive index changes to a positive slope. We believe this small inversion is crucial to building up the correct phase-matching curve that modulates the FWM fields. This is a feature seen in the EIA process [104], which is observed in the transmission of the input beams. We could only obtain these refractive index curves by solving the Bloch equations in all orders, allowing for high-intensity coherent effects to play a role in the model.

For these curves of the refractive index, the resulting phase-matching conditions

Figure 33 – Theoretical FWM signals with velocity integration and propagation with phase-matching from Eq. 109 (solid line) and with $\Delta k = 0$ (dashed line). All curves are in function of the detuning of the a field.

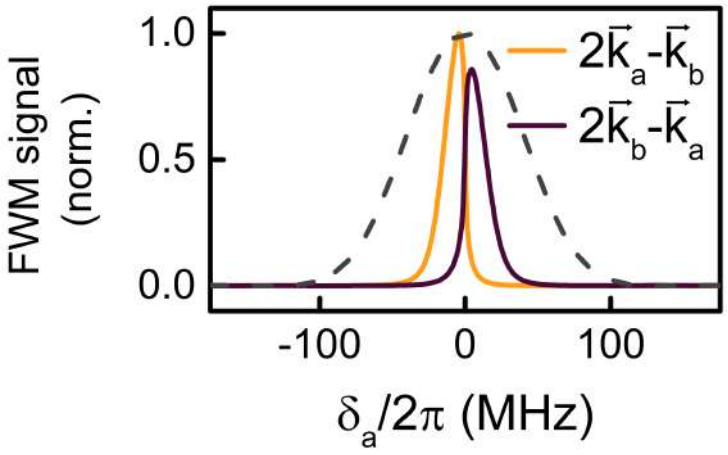

Source: Ref. [101].

for both FWM signals are in Fig. 32(b), again for an atom with no velocity. Notice that the Δk for the $2\mathbf{k}_a - \mathbf{k}_b$ signal is much closer to zero below the resonance and therefore the FWM signal itself should appear on the same region of the spectrum, as presented in the solid curves of Fig. 33. The same argument applies to the other signal, $2\mathbf{k}_b - \mathbf{k}_a$, as its phase-matching curve is closer to zero above resonance. If one considers $\Delta k = 0$, i.e. no phase mismatch, the result is shown in the dashed curve of Fig. 33. In this case, both FWM spectra are overlapping, broad, and identical.

The modeling of the refractive index is crucial for reproducing the features of the experimental signal. If this refractive index behaves as it usually does in a resonant interaction with an atomic medium, i.e. it generally increases with frequency but it has an anomalous dispersion window around the resonance, then the FWM signal $2\mathbf{k}_a - \mathbf{k}_b$ would only exist above resonance since the resulting phase-matching curve would only come closer to zero for $\delta > 0$. This is in disagreement with the spectra of the experiment. See for example the results of Fig. 28, in which the signal $2\mathbf{k}_a - \mathbf{k}_b$ is below resonance. Moreover, if we choose to neglect any dispersion effects, a phase mismatch due exclusively to the angle could be obtained, but only for a very large detuning (of hundreds of MHz). Therefore, angle alone does not provide the proper Δk that can be compensated by only adjusting the laser detuning. This could be the case if the ground states were not degenerate and therefore, lasers E_a and E_b had different wave numbers, as the authors of Ref. [29] demonstrate.

The high temperature of the vapor causes a significant Doppler broadening, which must be taken into account when calculating the FWM spectra. To obtain the spectra shown in Fig. 33, we used the Maxwell-Boltzmann velocity distribution to integrate Eq. 108, similarly to the previous section. The atomic density in these curves is approximately 10^{12} cm^{-3}, and the intensity of both input fields is ten times the saturation intensity of the transition. These values of intensity and atomic density are consistent with the range of experimental parameters. However, it should be noted that the model does not fit the experimental data perfectly, particularly when these parameters are modified. It is possible to modify the intensity, for example, in the experiment to obtain FWM results for a wide range of values while the theoretical results are not as robust.

Our model suggests that the nonlinear interaction between the fields in the medium leads to two fundamental responses: (i) a window with two dispersive curves in the behavior of the refractive index of the scanning laser, similar to what is seen in the EIA process; (ii) a variable refractive index for the laser with a fixed frequency. These two effects work together to create the necessary phase-matching condition to generate a signal below resonance and another above.

The results described in this section were published in a regular article in the Journal of Physics B [101]:

A. S. Alvarez, A. A. C. de Almeida, and S. S. Vianna, ‘‘Two symmetric four-wave mixing signals generated in a medium with anomalous refractive index”, J. Phys. B: At. Mol. Opt. Phys. 54 045403 (2021).

5 DEGENERATE FOUR-WAVE MIXING WITH COLD ATOMS: INTENSITY CORRELATIONS

In the previous section, we modeled results that were connected to the inhomogeneously broadening of the atomic medium. The goal from now on is to continue exploring the same experimental setup but switch the sample to cold rubidium atoms in a magneto-optical trap (MOT). In this context, without the Doppler-broadening, we present a study of the correlation between field intensity fluctuations of the two independent four-wave mixing (FWM) signals and between the transmission signals as well.

There are different approaches to address the issues related to these fluctuations, including both frequency domain and time domain analyses. In the latter approach, the group led by M. O. Scully has produced a set of articles [107, 108, 40] that are relevant to the problem we present here. Our experiment employs a similar setup using a single continuous-wave laser. However, in addition to examining correlations between transmitted beams, we also investigate correlations between two nonlinear signals generated by the FWM process of the previous section.

In this section, we present a set of experimental observations of strong correlations between the intensity fluctuations of two FWM signals generated through the interaction of laser light with a cold rubidium sample. We examine the correlation between the input laser fields, and our observations are consistent with previous findings in the literature. We also compare different polarization configurations, which allow us to access distinct internal energy level structures. Since we use a cold atomic sample with a narrow Maxwell-Boltzmann distribution, we can study how the correlations behave as a function of laser detuning. This is an advantage of the cold system compared to an atomic vapor, in which multiple velocity groups can respond to the input laser over a range of detunings determined by the Doppler broadening.

Additionally, we observe an oscillatory behavior consistent with Rabi oscillations [39] in the correlation functions. This behavior is detectable long after the transient period, and we can retrieve the frequency information through the correlation function. This concept of extracting an oscillation frequency using the correlation function has

been used in other contexts such as the observation of quantum beats in spontaneous emission or the detection of temporal beats in Raman Stokes fields [109]. Our theoretical model supports the idea that it is only due to fluctuations that we can detect this oscillatory behavior of the system.

Finally, the spectra of each of the polarization configurations are significantly different due to the distinct level structures. If the input lasers have linear and orthogonal polarization, the situation is the same as it was in the previous section, i.e. the system might be modeled with a three-level system. However, if the polarization of the input beams is circular and parallel then the population is pumped to the extreme Zeeman sublevels restricting the FWM to a pure two-level system. These differences remain throughout all spectra, so we draft a theoretical model by the end of the section. Although we do not consider our results satisfactory, we find them sufficient to identify the phenomena responsible for these differences.

5.1 Magneto-Optical Trap

Since the experiment described in this section is performed within a sample of cold rubidium atoms trapped in a MOT, it is useful to first provide some details about this device.

A magneto-optical trap is a device used to capture and manipulate atoms or molecules using a combination of lasers and magnetic fields. The MOT was first demonstrated by the late 1980s, and eventually rendered the Nobel prize to Steven Chu, Claude Cohen-Tannoudji, and William D. Phillips [42], and has since become an important tool in the fields of atomic physics, molecular physics, and quantum optics. The basic principle behind a MOT is to use laser light to cool and trap atoms or molecules in a three-dimensional trap formed by the forces that arise from the interaction of the laser light and the magnetic field with the atoms.

One of the main advantages of a MOT is that it allows for the precise control and manipulation of atoms or molecules over a wide range of conditions. This makes it an ideal tool for studying the properties of these systems and for developing new technologies based on these properties. Some of the applications include: compact

atomic clocks [110], as a MOT can be used to create a highly stable and accurate atomic clock by trapping a large number of atoms and measuring the frequencies of their transitions between energy levels; the study of cold collisions [111, 112], since the extremely low temperature highly suppresses the interactions between particles, which can provide insight into the underlying physics of these systems, and can be used to develop new technologies based on these interactions.

Let us describe briefly the physics behind the MOT. Light carries linear momentum, meaning that when a photon interacts with a moving atom there might be a momentum transference if the atom absorbs the photon. The force exerted in this phenomenon is the radiation force [44]

$$F = \frac{\sigma_{abs} I}{c}, \tag{111}$$

where σ_{abs} is the peak absorption cross-section of the atom, *I* is the laser intensity and c is the light velocity in vacuum. Usually, for the resonance frequency, this peak absorption cross-section is much larger than the actual size of the atom, making the radiation force quite significant.

Even though this description of the force does not need to consider a quantized light, it is insightful to look at the problem in such a way. Each photon absorbed by the atoms must be re-emitted by spontaneous emission in a random direction. Hence, the whole process can be seen as a scattering of photons. The force in this case is given by the multiplication of the photon momentum $\hbar k$ and the scattering rate. If we consider a two-level atom as a model, then this force is [44]

$$F_{scatt} = \hbar k \frac{\Gamma}{2} \frac{I/I_{sat}}{1 + I/I_{sat} + 4\delta^2/\Gamma^2}, \tag{112}$$

where Γ is the decay rate of the excited state, I_{sat} is the saturation intensity, and δ is the detuning from resonance. For a moving atom, we might already take into account the Doppler effect, i.e. $\delta = \omega - \omega_0 + kv$, where ω is the laser frequency, ω_0 is the resonance frequency, k is the wavevector, and v is the atomic velocity.

From Eq. 112 one derives the optical molasses technique developed by Chu *et al* in 1985 [113]. Still with the simple model of a two-level atom, consider the interaction with a pair of counter-propagating lasers, as presented in Fig. 34.

Figure 34 – Optical molasses technique: counter-propagating lasers acting on a moving two-level atom.

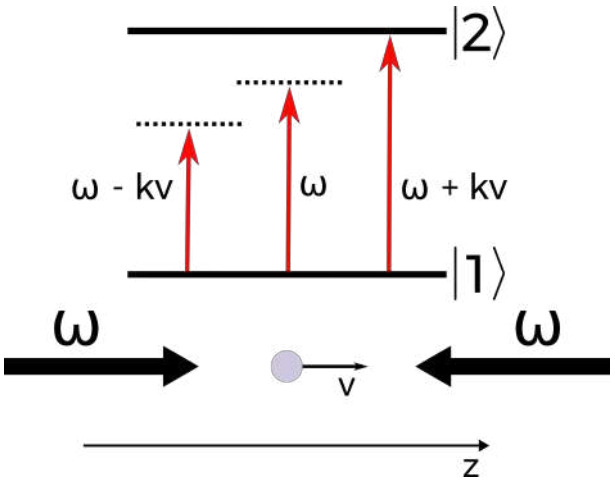

Source: The author (2023).

Since the atoms are moving in the direction of propagation of light, there will be a shift in the frequency of the lasers as seen by the atoms, caused by the Doppler effect. It is then possible to choose the correct detuning to make one of the lasers resonant with a set of velocity groups, leading to an absorption. Only these atoms will be slowed. Let us try to see the behavior of the combined forces in this situation. The net force on the atom is

$$F_{molasse} = F_{scatt}(\omega - \omega_0 - kv) - F_{scatt}(\omega - \omega_0 + kv), \tag{113}$$

and if we make an expansion of the force to consider only low velocities, i.e. $kv < \Gamma$ we get

$$\begin{aligned} F_{molasses} &\approx F_{scatt}(\omega - \omega_0) - kv\frac{\partial F}{\partial \omega} - \left[F_{scatt}(\omega - \omega_0) + kv\frac{\partial F}{\partial \omega}\right], \\ &\approx -2kv\frac{\partial F}{\partial \omega}, \\ &\approx -\alpha v, \end{aligned} \tag{114}$$

where $\alpha = 2k\frac{\partial F}{\partial \omega}$. This is a force similar to the one a particle experiences when it moves through a viscous fluid, therefore the name of the technique: optical molasses. In the actual experiment, it is important to use pairs of counter-propagating beams in all three directions to effectively slow down the atoms.

This is a very successful technique for cooling neutral atoms. Consider alkali metals as an example: the lowest temperature achievable is of hundreds of μK [114], which is an outstanding result. This lower limit is imposed by the spontaneous emission

of the atoms, i.e., once a photon of the cooling beam is absorbed, the atom must re-emit this photon in a random direction. To preserve momentum conservation, the atom must move in the opposite direction with a certain recoil velocity. By associating a temperature with this velocity, we may find the recoil cooling limit, which is the lowest temperature we can achieve through the optical molasses technique.

In this technique, although the atoms may accumulate in the region of the intersection of the beams, because of their small velocities, they are not trapped. Eventually, the atoms leave the interaction region and regain speed. To trap them, we must use a specific type of polarization in the beams combined with a magnetic field gradient, as first suggested by Jean Dalibard [115].

In this scheme, called magneto-optical trap, we add to the experimental setup of the optical molasses a pair of coils in the anti-Helmholtz configuration, i.e. their currents have different directions. This pair of coils generates a uniform field gradient near the point in the middle of them. This means that the atoms will experience a Zeeman shift in their energy levels. This shift can be explored, along with the selection rules, to add a new term in the force of Eq. 114.

Let us look in detail at how this field gradient and the lasers act together. For that, consider a simple transition $|F=0\rangle \rightarrow |F'=1\rangle$ as shown in Fig. 35. The pair of counter-propagating beams have orthogonal and circular polarizations, so they will only interact with the set of velocity groups that have the correct position regarding the center of the trap. This is caused by the selection rule of angular momentum. A σ^+ beam may only cause transitions that increase the angular momentum by one unity, while a σ^- polarization causes only transitions that decrease the angular momentum.

We might rewrite Eq. 113 if we consider the Zeeman effect in the detuning of the lasers, i.e. $\delta = \omega + kv - (\omega_0 - \beta z)$. The Zeeman shift is given by βz, where β depends on $\frac{dB}{dz}$. By doing the same previous expansion, we arrive at:

$$F_{MOT} \approx -\alpha v - \frac{\alpha\beta}{k} z. \tag{115}$$

There is a new term, a restoring force, meaning that the dynamics of the atoms in the trap follows a harmonic motion, typically over-damped [44]. A simplified representation of the apparatus to trap the atoms is presented in Fig. 36.

Figure 35 – Magneto-optical trap: counter-propagating lasers with circular polarization acting on a moving atom through a magnetic field gradient.

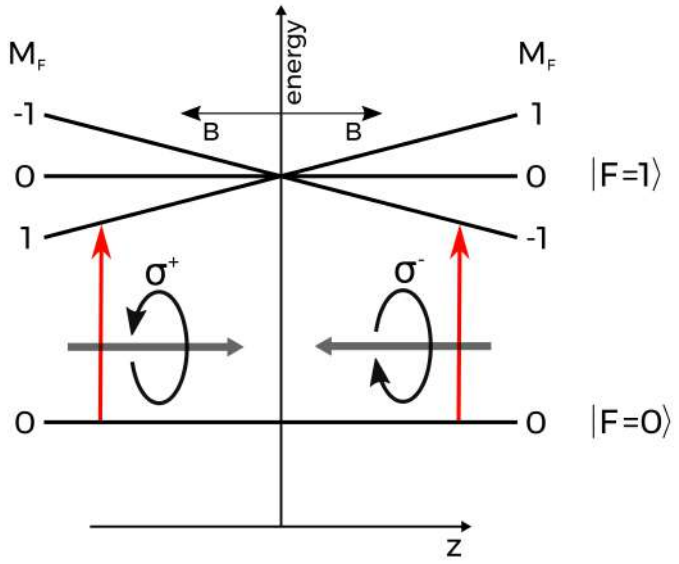

Source: The author (2023).

Figure 36 – Magneto-optical trap scheme.

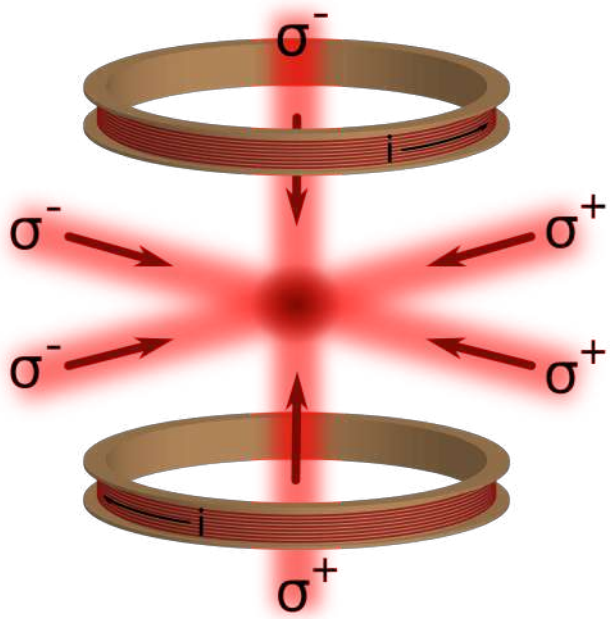

Source: The author (2023).

Magneto-optical traps provide good sources of cold atoms for a wide range of experiments. It is an easy-to-load trap, with typical capture velocities of tens of *m/s* [116], and up to 10^{10} trapped atoms. Surely, these numbers may change significantly from one specific setup to another. We must also emphasize that this is not a magnetic trap. The field gradient in a MOT is much smaller than in pure magnetic traps (not even enough to hold the atoms against gravity) so the forces in play are effectively due to the lasers.

From a practical point of view, the cooled atoms must stay in a very low-pressure environment to avoid collisions with background atoms and consequently the escape from the trap. This implies that the experiment requires a good vacuum system. For the MOT, the often used type of pump is an ionic pump, in our case, a *Starcell* from Varian. This pump operates typically in an ultra-high vacuum regime, i.e. $\sim 10^{-9}$ Torr. It ionizes the gas inside the chamber and accelerates these ions with a high electric potential, ranging from 3 kV to 7 kV. One of the main reasons for using ionic pumps in cold atoms experiments is that it does not have moving parts or the need for oil. Thus, they require little maintenance and produce almost no noise.

The vacuum pump is connected to a glass chamber, henceforth labeled *science chamber*, where the lasers can interact with the atoms. It is also in the science chamber that lies the rubidium dispenser. This dispenser contains a mixture of a rubidium compound and a reducing agent [117]. The alkali metal is released in a controllable way via ohmic heating, with currents typically from 5 A to 7 A and reaching temperatures up to ~800 °C.

Regarding the magnetic field, we use a pair of circular coils with a radius of 27 mm and made of 1.1 mm diameter copper wire, with 50 turns. As mentioned before, the coils are in an anti-Helmholtz configuration with a 1.5 A current, i.e. the currents circulate in different directions. The final arrangement is similar to the one presented in Fig. 36, with a typical magnetic field gradient of 10 G/m inside the science chamber.

In addition to this magnetic field, there are also compensation coils that balance external fields, especially the Earth's magnetic field. The cage is made of three pairs of square coils, arranged to form a cube so that each pair can generate a field in a

Figure 37 – Level diagram of the D_2 line of ^{87}Rb with the cooling and repump transitions in red and blue, respectively.

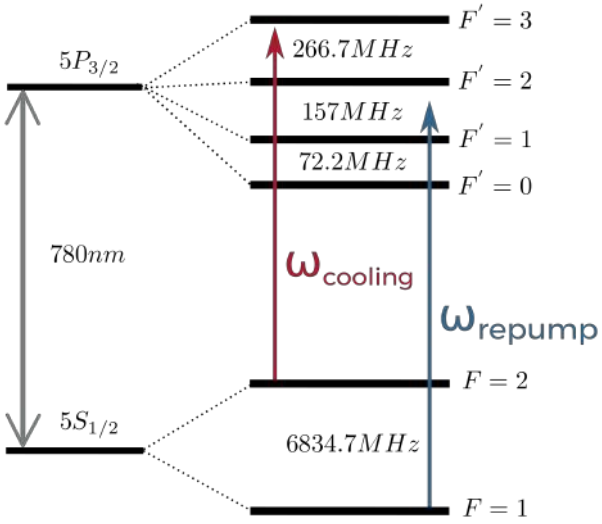

Source: The author (2023).

specific direction. The sum of these vectors can act against the earth's magnetic field and cancel it. For our system, we coarsely tuned the currents in the cage, but a precise procedure can be used as shown in Ref. [118].

In the optical setup of the experiment, we use two diode lasers of the same type as in the previous sections (*Sanyo* DL7140-201S). An extra step that we perform in this setup compared to what we presented so far, is to use a homemade locking frequency system to prevent the lasers to drift away from a desired frequency position. This system uses the peaks from a saturated absorption spectroscopy (SAS) signal as a reference to correct the frequency of the laser. The key feature of it is that it takes the time control pulses of the experiment (which we detail further along) to correct the laser frequency only when a measurement is not being made. Typical frequency locking devices involve introducing a periodic pertubation into the laser reference signal. Our system assures that the locking device does not disturb any acquired data. It is used not only to lock the frequency of the MOT lasers but also for the laser that induces the FWM process of this section.

The two diode lasers used in the MOT are labeled "cooling"and "repump"(see Fig. 37). The cooling laser is primarily responsible for the MOT mechanism, transferring momentum to the atoms through absorption. It is tuned near the transition $|F = 2\rangle \rightarrow |F' = 3\rangle$ of ^{87}Rb. Although this transition is closed, meaning it can only relax back to its

ground state, some atoms may still be able to reach the state $|F' = 2\rangle$. These atoms may then fall into the state $|F = 1\rangle$, which is a dark state where they can no longer interact with the cooling laser. To address this issue, the repump laser is tuned to the open transition $|F = 1\rangle \rightarrow |F' = 2\rangle$.

During the operation of the MOT, we use the SAS signal to monitor the frequencies of both the cooling and repump lasers. In order to properly trap the atoms, the cooling laser is set to a frequency that is near the crossover between the states $|F' = 1\rangle$ and $|F' = 3\rangle$. An acoustic-optical modulator (AOM) is used to bring the frequency of the laser closer to the closed transition, but it is still slightly detuned from the state $|F' = 3\rangle$. This is important because it allows the laser to interact with a larger number of atoms. If the laser frequency is set to be completely in resonance, only the stationary group of atoms will be able to interact with it.

We use the AOM for two reasons: first, the AOM modulates the cooling laser in order to switch the MOT in a controlled temporal scheme; second, the cooling laser must have a small detuning to optimally cool the atoms. In this case, the chosen crossover transition to fix the laser frequency is 212 MHz below the $|F' = 3\rangle$ level. The AOM blue shifts the laser frequency by 200 MHz for the first order, leaving it only 12 MHz from the cyclic transition. We also use the zero order of the AOM, in other parts of the experiment, e.g. as a guide beam for alignments or to measure the optical density of the MOT.

Since there are many optical elements in the path of the cooling beam before arriving at the atoms, significant power is lost. Our diode lasers have typical powers of tens of mW, making necessary the use of an amplifier to compensate for the losses. We use a *Boosta* amplifier from *Toptica Photonics*. In an optimal alignment situation, an input power of 20 mW renders an output power of 700 mW, which is enough for all of the MOT beams.

The MOT can be observed using an IR camera because of the spontaneously emitted light produced by the trapping process. It is also possible to capture an image of the trapped atoms using a CCD (charge-coupled device) camera, which can be used to measure the diameter of the cloud, as shown in Fig. 38, by converting the image into a matrix that contains the information for each pixel. The data from the sum of the rows

Figure 38 – CCD image of the atomic cloud. The red line indicates the diameter taken from the Gaussian fit.

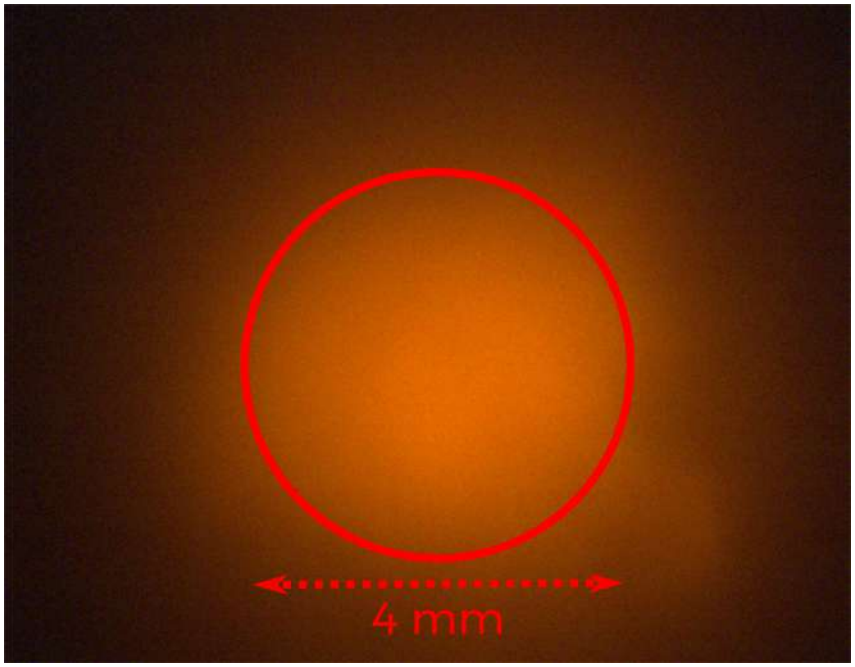

Source: The author (2023).

or the sum of the columns can then be plotted and fit with a Gaussian curve. The waist of this curve is used as the diameter of the MOT and in our case, the cloud measures 4 mm.

The same fluorescence that allows the CCD to capture images of the cloud might be used to measure the number of atoms. In this case, we use a photodetector (DET36 from *Thorlabs*) that captures this fluorescence with the aid of a lens. Using the peak response of the photodetector we may calculate the total power detected at that solid angle. By generalizing to a sphere, we know the total power emitted by the atoms. Finally, we divide this total power by the energy of a single photon and the scattering rate, finding the number of atoms. For our experimental setup, this number typically has the order of 10^9 atoms. The MOT diameter and number of atoms are a fraction of the several parameters that can be obtained from characterization measurements [119].

5.2 Experimental setup and results

The experimental configuration is similar to the one in the previous section. However, a key difference is that now we use a single cw laser instead of two. This means that the two input fields that induce the FWM process come from the same laser.

Figure 39 – Simplified scheme of the four-wave mixing setup. PBS and APD are polarizing beam-splitter and avalanche photodiode, respectively.

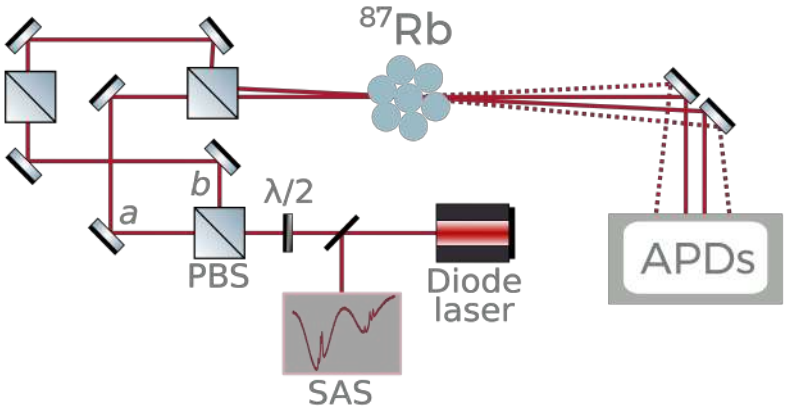

Source: The author (2023).

As the initial goal is to investigate the connection between resonant conversion of phase fluctuation into intensity fluctuations and the FWM process, it is interesting to use this single pump setup, as it eliminates the need of locking the phase of one input field to the other one. That is, both input fields necessarily have the same phase fluctuations since they come from the same laser.

We present the experimental setup in Fig. 39, in which the two input laser beams are labeled by their wave-vectors $\mathbf{k}_a$ and $\mathbf{k}_b$. As mentioned previously, the cw laser is similar to the cooling and repump lasers of the MOT and therefore can be locked in frequency and then modulated with an AOM. These two beams interact with our sample of cold ^{87}Rb atoms in the MOT.

We explore two cases regarding the polarization of the input laser fields. In the configuration depicted in Fig. 39, the polarizations are linear and orthogonal. In this case the fields are aligned in the atomic cloud using a PBS. In the second case, with circular and parallel polarizations, we substitute the first and last PBS for beam-splitters and add two quarter-wave plates before and after the atomic cloud.

As in the previous experiment with the atomic vapor, we are mainly interested in the two similar FWM signals. For this end we set the input beam powers to be almost the same so that the system generates the two signals shown in Fig. 40. The input beams are in an almost copropagating configuration, with a small angle of 10 mrad between

Figure 40 – Spatial distribution of the input beams and FWM signals.

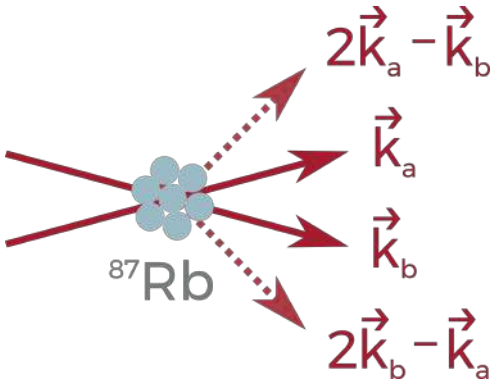

Source: The author (2023).

them to allow for the spatial separation of all four signals. This type of forward geometry is challenging since scattered light from one beam might arrive at the detection position of the other beams. To prevent this, we couple each signal in optical fibers, which results in cleaner detections.

The two FWM signals and the transmissions of the input beams *a* and *b* are detected by avalanche photodiodes (APD) of the models APD120A/M (max responsivity at 800 nm) and APD120A2/M (max responsivity at 600 nm) from *Thorlabs*, respectively. We use these detectors because they are highly sensitive and, for our experimental situation, the FWM light can be fairly small. To achieve this great sensitivity, APDs provide gain in the input signal via the process of avalanche multiplication.

The beams that induce the degenerate FWM processes are tuned near the closed transition $|F = 2\rangle \rightarrow |F' = 3\rangle$, of the D_2 line of ^{87}Rb. Since this is the same transition of the cooling laser of the MOT, there could be a competition between the lasers, making the FWM process inefficient. To avoid this, we use a temporal scheme to generate and acquire the signal of interest with the MOT lasers off. In our case, we built a time control apparatus using an *Arduino* board that temporally manages the entire experiment. Fig. 41 shows a scheme of this temporal control.

All trapping fields, i.e. cooling laser and anti-Helmholtz (AH) coil, are shut down in a 2 ms window. This time is small enough so that the atoms cannot gain much speed and therefore move away from the center of the science chamber. It is in this window that we obtain the whole FWM signal. The trigger (red curve in Fig. 41) has a small delay of

Figure 41 – Temporal control of the FWM experiment.

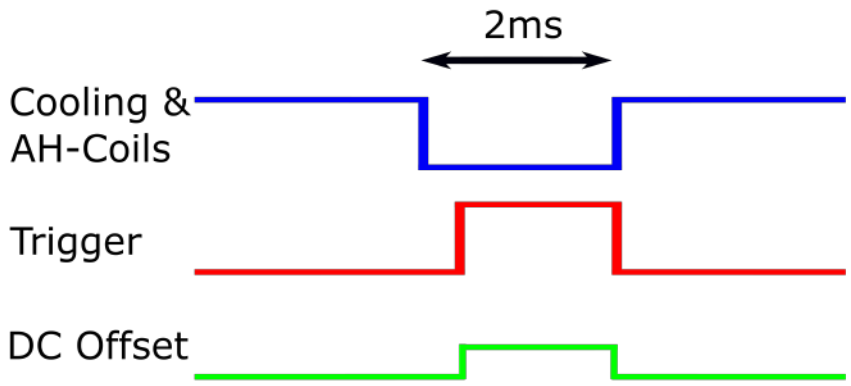

Source: The author (2023).

hundreds of μs, allowing the repump laser to properly prepare the atoms in the ground state $|F = 2\rangle$, where they can interact with the FWM laser. In fact, the repump laser is always active throughout the measurement. This trigger controls a signal generator that generates a DC Offset (green curve in Fig. 41) to control the AOM. The same trigger that turns the MOT on and off controls the frequency locking circuit. This way, the circuit only corrects the frequency of the laser while the MOT is on and therefore no data is being acquired. If, on the other hand, we want to scan the frequency of the input lasers to generate a spectrum, we switch the DC offset in the signal generator to a ramp and connect it directly to the laser to modulate the injection current, scanning the frequency of beams *a* and *b*. We detail more of these spectra measurements by the end of the section.

In the time interval in which the MOT fields are off, we acquire data from a time series with typically 100 μs intervals of all four signals. In these measurements, one must be careful with the detuning to the resonance because, for small detunings, or high laser intensities, the radiation pressure can disperse the atomic cloud. Therefore, there is a practical limitation in our experiment, since the FWM signal increases when the input laser is closer to resonance and for higher laser intensities, the same regime increases the radiation pressure.

Because of this limitation, the experimental setup with linear and orthogonal polarizations has an advantage: its spectrum (see Fig. 42(a)) is wider than the spectrum for the circular and parallel case (see Fig 42(b)). Furthermore, it has a dip around the resonance so that the maximum signal is slightly off-resonance. The fundamental

Figure 42 – FWM spectra with input laser intensity $I_a = I_b = 10$ mW/cm^2 for (a) linear and orthogonal polarizations; (b) circular and parallel polarizations.

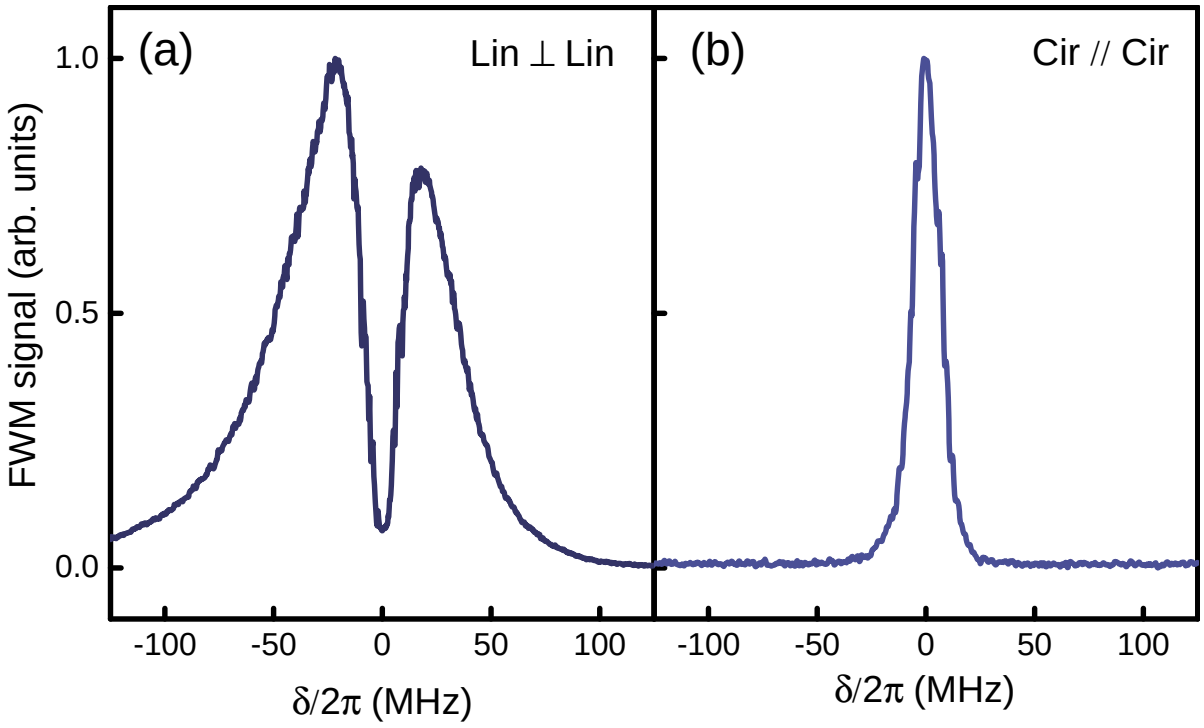

Source: The author (2023).

difference between these cases is in the energy level structure behind each setup. That is, while the circular case is modeled by a pure two-level system, the linear case has to be modeled as we discussed in the previous section, with at least a three-level system. We believe this dip is due to the presence of two degenerate ground levels together with the equally powerful input laser beams which we scan their frequencies simultaneously, inducing a coherent population trapping that prevents the signal from being generated on resonance [54, 120, 121]. We detail this hypothesis by the end of the section. The important point, for now, is that the measurements with linear and orthogonal polarizations are easier to obtain and render better results in terms of signal-to-noise ratio.

The signal we are interested in now is the time series of the intensity fluctuations of all four signals and the two polarizations. The acquired data typically has 100 μs and is filtered with a high-pass ideal FFT filter with a cutoff frequency of 500 kHz, to eliminate any slow fluctuations of the signals. Let us begin the analysis by looking at the intensity fluctuations if there are no atoms to interact with the laser. Naturally, in

Figure 43 – Time series of the intensity fluctuations for the transmittance of the input lasers with $I_a = I_b = 0.15$ mW/cm^2, MOT off, and (a) circular and parallel polarizations; (b) linear and orthogonal polarizations.

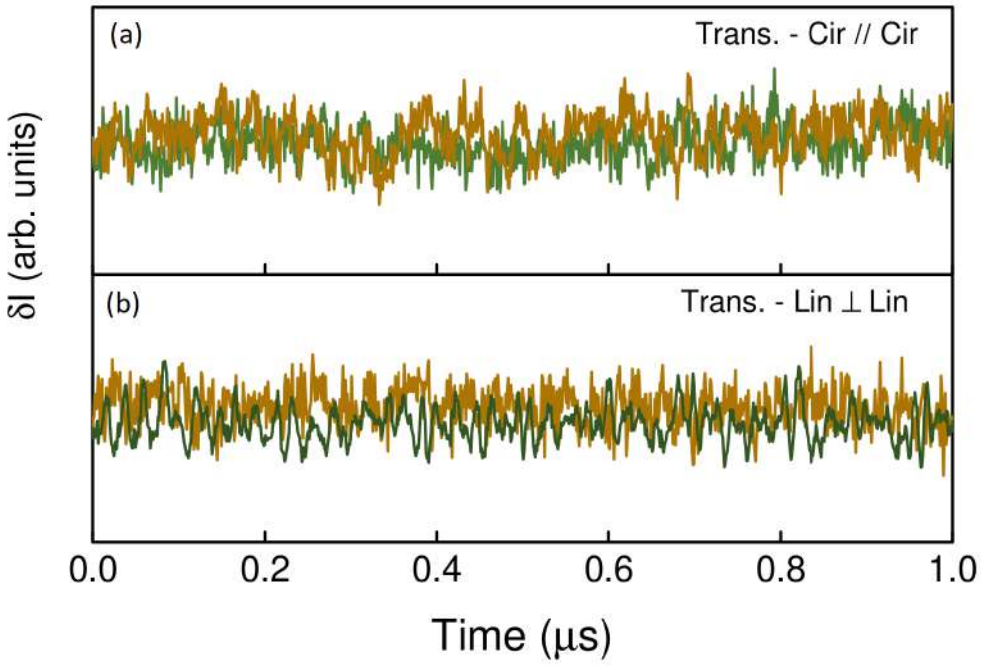

Source: The author (2023).

this case, we can only study the transmission signals, as there cannot be an FWM signal without the atomic media. We present a 1 μs section of these time series in Fig. 43. Notice that there are fluctuations in both fields but they are not at all similar. This indicates that, without the atomic media to interact, the lasers present no correlation [40].

The intensity fluctuations of the four signals and their two polarizations are shown in Fig 44. In both Fig. 44(a) (circular and parallel polarization) and Fig. 44(b) (orthogonal and linear polarization), we plot the intensity fluctuations over time for FWM signals (red and blue lines) with input laser intensities of $I_a = I_b = 3.3$ mW/cm^2 and a detuning from the excited state of $\delta/2\pi = 70$ MHz. While the fluctuations show similar behavior, they are not identical. It can be challenging to obtain a high signal-to-noise ratio for a signal far from resonance or with input lasers close to or above the saturation intensity, due to experimental constraints related to radiation pressure.

On the other hand, the intensity fluctuations of the input lasers can be obtained at a laser frequency much closer to resonance as long as the intensity is small. In Figs. 44(c) and (d) we show the time series of the transmission signals (orange and green

Figure 44 – Time series of the intensity fluctuations for the FWM signal with input laser intensity of $I_a = I_b = 3.3$ mW/cm^2, detuning from the excited state of $\delta/2\pi = 70$ MHz and (a) circular and parallel polarizations; (b) linear and orthogonal polarizations. Time series of the intensity fluctuations for the transmittance of the input lasers with $I_a = I_b = 0.15$ mW/cm^2, $\delta/2\pi = 15$ MHz and (c) circular and parallel polarizations; (d) linear and orthogonal polarizations.

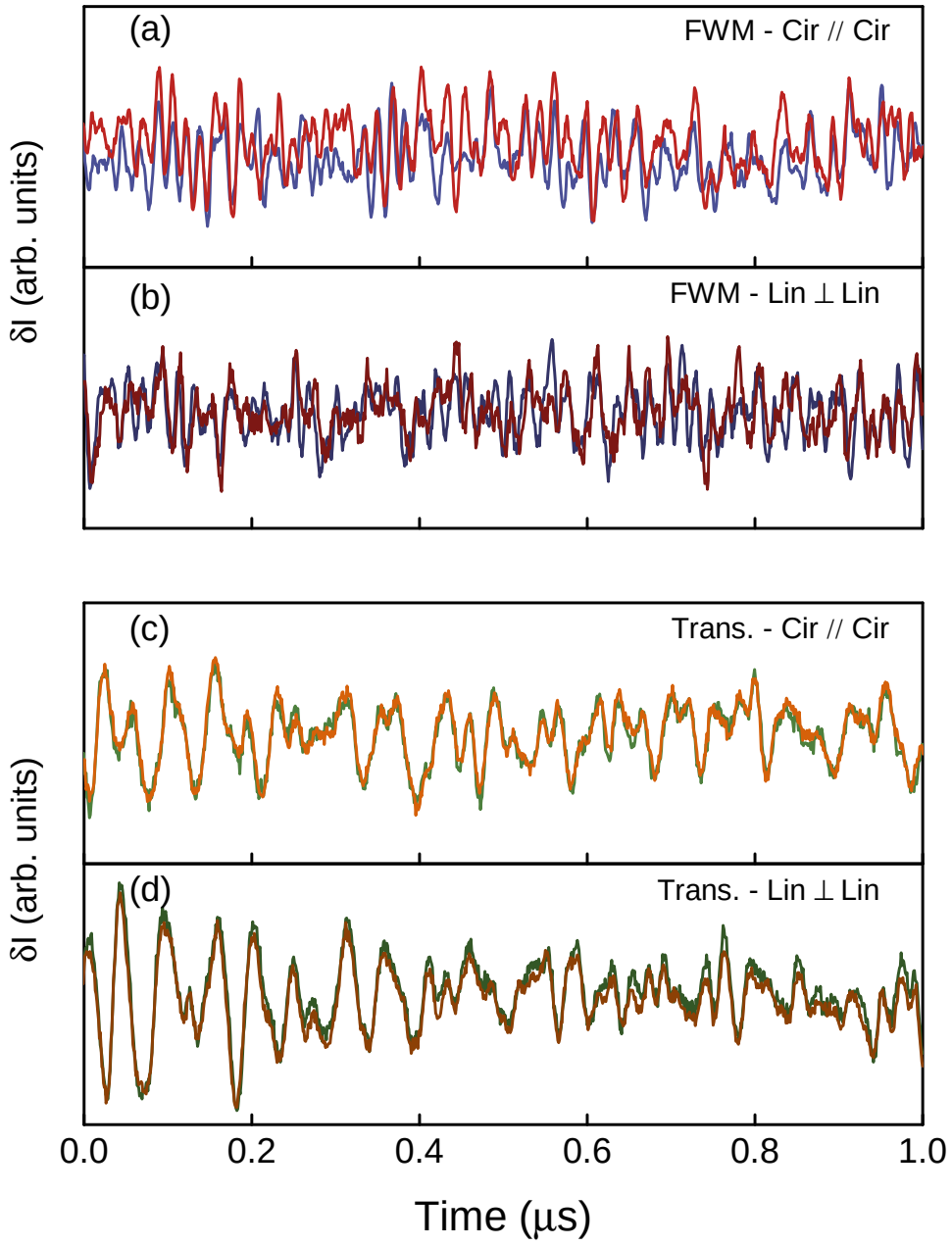

Source: The author (2023).

lines) for an input laser intensity of $I_a = I_b = 0.15$ mW/cm^2 and a detuning from the excited state of $\delta/2\pi = 15$ MHz. It is clear that these results are remarkably synchronized and should present near-perfect correlations, a known result [40].

These correlations can be quantified with the second-order correlation function $G_{ij}^{(2)}(\tau)$ [107, 108, 40, 38] for intensity fluctuations of two optical beams with time delay τ. It is given by

$$G_{ij}^{(2)}(\tau) = \frac{\left\langle \delta I_i(t)\, \delta I_j(t+\tau) \right\rangle}{\sqrt{\left\langle \delta I_i(t)^2 \right\rangle \left\langle \delta I_j(t+\tau)^2 \right\rangle}}, \tag{116}$$

where the $\delta I_{i,j}(t) = I_{i,j}(t) - \left\langle I_{i,j}(t) \right\rangle$ are the time-dependent intensity fluctuations, with $\left\langle I_{i,j}(t) \right\rangle$ being the average intensities of the laser fields and $i, j = a, b, s_1, s_2$ are the labels to designate the two input fields and the two FWM signals, respectively.

The second-order correlation function is a statistical measure that quantifies the degree of correlation between two random variables at different time lags. It is often used to analyze the temporal dynamics of a system and to identify patterns in time-series data. In terms of applications, it can be employed to analyze a wide range of phenomena, including the coherence of lasers and the correlations in noise signals. The definition we provide here is normalized so that the function is bounded in the range [-1,1], with the bottom value meaning anti-correlation and the top value meaning correlation.

In our case, we want to use this function to quantify the correlations between the data of Fig. 44. We present the intensity fluctuations correlation functions $G_{ij}^{(2)}(\tau)$ for the pairs of time series of Fig. 44 in Fig. 45. We implemented the calculation of the $G_{ij}^{(2)}(\tau)$ with a *Python* code (see appendix c). These correlation functions have peaks at zero time delay with amplitudes (Pearson coefficient) of ≈ 0.6 for the FWM signals and over 0.95 for the transmission signals. This confirms the expectation of Fig. 44 that there is a strong temporal positive correlation in the intensity fluctuations of the output signals. Moreover, in Figs. 45(c) and (d) we also present the autocorrelation (orange curve) for the intensity fluctuations of the a laser beam. These curves are remarkably similar to the cross-correlation (dark brown curves) of the two transmission signals, especially

Figure 45 – Second-order correlation function $G_{ij}^{(2)}(\tau)$ between the FWM signals with input laser intensity of $I_a = I_b = 3.3$ mW/cm^2, detuning from the excited state of $\delta/2\pi = 70$ MHz and (a) circular and parallel polarizations; (b) linear and orthogonal polarizations. Second-order correlation function $G_{ij}^{(2)}(\tau)$ for the transmittance of the input lasers (dark brown line) and autocorrelation (orange line) with $I_a = I_b = 0.15$ mW/cm^2, $\delta/2\pi = 15$ MHz and (c) circular and parallel polarizations; (d) linear and orthogonal polarizations.

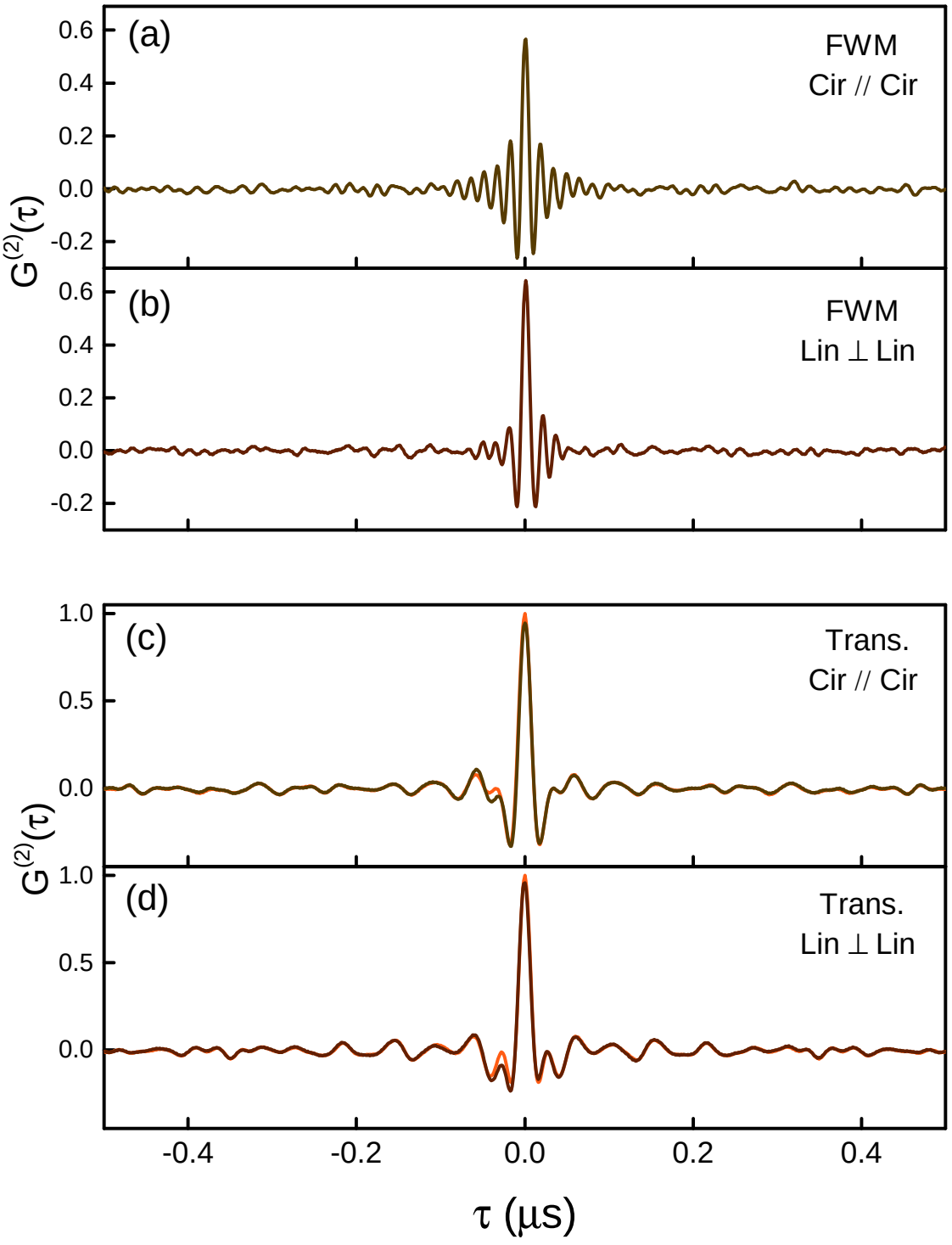

Source: The author (2023).

concerning the oscillations near zero delay.

The cross-correlation we see in the transmission beams arises from resonant phase-noise to amplitude-noise conversion [31, 122, 123, 124, 125], which is driven by the resonant interaction with atoms. If there were no atoms present or if the input laser was not near resonance, there would be no correlation. Essentially, the fields are correlated because they all come from the same laser with the same phase fluctuations. It would be interesting to examine the correlations between the transmited laser field and one of the FWM signals. Unfortunately, the experiment does not allow for this, as there is no suitable choice of parameters to obtain both signals simultaneously. To obtain the maximum FWM signal, the intensity of the input laser must be increased as much as possible without causing excessive radiation pressure on the atomic sample. On the other hand, to measure the intensity fluctuations of the input laser, the intensity must be kept low to prevent saturation of the medium and minimize the number of detected photons that do not interact with the atomic cloud.

A notable feature of these correlation curves is that the width of the FWM correlation peak appears different from the width of the transmission correlation peak, as expected due to the different intensities and detunings. In a similar experiment using an atomic vapor and a magnetic field to break the degeneracy of the Zeeman sublevels [107], the authors noted that the widths of the correlation peaks are related to the power broadening of the single photon resonance in the Rb vapor. To further investigate this, we repeated the time series for each pair at different intensities but with a fixed detuning, and plotted the normalized correlation functions in Fig. 46 for the FWM signals and transmission beams, respectively. We increased the input laser intensity by up to a factor of 3 in most cases, but the width of the correlation peak did not change significantly. This is likely because the atomic medium was not fully saturated in any of these measurements, either when we measured transmission or FWM signals. In the case of FWM signals, the input laser fields were above saturation intensity, but the nonlinear signal itself was weak due to the efficiency of the process.

We must then investigate the behavior of the correlation as a function of the detuning. Interestingly, the cold atomic systems are more suited to investigate this behavior than atomic vapors. In hot systems, the Doppler broadening is significant,

Figure 46 – Normalized second-order correlation function $G_{ij}^{(2)}(\tau)$ between intensity fluctuations of FWM signals varying input laser intensity at $\delta/2\pi = 85$ MHz with (a) linear and orthogonal polarizationa and (b) circular and parallel polarizations. Transmission signals varying input laser intensity at $\delta/2\pi = 25$ MHz with (c) linear and orthogonal polarizations and (d) circular and parallel polarizations .

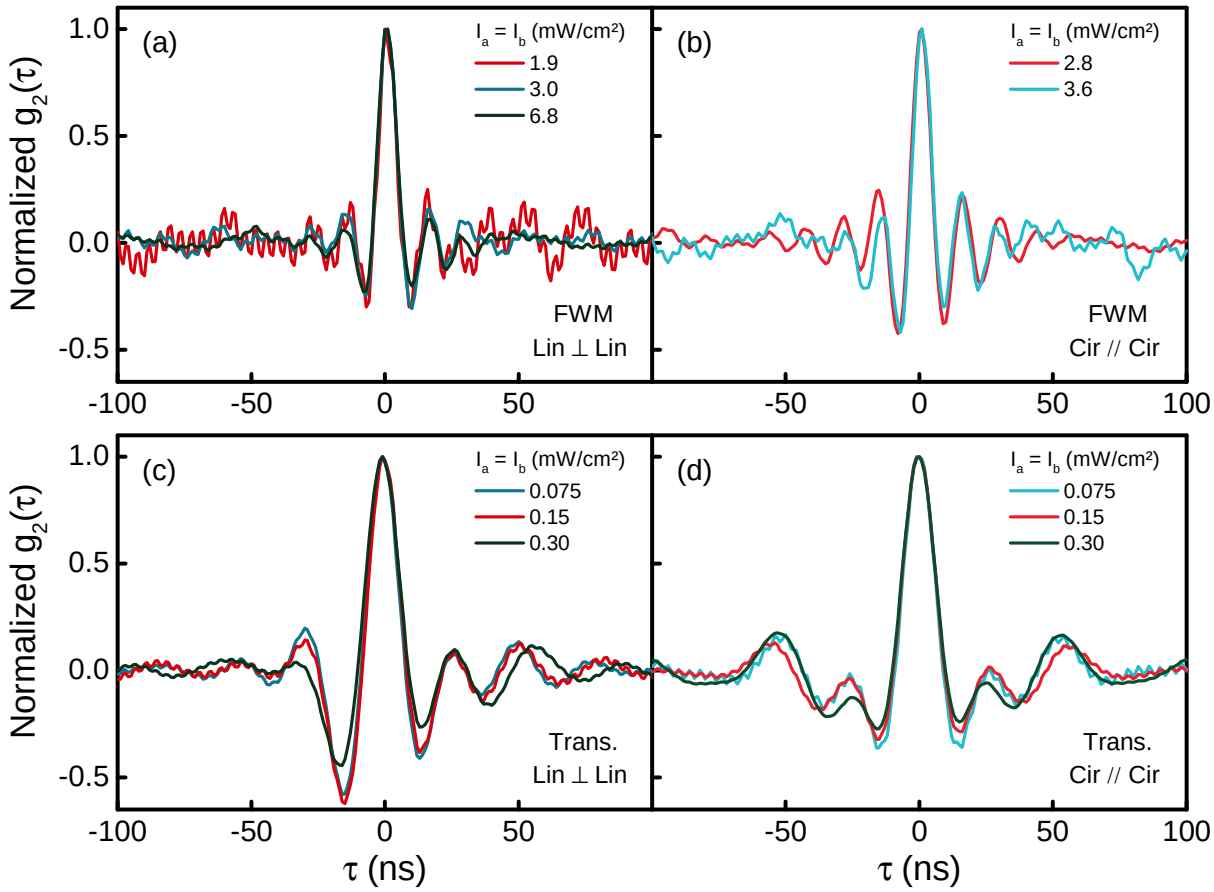

Source: The author (2023).

meaning that variations of the detuning inside the Maxwell-Boltzmann curve will always find a resonant velocity group and possibly cover any phenomena regarding detuning variations. We provide in Fig. 47 a detailed map of the correlation between transmission fluctuations as a function of detuning. We recall that in the case of the transmission analysis, we can work with very low intensities, so it is easy to tune the laser frequency without pushing away the atoms, allowing such a complete map. In this graph, the broadening of the central peak near resonance becomes clearer. Furthermore, it is noticeable the presence of oscillations near the central peak. It seems that the frequency of this oscillation gets smaller near resonance.

The same behavior described for the correlation between transmission signals can be seen in the correlations between FWM fluctuations. However, it is not possible to produce a detailed map as the intensity necessary to induce the FWM process

Figure 47 – Second-order correlation function $G_{ij}^{(2)}(\tau)$ as a function of the detuning $\delta/2\pi$ between transmission signals with (a) linear and orthogonal polarizations and (b) circular and parallel polarizations. The input laser intensity is $I_a = I_b =$0.15 mW/cm^2.

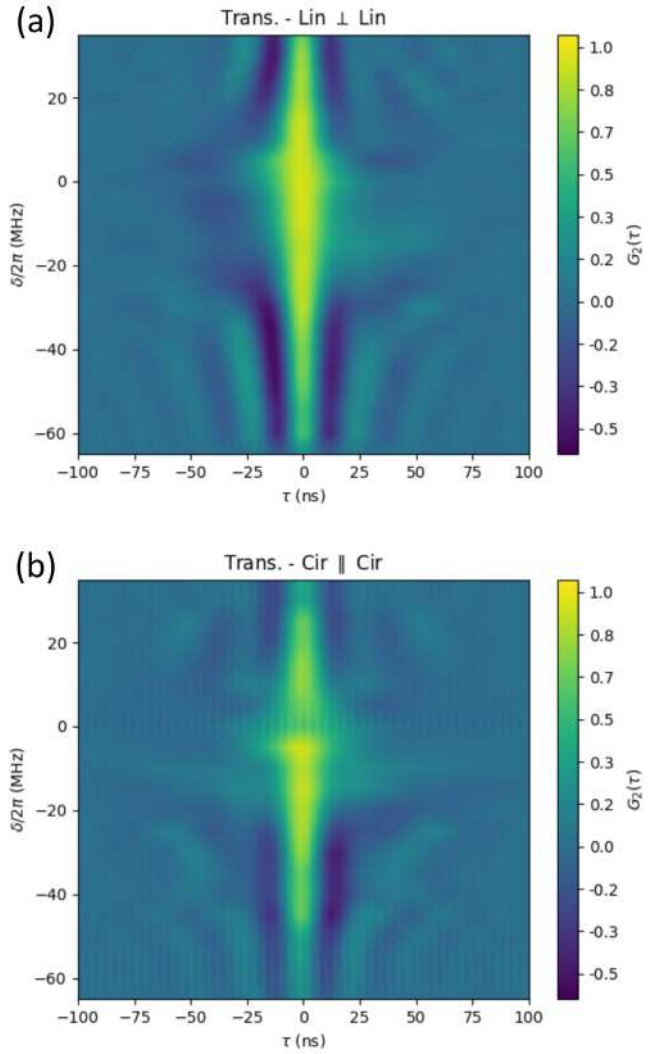

Source: The author (2023).

together with a small detuning will certainly exert a radiation pressure strong enough to push the atoms away. In this sense, we show in Fig. 48 the correlation curves between FWM signals for three different detunings. The most notable feature is that the correlation curves become wider as the frequency of the input laser approaches resonance. Additionally, far from resonance, an oscillation of the correlation curves becomes more evident and has a higher frequency. There are regions of correlation ($G_{ij}^{(2)}(\tau) > 0$) and regions of anti-correlation ($G_{ij}^{(2)}(\tau) < 0$). This behavior was also seen in the previous correlation curves for FWM signals (Figs. 45(a) and 45(b)), as they were all far from resonance. It is important to note that the results in Fig. 47 are for a fixed

Figure 48 – Second-order correlation function $G_{ij}^{(2)}(\tau)$ as a function of the detuning $\delta/2\pi$ between FWM signals with (a) linear and orthogonal polarization and (b) circular and parallel polarization.

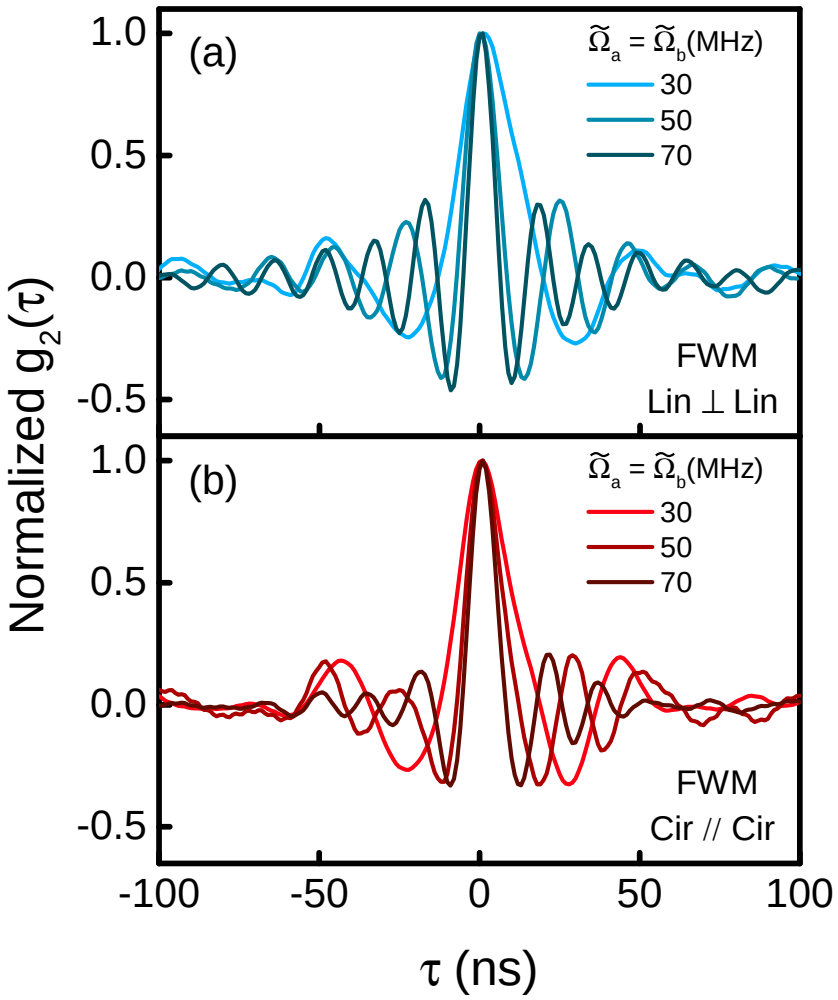

Source: The author (2023).

input intensity of 0.15 mW/cm^2, while the results for FWM signals in Fig. 48 are for different intensities in each case. In the latter we do so to maximize the signals for each detuning, otherwise, the signal-to-noise ratio would not allow us to properly visualize the correlation. However, if we consider the generalized Rabi frequency $\overline{\Omega} = \sqrt{\Omega^2 + \delta^2}$, it is approximately equal to the detuning since the Rabi frequency of the input beams is close to the natural linewidth of the transition.

These results show that the second-order correlation function behaves differently when the detuning is changed. Moreover, there seems to be a main frequency component that depends linearly on the detuning, or more precisely, on $\overline{\Omega}$. Therefore, we hypothesize that these oscillations in the second-order correlation function are directly connected to the generalized Rabi frequency. This means that during the process

of conversion of phase fluctuations of the laser into intensity fluctuations through its interaction with the atomic medium, the intensity fluctuations oscillate at approximately the generalized Rabi frequency [39]. One could expect to see this oscillation in the raw data, that is, in the time series shown in Fig. 44. However, these oscillations are not noticeable in this case because the measurements were taken long after the transient period when the oscillations would be less noticeable. Additionally, the signal we acquire is the average signal of the light emitted by the atomic ensemble, rather than by a single atom.

On the other hand, a higher-order measurement should be able to retrieve the spectral information of the system [109, 126]. This is possible with the intensity fluctuations correlation function $G_{ij}^{(2)}(\tau)$, which does have a noticeable spectral peak. The Fourier analysis of these curves (Figs. 47 and 48) shows that there is a spectral peak that is compatible with the generalized Rabi frequency, or when the laser intensity is small, compatible with the detuning. See, for example in Fig. 49, the Fourier transform of the second-order correlation function for transmission signals (see of Fig. 47). In this case, the generalized Rabi frequencies are 10, 20 and 40 MHz, while the spectral peaks are located at 14, 24 and 37 MHz, respectively. We expect this to be an approximate result because even for a simple two-level system, the presence of spontaneous emission decay modifies how the temporal solution of the optical Bloch equations oscillates. However, the values should be close to $\overline{\Omega}$.

To verify this claim, we plot in Fig. 50 the spectral peak present in each correlation curve (red dots) compared with the absolute value of the detuning (solid line). There is a reasonable agreement between the two results, supporting our argument. One can see in the transmission case (see Fig. 50(c) and (d)) that, near resonance, the spectral peak of the correlation curves moves away from the detuning as the Rabi frequency gets more relevant to the generalized Rabi frequency.

One final comment on the results of the correlation between FWM signals is related to why we observe a positive correlation and not a competition between signals, that is, an anti-correlation. Yang *et al* [38] observed an anti-correlation between FWM signals in an atomic vapor using a Λ-sytem. This situation compares to our results using linear and perpendicular configurations. Our case differs from theirs because the

Figure 49 – Fourier transform of $G_{ij}^{(2)}(\tau)$, for two transmission signals with linear and orthogonal polarizations.

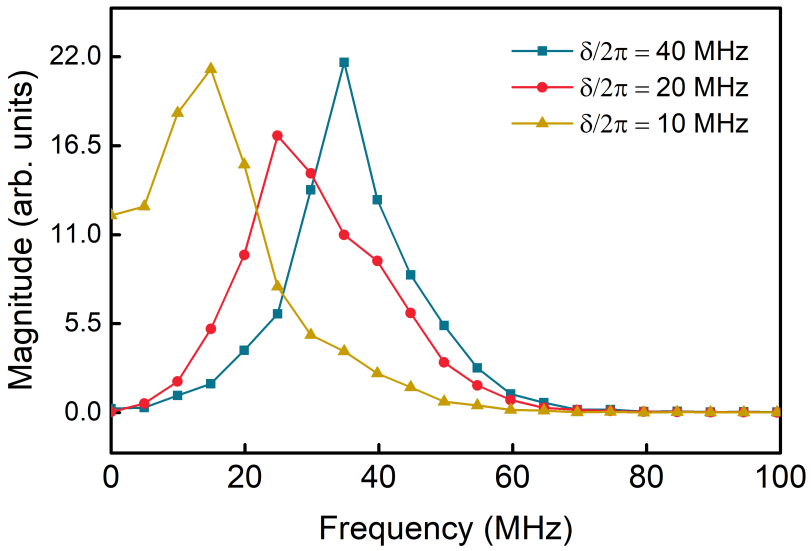

Source: The author (2023).

ground states are degenerate, rendering a symmetrical system that forbids competition between the fields. The results of Ref. [40] show how this degeneracy controls the correlation by introducing an external magnetic field that can break the degeneracy, and change from perfect correlation to anti-correlation.

5.3 Theoretical model

In this subsection, we use the theoretical model presented in Ref. [40] to analyze the correlations between the transmission signals in our system. While the model does not explicitly consider the FWM signals, we believe that some of the analysis can be extrapolated to this case. We focus on the dependence of the correlation with the detuning, paying particular attention to the presence of Rabi oscillations. Our system is well-suited for this analysis on the detuning dependence as the Doppler broadening can be neglected in cold atomic systems.

To begin with, we write the Bloch equations for our three-level system, similar to what was done in the previous sections. However, we now consider that the input electric fields have a stochastic phase which will render in the amplitude fluctuations we

Figure 50 – Frequency of the oscillation in the correlation function for FWM signals with (a) linear and orthogonal polarizations and (b) circular and parallel polarizations; Transmission signals with (c) linear and orthogonal polarizations and (d) circular and parallel polarizations. The solid lines are the absolute value of the detuning.

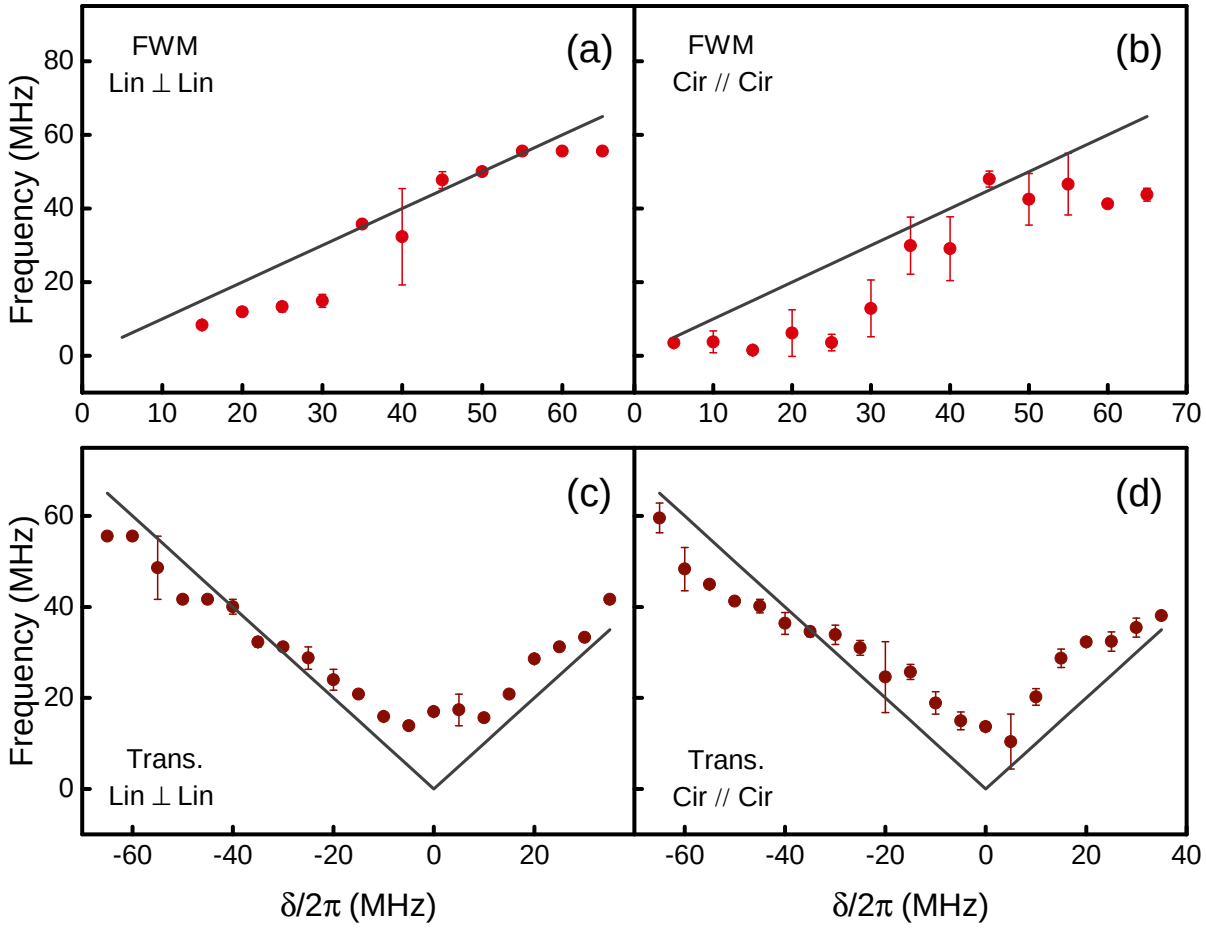

Source: The author (2023).

observe. The input fields are then

$$\begin{aligned}\mathbf{E}_a &= \left[\varepsilon_a(t)e^{-i(\omega_a t+\phi(t)-k_a z)}+c.c.\right]\frac{(\hat{\sigma}^+ + \hat{\sigma}^-)}{\sqrt{2}},\\ \mathbf{E}_b &= \left[\varepsilon_b(t)e^{-i(\omega_b t+\phi(t)-k_b z)}+c.c.\right]\frac{(i\hat{\sigma}^+ - i\hat{\sigma}^-)}{\sqrt{2}},\end{aligned} \tag{117}$$

where ε_l is the amplitude of the electric field, ω_l is the optical frequency, $\phi(t)$ is the fluctuating phase, and $\mathbf{k}_l$ is the associated wave-vector. The polarization vector is represented in the circular base as it highlights how these fields interact with the Λ system.

The fluctuating phase $\phi(t)$ of the input fields are described by a Wiener-Levy diffusion process [127]. For these processes, the average of the stochastic variable is

zero and the average of the two-time correlation is given by $\overline{\langle \dot{\phi}(t)\,\dot{\phi}(t')\rangle} = 2D\delta(t-t')$, where D is the diffusion coefficient.

We recall that, in the previous section, we considered that the field a is tuned in one of the transitions while the field b is tuned in the other. That is, we only take one circular component of each field. A complete treatment of this system, including even wave-mixing processes of superior orders, is performed in Ref. [53]. In this model, they perform a Floquet expansion of the density-matrix elements in the frequency of the input fields and their combinations. One could include a stochastical phase in this last model, but it would take the system from nine coupled equations, as we write it in this work, to a few tens of equations. The numerical solution becomes unstable and demanding in terms of computation time.

The Bloch equations in the rotating-wave approximation can be written as (see section 2):

$$\begin{aligned}
\dot{\rho}_{11} &= -i\sigma_{12}\Omega_a + i\sigma_{21}\Omega_a^* + \Gamma_{21}\rho_{22};\\
\dot{\rho}_{22} &= i\sigma_{12}\Omega_a - i\sigma_{21}\Omega_a^* - i\sigma_{23}\Omega_b^* + i\sigma_{32}\Omega_b - (\Gamma_{21}+\Gamma_{23})\rho_{22};\\
\dot{\rho}_{33} &= i\sigma_{23}\Omega_b^* - i\sigma_{32}\Omega_b + \Gamma_{23}\rho_{22};\\
\dot{\sigma}_{12} &= -\sigma_{12}\left(i\delta_a + \gamma_{12} - \dot{\phi}(t)\right) - i(\rho_{11}-\rho_{22})\Omega_a^* - i\sigma_{13}\Omega_b^*;\\
\dot{\sigma}_{13} &= -\sigma_{13}\left(i\delta_a - i\delta_b + \gamma_{13}\right) - i\sigma_{12}\Omega_b + i\sigma_{23}\Omega_a^*;\\
\dot{\sigma}_{32} &= -\sigma_{32}\left(i\delta_b + \gamma_{23} - \dot{\phi}(t)\right) - i(\rho_{33}-\rho_{22})\Omega_b^* - i\sigma_{31}\Omega_a^*.
\end{aligned} \tag{118}$$

The σ_{jk} terms are the coherences from equation (4) in the rotating frame, whereas Γ_{jk} are the decay rates of the populations. The missing coherence equations are the complex conjugate of the ones presented.

Since the set of Eqs. 118 contains stochastical terms, we must solve them numerically using the so-called Itô's calculus, a mathematical framework for modeling and analyzing systems that are subject to random fluctuations. It was developed by Kiyoshi Itô in the 1940s and has since become an important tool in fields such as finance, physics, and engineering, where it is used to model phenomena such as Brownian motion, option pricing, and noise in electronic circuits.

At the heart of Itô's calculus is the concept of a stochastic differential equation

(SDE). An SDE is a type of differential equation that contains one or more random variables, or "noise terms", which describe the random fluctuations in the system. These noise terms are often modeled using Wiener processes, the stochastical process of a Brownian motion.

To solve an SDE, Itô's calculus introduces the concept of an Itô integral, used to integrate functions of a random variable. This allows one to compute the expected value and variance of the solution to an SDE, as well as to compute higher-order moments and probability distributions. One of the key benefits of Itô's calculus is that it allows one to model systems that are subject to random fluctuations in a rigorous and mathematically precise way. This is particularly useful in fields such as finance [128], where it is used to model the random movements of financial markets, and in physics, where it is used to model the random motion of particles in a fluid.

When it comes to laser fields, the typical stochastical process used to model the fluctuating phase is the Ornstein-Uhlenbeck process [129, 130], which is a continuous-time stochastic process that describes the random evolution of a system over time. It is named after Leonard Ornstein and George Eugene Uhlenbeck, who first introduced the process in 1930 as a model for the Brownian motion of particles suspended in a fluid. It is often used to model systems that exhibit a certain degree of "damping" or "friction", meaning that the system tends to an equilibrium state over time.

This process satisfies the SDE:

$$dX_t = \alpha\,(\gamma - X_t)\,dt + \beta\,dW_t \tag{119}$$

where the Itô's diffusive process dX_t has a deterministic part and a stochastic one. The deterministic term, the first one, has a magnitude of the mean drift α while the asymptotic mean is γ. If $X_t > \gamma$ the drift will be negative and the process will go towards the mean. If $X_t < \gamma$ then the opposite happens, the drift is positive and the process moves away from the mean. As for the stochastic part, it is a Brownian motion W_t with a magnitude constant β.

These properties make the Ornstein-Uhlenbeck process useful for modeling a wide range of systems that have a stationary distribution, i.e., systems that reach a

steady state over time. In addition, the Ornstein-Uhlenbeck process has a finite variance, meaning that the state of the system exhibits a certain level of “stability”. This is in contrast to a simple random walk, where the variance of the system grows without bounds over time.

Once the diffusion process is chosen, we can solve the system of SDEs. There are several different methods for solving SDEs, depending on the specific form of the equations and the properties of the system being modeled. One common method for solving SDEs is the Euler-Maruyama method, which is a numerical approximation method that uses the Euler method to approximate the solution to the SDE at discrete time steps. It is a method relatively simple to implement and is well-suited for systems with relatively smooth dynamics. In the reference we are basing this model (Ref. [40]), the authors use this method. However, it can be prone to numerical instability and may not be accurate for systems with highly nonlinear or singular dynamics.

Another way to solve the SDE system is with the Runge-Kutta method. It is a similar algorithm to the Euler-Maruyama method, as it uses a series of discrete time steps to approximate the solution to the SDE, but with different techniques to improve the accuracy of the approximation. In addition to numerical approximation methods, there are also analytical methods for solving SDEs in certain cases. For example, if the SDE has a linear form and the noise term is additive, the solution can be found using the Laplace transform or the Fourier transform. If the SDE has a quadratic form and the noise term is multiplicative, the solution can be found using the Fokker-Planck equation.

In our case, we opt for solving the system of SDEs numerically using the Runge-Kutta algorithm for scalar noise (*Mathematica* notebook available in appendix D). It is a generalization of the Euler method, and similarly to the deterministic Runge-Kutta method, it involves dividing the time interval of interest into a series of discrete time steps. At each time step, the solution to the SDE is approximated using a weighted average of the function at the current time step and its derivative at several points within the time step. This algorithm possesses a good accuracy for our problem, with a thin distribution of residuals. We also use the same Brownian increment dW_t for both one-photon coherences, as the original fluctuation comes from a single laser. Finally, we probed several choices of parameters of the Ornstein-Uhlenbeck process, but the

outcomes are not drastically different as long as the variance of the process, given by $\beta^2/2\alpha$, is small.

Once the numerical simulation is complete, we can use the time series of the elements of the density matrix to calculate the second-order correlation function for the intensity fluctuations. However, we need to establish the connection between the density matrix elements and the actual detected signal. To do this, we solve the wave equation derived from Maxwell's equations with the same procedure and approximations of the last section, rendering the differential equation

$$\frac{\partial \Omega_l}{\partial z} = i\kappa_{2j}\sigma_{2j}, \tag{120}$$

where $\kappa_{2j} = \frac{\omega_l N \mu_{2j}^2}{2\hbar\varepsilon_0 c}$ and N is the number of atoms.

Solving this equation leads to the fields we detect in the experiment after they propagate in the sample. To do so, we can perform an approximation that simplifies the solution: the MOT diameter L is much smaller than the Rayleigh length of the fields in play, therefore, it is adequate to consider the thin-medium regime. This implies that, in a first-order approximation, we detect a superposition of the input and the generated fields

$$\Omega_l \approx \Omega_l^0 + i\kappa_{2j} L \sigma_{2j}. \tag{121}$$

We are interested in the intensity itself, which scales with the square of the Rabi frequency, therefore (in first-order):

$$I_l \approx \left[\Omega_l^0\right]^2 + \Omega_l^0 \kappa_{2j} L \mathrm{Im}\left(\sigma_{2j}(t)\right). \tag{122}$$

Since the generated field is much weaker than the input fields, the first term acts as the average signal. Hence, only the second term should present intensity fluctuations, as it is explicitly connected to the one-photon coherence. Therefore

$$\delta I_l = \Omega_l^0 \kappa_{2j} L \mathrm{Im}\left(\delta\sigma_{2j}(t)\right). \tag{123}$$

To calculate the second-order correlation function of the intensity fluctuations we can rewrite Eq. 116 as:

$$G^{(2)}(\tau) = \frac{\langle \mathrm{Im}(\delta\sigma_{21}(t))\,\mathrm{Im}(\delta\sigma_{23}(t+\tau))\rangle}{\sqrt{\left\langle [\mathrm{Im}(\delta\sigma_{21}(t))]^2 \right\rangle \left\langle [\mathrm{Im}(\delta\sigma_{23}(t))]^2 \right\rangle}}. \tag{124}$$

Notably, in the model, as it is, only the transmission results can be directly explored. However, as our numerical solution renders the elements of the density-matrix in all orders, the nonlinear effects of wave-mixing are also built in the one-photon coherence. Naturally, the stronger term should be the lower-order one, which is indeed connected to the transmission.

5.3.1 Theoretical results

After performing a numerical simulation of the time series for the transmission signals by solving a system of coupled SDEs, we present an example of a single realization of the series in Fig. 51(a) for a detuning of $\delta/2\pi = 30$ MHz and Rabi frequencies of $\Omega_a = \Omega_b = 0.1\Gamma$. We simulate the signal for a total of 20 μs, but we exclude the first half of the series to ensure that the transient period is not present. Using Eq. 124, we calculate the second-order correlation function for the series shown in Fig. 51(a) and present the results in Fig. 51(b).

Since we use the same Brownian increment dW_t for both signals, they must be perfectly correlated as in Fig. 51(b). It is easy to introduce different increments for each input field and control how large their correlation is by stating that $dW_t^{(1)} = dW_t^{(2)} + \sqrt{1-\rho^2}dW_t^{(3)}$, where ρ ranges from zero to one; that is, one increment is equal to the other with the addition of a third increment. However, we use a single cw laser, so the stochastic phase each input field carries should be the same.

We presented the case of cross-correlation between input field intensity fluctuations for the scenario with linear and perpendicular polarizations. If we eliminate one of the ground states and, therefore, all the equations and terms connected to it in Eqs. 118, then we would have a two-level system. This is the scenario with circular and parallel polarizations. However, as the results are remarkably similar to those in Fig. 51, we do not present them here.

Figure 51 – (a) Numerical simulation of a time series of the intensity fluctuations for the transmission signals with input Rabi frequency $\Omega_a = \Omega_b = 0.1\Gamma$, detuning from the excited state of $\delta/2\pi = 30$ MHz and linear and orthogonal polarizations. (b) Second-order correlation function $G^{(2)}_{ij}(\tau)$ between the time series of (a).

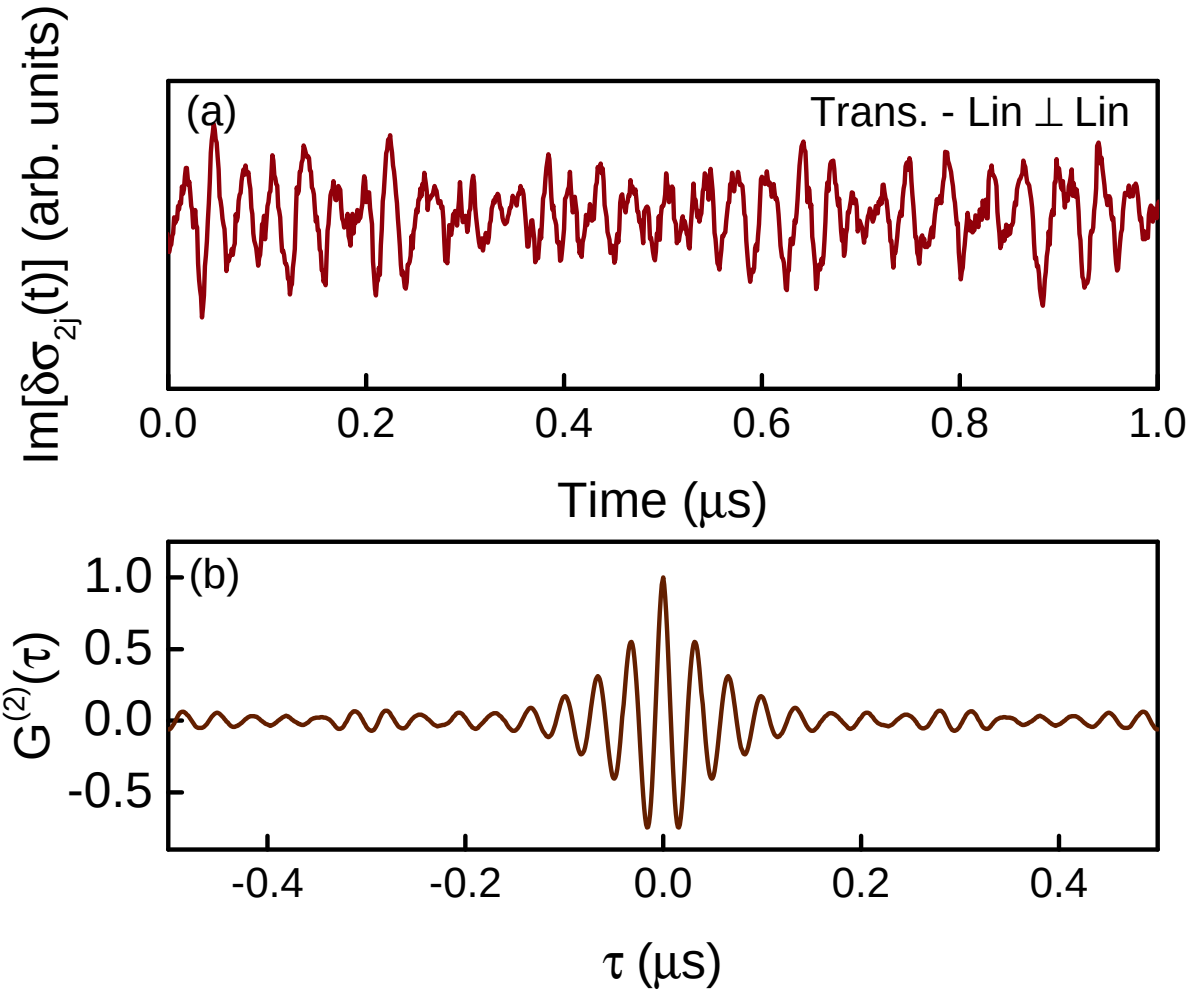

Source: The author (2023).

A theoretical map such as the one presented in Fig. 47 can be achieved and it is presented in Fig. 52(a). It shows a broadening of the correlation peak compatible with the behavior of the experimental result. Moreover, the theoretical results highlight the oscillation of the correlation curve in the generalized Rabi frequency.

A graph similar to the one shown in Fig. 50 is presented in Fig. 52(b) for the transmission signals in the linear and perpendicular polarization case. This graph agrees with the experimental results and therefore supports that the frequency of the oscillation we see in the correlation curves is indeed well described by the generalized Rabi frequency.

We must emphasize that our results were able to reveal this oscillating behavior

Figure 52 – (a) Second-order correlation function $G_{ij}^{(2)}(\tau)$ as a function of the detuning $\delta/2\pi$ between theoretical transmission signals with linear and orthogonal polarizations. The input laser Rabi frequency is $\Omega_a = \Omega_b = 0.1\Gamma$. (b) Frequency of the oscillation in the correlation function of (a). The solid line is the absolute value of the detuning

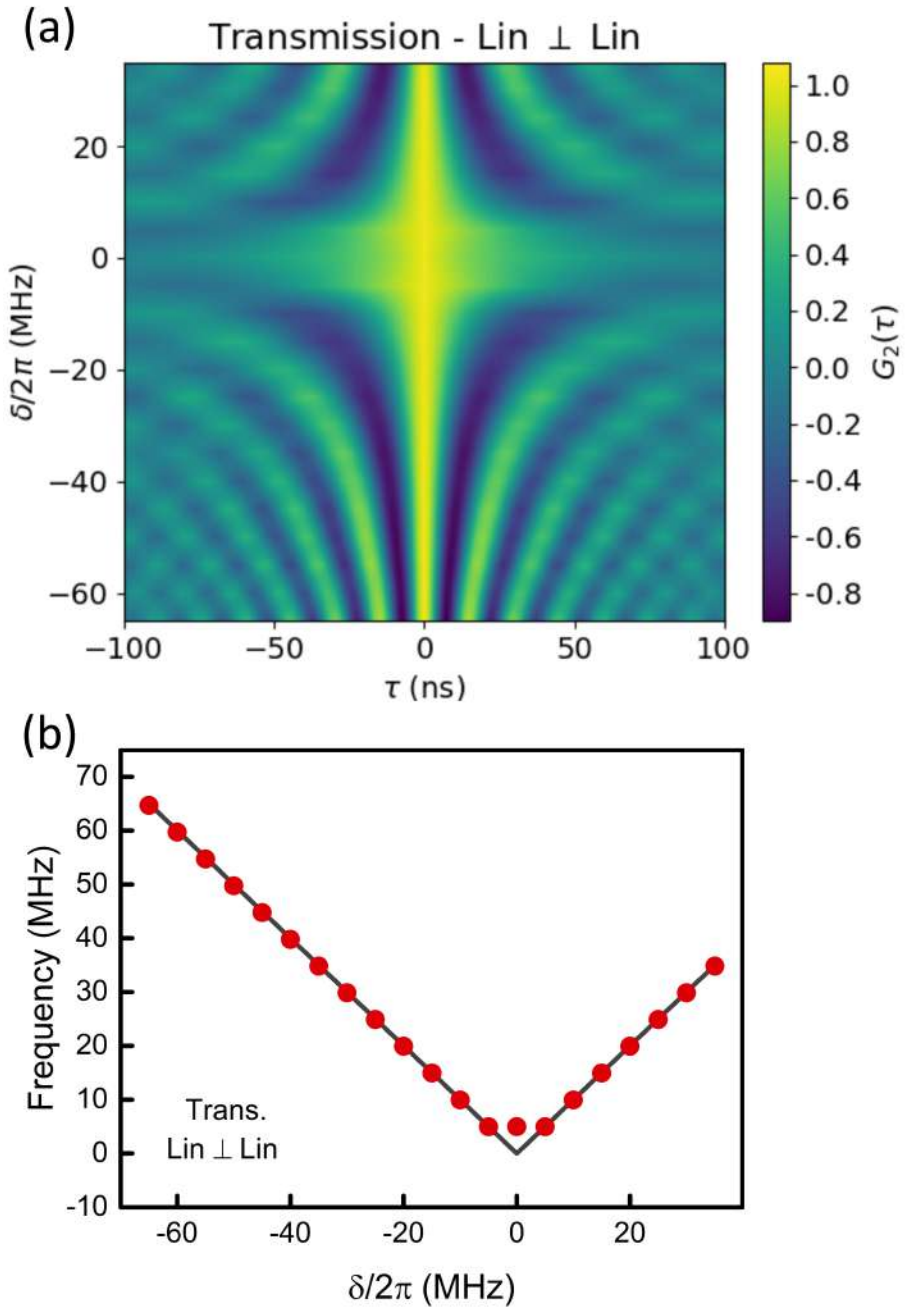

Source: The author (2023).

because the experiments were performed in a cold atom cloud. In a vapor cell, for example, this signature would have been washed away due to the atomic movement. The Doppler integration should change the observation of these oscillations, as the correlation curve would contain the response of several velocity groups.

5.4 Analysis of the FWM spectra

We presented in the first subsection two FWM spectra (see Fig. 42), one for each polarization configuration. The case with linear and orthogonal polarization has a dip around the resonance, which we hypothesize is due to coherent population trapping (CPT).

CPT is a phenomenon that occurs in atomic systems, in which a pair of laser fields interacting with a three-level system, induces a transverse optical pumping that accumulates all the atoms in ground levels near-resonance. This is directly connected to the fact that the optical susceptibility in these systems is purely imaginary, meaning that dispersive effects due to laser detuning from each ground level mutually cancels each other. This phenomenon manifests itself as a dip near resonance in the absorption spectrum [120].

One of the key applications of CPT is in high-precision measurements, where it is used to measure small changes in the frequency or intensity of the laser fields. For example, an important application of CPT is in optical frequency standards, where it is used to create extremely stable and precise frequency references [131, 132].

There is not much literature on this specific configuration we work with, i.e., in which both input fields are scanned in frequency simultaneously. In Ref. [121], the authors comment that, for this specific situation, in which both fields have the same detuning and Rabi frequency, the population will be equally trapped in the lower levels because of the optical pumping, i.e., CPT. This effect holds even for high intensities, which agrees with our experimental results. Let us present them.

To obtain the FWM spectra, we perform the complete FWM measurement in a single time window (see Fig. 41). Therefore, the scanning wave of the injection current of the input laser has a 250 Hz frequency. The amplitude of the ramp depends on the

Figure 53 – (a) Transmission of the input beams both with I ≈ 10 mW/cm^2. (b) FWM spectra using a single laser. Inset: $2\mathbf{k}_a - \mathbf{k}_b$ signal using parallel circularly polarized input beams. All curves are normalized.

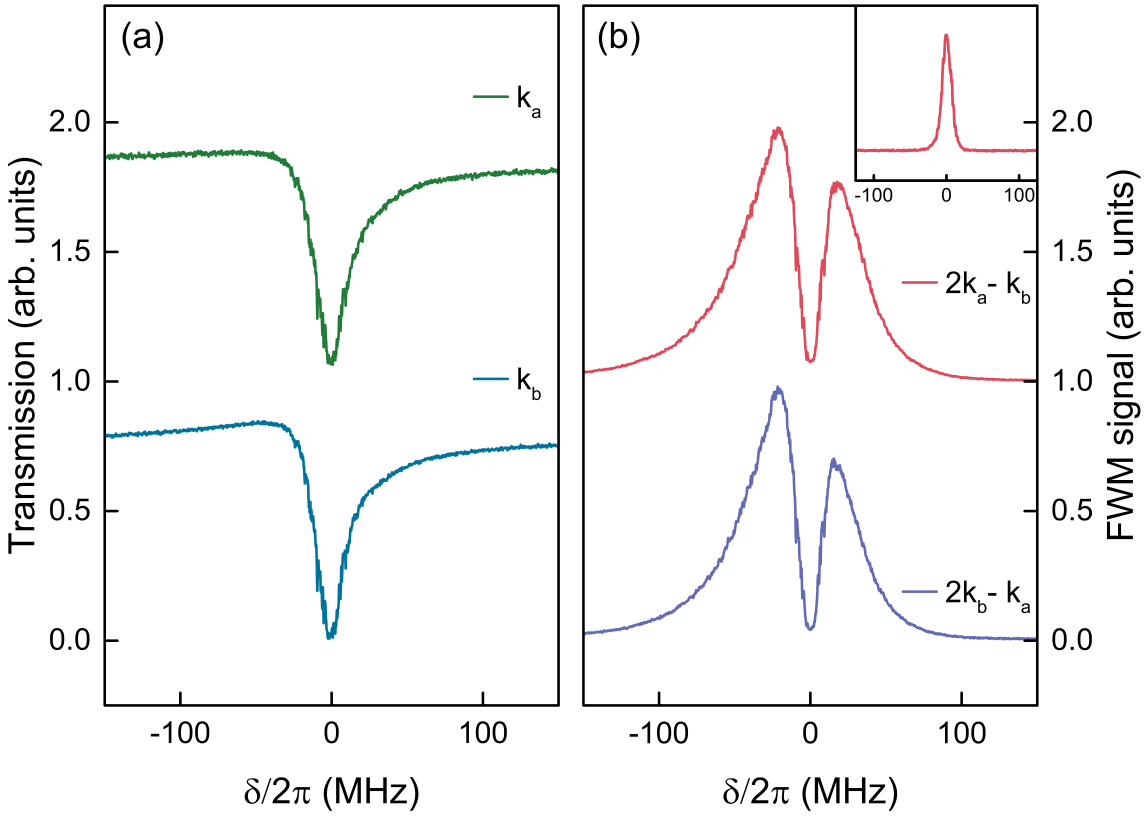

Source: The author (2023).

intensity of the input beams since they are copropagating and, therefore, tend to push the atoms away from the center of the chamber. This radiation pressure is higher on resonance, so we cannot scan the FWM laser slowly, otherwise the atoms would gain too much velocity and leave the trap.

We present a typical result for this single laser setup in Fig. 53, for a laser intensity of 10 mW/cm^2 for each input beam. The curves in Fig. 53(a) show the transmissions of the input beams, while in Fig. 53(b), we show the spectra of the two FWM signals. The transmission curves are slightly asymmetric, possibly due to the fast scanning of the frequency or even self-focalization effects [133].

The main result is in Fig. 53(b), the FWM spectra, and it presents the dip we are attributing to CPT. In the inset of Fig. 53(b), we present a result for the same FWM process but using parallel and circularly polarized input beams, similar to Fig. 42. We recall that in this case, we are dealing with a pure two-level system as the population is pumped through the Zeeman sublevels until it reaches the larger m_f state. Notice

that there is no valley in this result, meaning that the use of beams with perpendicular polarization is crucial to the phenomenon we are addressing.

One could state that this spectral lineshape with a dip on resonance should only be due to absorption effects since we are dealing with highly absorbing media. Another possibility would be an AT splitting caused by the lasers, given that they are, for this particular result, a few times above saturation intensity. If it was the case, the lasers would split the upper level of the transition in two, leading to more than one possible excitation route of the FWM process.

To verify these two initial hypotheses, we change the intensity of the input beams or the density of the atomic sample. We begin the analysis with the results of Fig. 54(a), in which we change the intensity of the two input fields. These three spectra have different intensities of both input beams and the curves are normalized to allow a superposition. There is a power broadening effect, considering that the higher intensity curves have a larger width. Despite that, the valley remains with nearly the same width and depth. In fact, if the intensity of the input beams is within a range of two orders below to two orders above saturation intensity, the valley remains nearly the same shape. It then becomes clear that the AT hypothesis must be ruled out because there should be no splitting below saturation intensity and for high intensities, there should be two well-separated peaks. The absorption hypothesis also loses strength, as it should result in a less pronounced valley for a high-intensity regime.

An additional test to check our first hypothesis is to change the optical depth (OD) of the atomic sample. One can achieve this by using neutral density filters to lower the power of the cooling beams. In our case, the optical depth ranged from $OD \approx 4$ to a lower density regime with $OD \approx 1$, as Fig. 54(c) shows. It is reasonable to expect that, if the valley is exclusively due to absorption, a sample with lower OD would absorb less and consequently produce a shallower dip. However, the spectra show otherwise. There is no significant change in the valley depth regarding this variation of density.

There are additional characteristics of the signal worth mentioning. There is an asymmetry that is possibly related to the frequency scan rate. For slower scans, that is, with the same frequency and smaller amplitudes, the signals can become symmetrical,

Figure 54 – (a) FWM spectra for different intensities of both input beams. (b) FWM spectra for different frequency scan speeds. (c) FWM spectra for different optical depths. All curves are normalized.

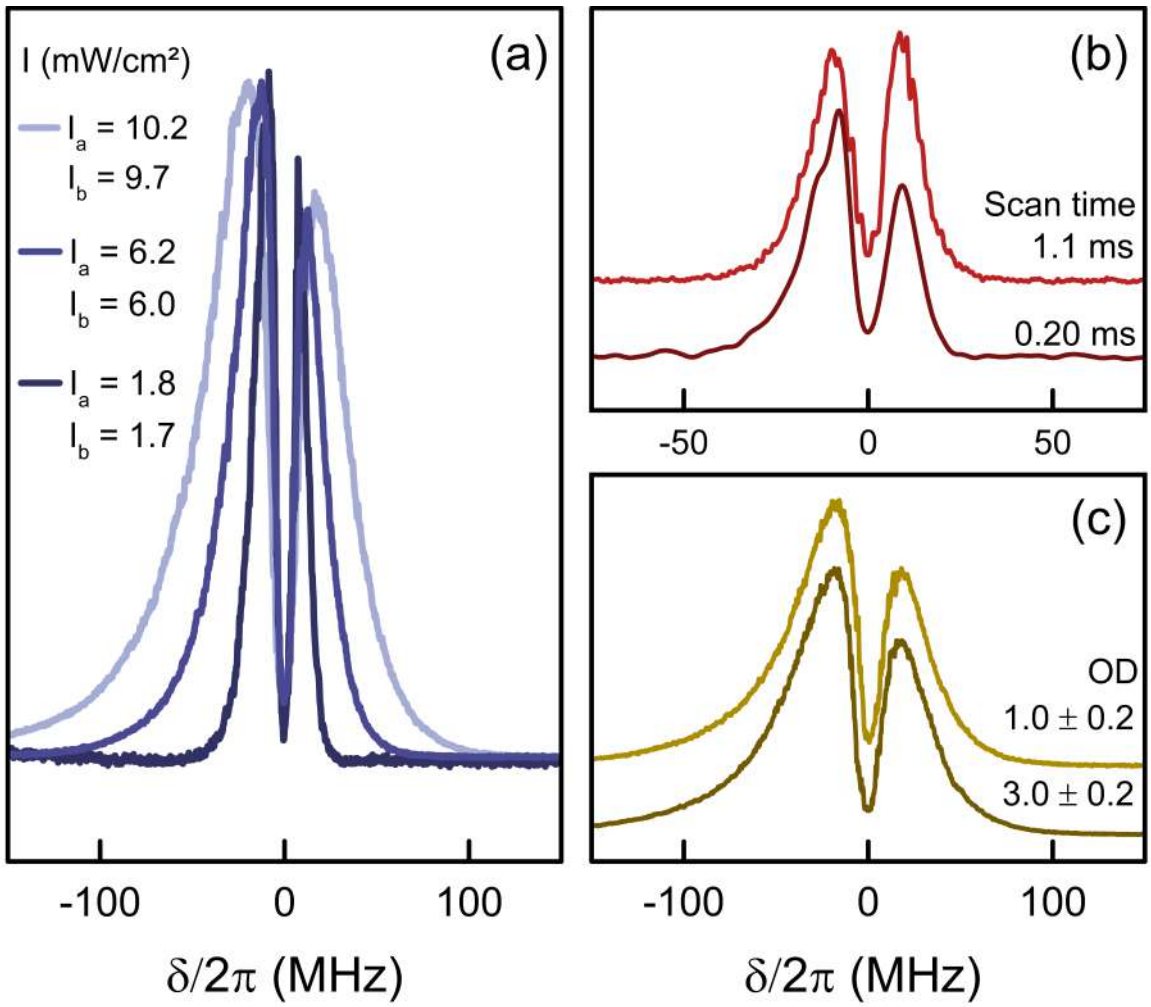

Source: The author (2023).

as Fig. 54(b) shows. However, as mentioned previously, the geometric configuration of the experiment limits the scan rate since, at high intensities, the atoms can be pushed away from the trapping region.

Furthermore, one would expect that the FWM signal in a cold atomic sample would have a narrow profile, closer to the natural linewidth Γ. However, the spectra in Fig. 53 have widths of at least one order of magnitude larger than Γ. Once again, this has to do with the frequency scanning setup. As both fields are varying in frequency, it is reasonable that the signals get a lot broader.

With all this data in hand, it is hard to support the idea of the valley being a result of only absorption or even a level-splitting phenomenon. Had this been the case, we would expect to see the valley depth change as the intensity or sample density

varies. Only in the low-intensity regime, absorption could justify this feature, as the input beam could be entirely absorbed by the atoms in this case. Let us attempt to use the theoretical model we built in section 4 to obtain this dip in the FWM spectra and hopefully find supporting arguments for the CPT hypothesis.

5.4.1 Theoretical FWM spectra

We use the same set of the equations of section 4, that is, without any stochastical phase, as the problem we are dealing with now is the FWM spectra. However, instead of taking a numerical solution, let us look for an analytical expression taking Eq. 86 as the initial step.

We calculate perturbatively the population difference between excited and ground states. To do so we consider two approximations: first, the system is closed, that is, $\sum_{j=1}^{3}\rho_{jj}=1$; second, both ground states have the same populations, $\rho_{11}=\rho_{33}$. These two considerations eliminate part of the Bloch equations, so the solution for the population difference becomes simple:

$$\rho_{11}-\rho_{22}=\rho_{33}-\rho_{22}=\frac{(\Gamma_{21}+\Gamma_{23}+\gamma')}{2(\Gamma_{21}+\Gamma_{23}+\gamma')+3\zeta(\delta_a,\delta_b)}. \tag{125}$$

The $\zeta(\delta_a,\delta_b)$ function contains all of the detuning dependence and it can be written as

$$\zeta(\delta_a,\delta_b)=\frac{2|\Omega_a|^2(\gamma_{12}+\gamma')}{\delta_a^2+(\gamma_{12}+\gamma')^2}+\frac{2|\Omega_b|^2\gamma_{32}+\gamma'}{\delta_b^2+(\gamma_{32}+\gamma')^2}. \tag{126}$$

In this last step, we cut off high-order terms. Namely, we restrain our solution of the population difference to terms of the order of $\left|\Omega_{a,b}\right|^2$.

Once we substitute these population differences into Eq. 86, we can write the coherence σ_{21}'. This density-matrix element is behind the generation of the FWM field with frequency $\omega_s=2\omega_a-\omega_b$, wave-vector $\mathbf{k}_s$ in the direction of $2\mathbf{k}_a-\mathbf{k}_b$, and circular polarization. It is described by Eq. 87.

Since the angle between the input fields is small, and so is the atomic sample length, we consider that the phase-matching condition is fulfilled, that is, $\Delta\mathbf{k}=2\mathbf{k}_a-\mathbf{k}_b-\mathbf{k}_s=0$. Therefore, the FWM signals are proportional to the modulus square of the

sum $\sigma'_{21} + \sigma'_{23}$. However, to take into account the absorption of the generated FWM field and the input beams we must include the propagation of these fields through the atomic medium using the same procedure we performed in section 4. However, since the MOT provides a highly absorbing medium, we will not use the non-depleted input approximation as we did previously with hot vapor.

Therefore, the Rabi frequencies of the input fields and the FWM field are given by the coupled equations

$$\frac{\partial \Omega_a}{\partial z} = -\kappa_{12}\frac{(\rho_{11}-\rho_{22})\Omega_a}{-i\delta_a+\gamma_{12}+\gamma'}; \tag{127a}$$

$$\frac{\partial \Omega_b}{\partial z} = -\kappa_{32}\frac{(\rho_{33}-\rho_{22})\Omega_b}{-i\delta_b+\gamma_{32}+\gamma'}; \tag{127b}$$

$$\frac{\partial \Omega_s}{\partial z} = \frac{-\kappa_{12}(\rho_{11}-\rho_{22})\Omega_s}{-i\delta_{a+}+\gamma_{12}+\gamma'} - \frac{\kappa_{12}\tilde{\sigma}_{31}\Omega_a}{-i\delta_a+\gamma_{32}+\gamma'}, \tag{127c}$$

where the constant $\kappa_{jk} = \frac{\omega_l N \mu_{jk}^2}{\hbar \varepsilon_0 c}$, and k_l is the wavenumber. We emphasize that we considered the phase-matching condition to be fulfilled $\Delta\mathbf{k} = 2\mathbf{k}_a - \mathbf{k}_b - \mathbf{k}_s = 0$. We solve these equations numerically with a fourth-order Runge-Kutta method from $z = 0$ to $z = 4$ mm.

Once this system of coupled Rabi frequencies is solved, we can plot the theoretical FWM spectra. Since in the experiment we scan the input fields simultaneously, in the following plots the detunings are $\delta_a = \delta_b = \delta$. We consider three scenarios in Fig. 55: (i) without absorption of the input beams, that is, it derivatives of Eq. 127(a) and (b) are zero; (ii) with a decay rate of the coherence between ground states γ_{13} too large, preventing the CPT from happening; (iii) the full solution including the absorption, that is, using the Rabi frequencies that are the solution of Eqs. 127 to obtain $|\Omega_s|^2$ and the decay rate γ_{13} is set as ten orders below the population decay rate. The results will not change as long the condition $\gamma_{13} \ll \Gamma_{21}$ holds. Most of the numerical parameters for these plots come from Ref. [46], such as the natural linewidth ($2\pi \cdot 6.065$ MHz). The number of atoms in the MOT is estimated using the fluorescence detected at a solid angle and set as $8 \cdot 10^8$ atoms.

Our theoretical result considering constant input fields (Fig. 55(b)) achieves a

Figure 55 – (a) Experimental spectra; Theoretical spectra with (b) constant input fields; (c) $\gamma_{13} \gg \Gamma$; (d) a Full solution, including absorption and CPT. All curves are normalized.

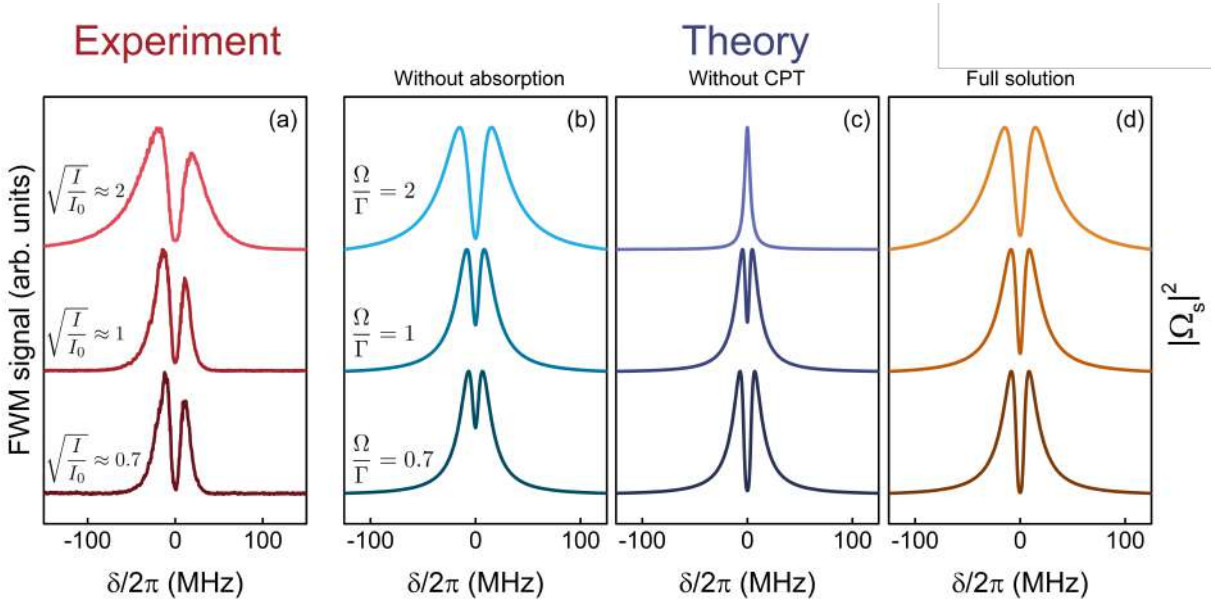

Source: The author (2023).

good agreement with the experimental spectra (Fig. 55(a)) in the high-intensity regime. The model reproduces the width and there is a dip in the spectrum. However, if the intensity is smaller than the saturation intensity, or, the Rabi frequency is smaller than the natural linewidth, the dip vanishes.

On the other hand, we can modify the decay rate γ_{13} to be much larger than any other decay rate of the system, meaning that the coherence σ_{13} decays much faster and therefore forbids the superposition of ground states to happen, which avoids the CPT. In this case (see Fig. 55(c)) the dip only appears in the low-intensity regime due to absorption but does not appear in the high-intensity regime.

Finally, we recover the experimental lineshape by adding the possibility of the input fields being absorbed by the medium and stating that $\gamma_{13} \ll \Gamma_{21}$. With this addition, the agreement is successful for high and low input intensities, as Fig. 55(d) shows.

The key to understanding the presence of this valley in the FWM spectrum is in the coherence σ_{13}. For this very particular situation, in which we scan the frequency of both incident fields, this coherence should last longer than the other coherences of the system, as they are connected to the resonance with the excited level. σ_{13}, on the other hand, exists long before the lasers arrive at the resonance frequency. Therefore, to

plot the theoretical spectra, we must consider that γ_{31}, the decay rate of the coherence between ground states, is much smaller than the other rates of the system.

In this case, the real part of σ_{13} presents a sharp valley only at the resonance, since the imaginary part is zero [120] (see Eq. 86). This implies that there is a non-absorption resonance for $\delta = 0$ [54] due to the transverse optical pumping of the population. This supports the hypothesis that we are observing a manifestation of CPT [120, 134].

We must emphasize, however, that this is an atypical manifestation of CPT, due to our frequency scanning configuration with both input fields changing simultaneously. In a typical CPT, for this type of level system, one would expect a sharp dip in an absorption spectrum. However, we are observing the phenomenon in a forward FWM signal with this very particular frequency scanning setup, which broadens the entire signal. Therefore, the dip caused by the CPT is wider than usual.

When we make a different assumption for the decay rate γ_{13} that is to say it is much larger than the other rates in the system, the real part of σ_{31} (once again, the imaginary part is zero) would present a peak for $\delta = 0$ and be zero elsewhere. In this situation, the coherence between ground states vanishes so quickly that it can only exist at the resonance, that is, there is not enough time for the CPT to happen. It is a completely different dynamics. Evidently, in this situation, we cannot achieve the FWM spectrum with a valley on resonance.

Using the appropriate numerical value for the decay rate of the coherence between ground states, we present a complete comparison between experimental and theoretical spectra in Fig. 56 for different intensity values of the incident fields. In this case, we consider the model of Fig. 55(d).

The colormaps of Fig. 56 make it clear that we can successfully reproduce with a good agreement the valley and the width of the spectra for this range of intensities. The asymmetry of the experimental results is not present in the model, but as we discussed previously, it is connected with the frequency scan rate. To model this feature, one would need to solve the Bloch equations in the time domain and not assume a steady-state solution as we do. We have implemented a time solution of the Bloch equations to all

Figure 56 – Comparison between experimental and theoretical FWM spectra for different intensities of the input fields. The plots are normalized individually.

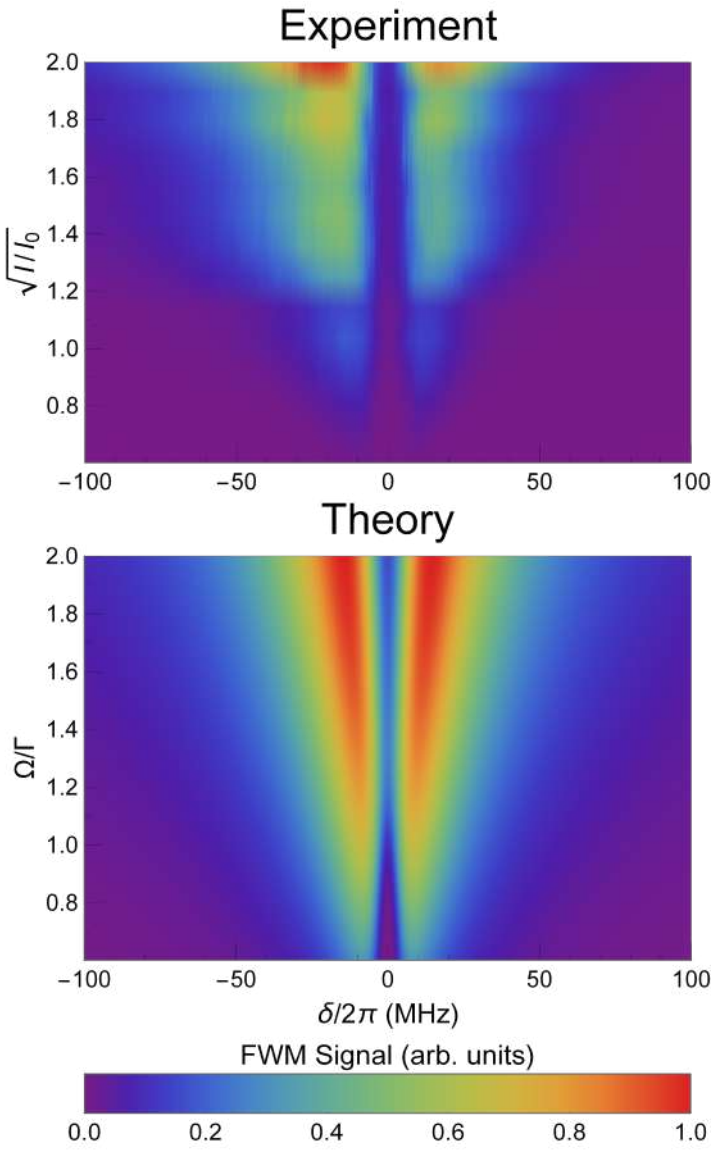

Source: The author (2023).

orders and it supports this hypothesis of the asymmetry being connected to the scan rate. For faster scans, the signal gets more asymmetrical as in the experiment [135].

On the other hand, the theoretical solution fails to agree with the experiment for higher intensities of the input lasers. The dip in the FWM spectra starts to get wider, in disagreement with the experiment that shows almost no change in the dip width for input intensities of ten times the saturation intensity. Once again, we cite Ref. [53], in which the authors perform a Floquet expansion of the density-matrix elements in the frequency of the input fields and their combinations. This way they can model any high-order phenomenon in the high-intensity regime by writing a continuous-fraction

solution that includes all orders of interaction. This type of procedure could improve the agreement with our experimental results.

The results described in this section were submitted as a regular article in the Physical Review A:

A. A. C. de Almeida, M. R. L. da Motta, and S. S. Vianna, “Intensity correlations in the forward four-wave mixing driven by a single pump”, Phys. Rev. A 107, 023515 (2023).

6 CONCLUSIONS

We have successfully executed the three four-wave mixing (FWM) experiments we proposed, observing in each case different aspects and phenomena. We were also able to build theoretical models that, to some extent, did fit the experimental data.

In the first place, we have presented our findings on the dynamic Stark shift and interference between excitation routes in the coherent blue light (CBL) signal obtained through an FWM process in section 3. The geometrical configuration with copropagating beams was critical to the observed phenomena and it is one of the characteristics of our experiment that makes the results unique. Furthermore, we have theoretically modeled the Autler-Townes (AT) splitting pattern in a dressed cascade three-level system using a numerical calculation of the Bloch equations. This allows us to compare the response of the CBL signal and the blue fluorescence given by the upper-level population for homogeneously and non-homogeneously broadened medium.

We found that in the case of homogeneous broadening, the response did not depend on whether the beams were copropagating or counter-propagating. The AT doublet was present in both fluorescence and FWM signals when the weak beam frequency was sweeping, but this doublet pattern was indistinguishable in the strong field frequency scanning regime.

On the other hand, for a Doppler-broadened medium, we found that the response depends on whether the beams are copropagating or counterpropagating, and which beam is sweeping. In this case, an interesting result was observed when the beams traveled in the same direction: a doublet structure was seen in the FWM signal for both scanning regimes, but not in the fluorescence signal. Noteworthy, we highlighted the physical mechanism behind this doublet structure and how it varies depending on the scanning regime. In a weak field scanning regime, the doublet structure is directly related to the contribution of the AT effect from all velocity groups. However, in the strong field scanning regime, the two peaks correspond to the most distant peaks of the resonance due to two AT doublets from different velocity groups.

We observed an interference effect between two possible FWM excitation routes when two modes of the 1GHz mode-locked laser are resonant with one- and two-photon transitions for the same atomic velocity group. This interference resulted in a narrow peak on top of an Autler-Townes doublet when we scanned the repetition rate of the frequency comb. This process allows us to selectively probe a specific velocity group of atoms in the medium. Our model supports the idea that this narrow structure is caused by interference between the two excitation pathways. These results demonstrate that the combination of a continuous-wave laser and a 1 GHz frequency comb can create different pathways that may lead to non-trivial quantum interferences.

Subsequently, in section 4, we presented a study on the excitation spectra of two symmetrical FWM signals generated in rubidium vapor, using a copropagating laser beam configuration. The nonlinear signals were produced by two separate lasers that were both tuned to the closed transition of ^{85}Rb $5S_{1/2}(F=3) \rightarrow 5P_{3/2}(F=4)$, resulting in a single peak in each spectrum. While this type of degenerate FWM process is well-known, we simultaneously detected and analyzed the symmetry between the two signals. Our results showed anomalies in the atomic medium's index of refraction due to the interaction with both fields.

One interesting aspect of this experiment is that, although the two signals were generated by separate FWM processes, they provide information on the dynamic of an ensemble of atoms that interacted simultaneously with the same excitation fields. This characteristic can be used to investigate the interaction between atoms within the excitation region or to study correlations induced by the atomic system. Specifically, the degeneracy of the nonlinear process combined with the field configuration leads to symmetry in the signals, both spatially and in frequency, regardless of which beam is used to probe the excitation spectrum.

The anomalies in the refractive index were revealed through two experimental features: (i) an absorption dip in the transmission of the frequency-scanning beam, similar to an electromagnetically induced absorption process, and (ii) a frequency shift of both FWM signals in opposite directions, determined by the phase-matching condition. Our theoretical analysis, which was applied to a three-level system, demonstrated how the index of refraction seen by each beam can change during the interaction process.

Importantly, the correct description of the frequency position of each peak is supported by a variable refractive index for both lasers, with the scanning laser experiencing an anomalous window in the refractive index near resonance.

Finally, in section 5, we successfully presented an experiment to study the FWM process using atoms cooled by a magneto-optical trap (MOT), in a copropagating configuration of the input beams. The experiment was designed to generate two similar FWM signals in distinct directions. We have successfully demonstrated that there are temporal correlations between intensity fluctuations of two distinct degenerate FWM signals in a cold rubidium sample. It is noteworthy that this is the first demonstration of these correlations in degenerate FWM processes, which due to this degeneracy, do not present competitive signals and therefore have a positive correlation between them. In a complementary scenario to ours are the results of Ref. [38] that present an anticorrelation between FWM signals due to the nondegeneracy of the ground states.

Furthermore, since our cold atomic system allows a proper definition of detuning, namely, there is not a significant Doppler broadening, we can study how the correlation between FWM signals and transmission signals behave as a function of detuning. The results show that the system exhibits Rabi oscillations that can be revealed by the second-order correlation function long after the transient. The theoretical model from Ref. [40] was used to provide numerical results for the transmission signals that support the experimental findings. Even though the model only deals with the transmission signals, it provides a good insight that the mechanism behind the correlations, and the Rabi oscillations we see in them, is the conversion of phase-noise to amplitude-noise due to the interaction of the laser with the atoms. The FWM signals should follow a very similar behavior, so we believe that the results regarding the cross-correlation between transmission signals can be extrapolated to the nonlinear case.

As for the spectra results, we have presented our hypothesis that the dip in the FWM signal is due to coherent population trapping (CPT). The fact that for high intensities there was no clear separation between the two peaks ruled out the splitting of atomic levels due to the AC Stark effect, i.e. an Autler-Townes splitting. In addition, the linear absorption of the input beams and the generated signal should not be enough to produce such a deep valley in a high-intensity regime. Changing the optical density

of the atomic sample confirmed that the dip should not be complete due to absorption effects, since a low-density sample rendered the same usual FWM spectrum.

To support our interpretation of the features of the FWM signal, we have modeled the process using the procedure of section 4. The model gives evidence that absorption effects are only capable to explain the experimental results for a low-intensity regime, as expected. For high intensities of the input beams, the real part of the Rabi frequency of the generated FWM light dominates the spectrum, which corroborates with the hypothesis of a CPT. However, the model does not achieve a perfect description of the experimental data, especially if the input lasers are too intense.

REFERENCES

1 MAIMAN, T. H. Stimulated optical radiation in ruby. *Nature*, v. 187, p. 493–494, 1960.

2 BLOEMBERGEN, N. Nonlinear optics and spectroscopy. *Rev. Mod. Phys.*, v. 54, p. 685–695, Jul 1982.

3 KERR, J. A new relation between electricity and light: Dielectrified media birefringent. *The London, Edinburgh, and Dublin Philosophical Magazine and Journal of Science*, v. 50, n. 332, p. 337–348, 1875.

4 FRANKEN, P. A. et al. Generation of optical harmonics. *Physical Review Letters*, v. 7, p. 118–119, 1961.

5 KAISER, W.; GARRETT, G. C. B. Two-photon excitation in CaF_2; Eu^{2+}. *Physical Review Letters*, v. 7, p. 229–231, 1961.

6 WOODBURY, E. J.; NG, W. K. Ruby laser operation in the near ir. *Proceedings of the IRE*, v. 50, p. 2347–2348, 1962.

7 MAKER, P. D.; TERHUNE, R. W. Optical third harmonic generation. *Journal of the Optical Society of America*, v. 53, p. 523, 1963.

8 MAKER, P. D.; TERHUNE, R. W. Study of optical effects due to an induced polarization third order in the electric field strength. *Phys. Rev.*, v. 137, p. A801–A818, Feb 1965.

9 HARRIS, S. E.; OSHMAN, M. K.; BYER, R. L. Observation of tunable optical parametric fluorescence. *Phys. Rev. Lett.*, v. 18, p. 732–734, May 1967.

10 ABRAMS, R. L.; LIND, R. C. Degenerate four-wave mixing in absorbing media. *Opt. Lett.*, v. 2, n. 4, p. 94–96, Apr 1978.

11 ORIA, M. et al. Efficient phase conjugation of a cw low-power laser diode in a short cs vapor cell at 852 nm. *Opt. Lett.*, v. 14, n. 19, p. 1082–1084, Oct 1989.

12 PINARD, M.; VERKERK, P.; GRYNBERG, G. Backward saturation in four-wave mixing in neon: Case of cross-polarized pumps. *Phys. Rev. A*, v. 35, p. 4679–4695, Jun 1987.

13 CARDOSO, G.; TABOSA, J. Electromagnetically induced grating in a degenerate open two-level system. In: *Technical Digest. Summaries of papers presented at the Quantum Electronics and Laser Science Conference. Postconference Technical Digest (IEEE Cat. No.01CH37172)*. [S.l.: s.n.], 2001. p. 24–25.

14 Resonant nonlinear optics in phase-coherent media. In: BEDERSON, B.; WALTHER, H. (Ed.). [S.l.: s.n.], 2000, (Advances In Atomic, Molecular, and Optical Physics, v. 42). p. 347–386.

15 MA, R. et al. Compact sub-kilohertz low-frequency quantum light source based on four-wave mixing in cesium vapor. *Opt. Lett.*, v. 43, n. 6, p. 1243–1246, Mar 2018.

16 KIM, S.; MARINO, A. M. Generation of 87rb resonant bright two-mode squeezed light with four-wave mixing. *Opt. Express*, v. 26, n. 25, p. 33366–33375, Dec 2018.

17 CHOPINAUD, A. et al. High helicity vortex conversion in a rubidium vapor. *Phys. Rev. A*, v. 97, p. 063806, Jun 2018.

18 OFFER, R. F. et al. Spiral bandwidth of four-wave mixing in rb vapour. *Communications Physics*, v. 1, n. 1, p. 84, Nov 2018. ISSN 2399-3650.

19 KATZIR, I.; RON, A.; FIRSTENBERG, O. Diffraction manipulation by four-wave mixing. *Opt. Express*, v. 23, n. 5, p. 6379–6391, Mar 2015.

20 RIPKA, F. et al. A room-temperature single-photon source based on strongly interacting rydberg atoms. *Science*, v. 362, n. 6413, p. 446–449, oct 2018.

21 LUKIN, M. D. et al. Resonant enhancement of parametric processes via radiative interference and induced coherence. *Phys. Rev. Lett.*, v. 81, p. 2675–2678, Sep 1998.

22 XIA, H. et al. Electromagnetically induced transparency in atoms with hyperfine structure. *Phys. Rev. A*, v. 56, p. R3362–R3365, Nov 1997.

23 FLEISCHHAUER, M.; IMAMOGLU, A.; MARANGOS, J. P. Electromagnetically induced transparency: Optics in coherent media. *Rev. Mod. Phys.*, v. 77, p. 633–673, Jul 2005.

24 AKULSHIN, A. M.; BARREIRO, S.; LEZAMA, A. Electromagnetically induced absorption and transparency due to resonant two-field excitation of quasidegenerate levels in rb vapor. *Phys. Rev. A*, v. 57, p. 2996–3002, Apr 1998.

25 TAICHENACHEV, A. V.; TUMAIKIN, A. M.; YUDIN, V. I. Electromagnetically induced absorption in a four-state system. *Phys. Rev. A*, v. 61, p. 011802, Dec 1999.

26 MUKAMEL, S. *Principles of Nonlinear Optical Spectroscopy*. [S.l.]: Oxford University Press, 1995. (Oxford series in optical and imaging sciences). ISBN 9780195092783.

27 LOMSADZE, B.; CUNDIFF, S. T. Frequency combs enable rapid and high-resolution multidimensional coherent spectroscopy. *Science*, v. 357, n. 6358, p. 1389–1391, sep 2017.

28 AUTLER, S. H.; TOWNES, C. H. Stark effect in rapidly varying fields. *Phys. Rev.*, v. 100, p. 703–722, 1955.

29 ZHOU, H.-T. et al. Influence of the frequency detuning on the four-wave mixing efficiency in three-level system coupled by standing-wave. *Indian Journal of Physics*, v. 92, n. 5, p. 557–563, May 2018. ISSN 0974-9845.

30 YABUZAKI, T.; MITSUI, T.; TANAKA, U. New type of high-resolution spectroscopy with a diode laser. *Phys. Rev. Lett.*, v. 67, p. 2453–2456, Oct 1991.

31 WALSER, R.; ZOLLER, P. Laser-noise-induced polarization fluctuations as a spectroscopic tool. *Phys. Rev. A*, v. 49, p. 5067–5077, Jun 1994.

32 GARDINER, C. W. *Handbook of stochastic methods for physics, chemistry and the natural sciences*. Third. Berlin: Springer-Verlag, 2004. v. 13. xviii+415 p. (Springer Series in Synergetics, v. 13). ISBN 3-540-20882-8.

33 MARTINELLI, M. et al. Noise spectroscopy of nonlinear magneto-optical resonances in rb vapor. *Phys. Rev. A*, v. 69, p. 043809, Apr 2004.

34 CRUZ, L. S. et al. Laser-noise-induced correlations and anti-correlations in electromagneticallyinduced transparency. *Eur. Phys. J. D.*, v. 41, n. 3, p. 531–539, Mar 2007. ISSN 1434-6079.

35 XIAO, Y. et al. Electromagnetically induced transparency with noisy lasers. *Phys. Rev. A*, v. 80, p. 041805, Oct 2009.

36 FLOREZ, H. M. et al. Power-broadening-free correlation spectroscopy in cold atoms. *Phys. Rev. A*, v. 88, p. 033812, Sep 2013.

37 LI, C. et al. Polarization controlled intensity noise correlation and squeezing of four-wave mixing processes in rubidium vapor. *Optical Materials*, v. 55, p. 102–108, 2016. ISSN 0925-3467.

38 YANG, X. et al. Generation of correlated and anticorrelated multiple fields via atomic spin coherence. *Phys. Rev. A*, v. 85, p. 013824, Jan 2012.

39 PAPOYAN, A.; SHMAVONYAN, S. Signature of optical rabi oscillations in transmission signal of atomic vapor under continuous-wave laser excitation. *Optics Communications*, v. 482, p. 126561, 2021. ISSN 0030-4018.

40 ARIUNBOLD, G. O. et al. Intensity correlation and anti-correlations in coherently driven atomic vapor. *Journal of Modern Optics*, v. 57, n. 14-15, p. 1417–1427, 2010.

41 ALLEN, L.; EBERLY, J. *Optical Resonance and Two-level Atoms*. [S.l.]: Dover, 1987. (Dover books on physics and chemistry). ISBN 9780486655338.

42 THE Nobel Prize in Physics 1997. 2019. Nobel Media AB. Available from Internet: <https://www.nobelprize.org/prizes/physics/1997/summary/>. Accessed on: 16 jan 2023.

43 THE Nobel Prize in Physics 2001. 2019. Nobel Media AB. Available from Internet: <https://www.nobelprize.org/prizes/physics/2001/summary/>. Accessed on: 16 jan 2023.

44 FOOT, C. J. *Atomic Physics (Oxford Master Series in Physics)*. 1. ed. Oxford, UK: Oxford University Press, 2005.

45 SHENG, D.; GALVÁN, A. P.; OROZCO, L. A. Lifetime measurements of the $5d$ states of rubidium. *Phys. Rev. A*, American Physical Society, v. 78, p. 062506, Dec 2008.

46 STECK, D. A. *Alkali D Line Data*. 2021. Available from Internet: <https://steck.us/alkalidata/>. Accessed on: 17 jan 2023.

47 LABZOWSKY, L.; GOIDENKO, I.; PYYKKö, P. Estimates of the bound-state qed contributions to the g-factor of valence ns electrons in alkali metal atoms. *Physics Letters A*, v. 258, n. 1, p. 31–37, 1999. ISSN 0375-9601.

48 JACKSON, J. D. *Classical electrodynamics*. 3rd ed.. ed. New York, NY: Wiley, 1999. ISBN 9780471309321.

49 BOYD, R. *Nonlinear Optics*. 3. ed. Orlando, FL, USA: Academic Press, 2008.

50 SAKURAI, J. J. *Modern Quantum Mechanics (Revised Edition)*. 1. ed. [S.l.]: Addison Wesley, 1993. Hardcover. ISBN 0201539292.

51 Cohen-Tannoudji, C.; Grynberg, G.; Dupont-Roc, J. *Atom-Photon Interactions: Basic Processes and Applications*. New York: Wiley, 1992.

52 LOUDON, R. *The Quantum Theory of Light*. Second. Oxford: Clarendon Press, 1983.

53 EILAM, A.; WILSON-GORDON, A. D. Temporal optical memory based on coherent population and two-photon coherence oscillations. *Phys. Rev. A*, v. 98, p. 013808, Jul 2018.

54 ORRIOLS, G. Nonabsorption resonances by nonlinear coherent effects in a three-level system. *Il Nuovo Cimento B (1971-1996)*, v. 53, n. 1, p. 1–24, Sep 1979. ISSN 1826-9877.

55 HARRIS, S. E. Lasers without inversion: Interference of lifetime-broadened resonances. *Phys. Rev. Lett.*, v. 62, p. 1033–1036, Feb 1989.

56 HARRIS, S. E.; FIELD, J. E.; IMAMOGLU, A. Nonlinear optical processes using electromagnetically induced transparency. *Phys. Rev. Lett.*, v. 64, p. 1107–1110, Mar 1990.

57 ANISIMOV, P. M.; DOWLING, J. P.; SANDERS, B. C. Objectively discerning Autler-Townes splitting from electromagnetically induced transparency. *Phys. Rev. Lett.*, v. 107, p. 163604, Oct 2011.

58 HAO, L. et al. Transition from electromagnetically induced transparency to Autler-Townes splitting in cold cesium atoms. *New Journal of Physics*, v. 20, n. 7, p. 073024, jul 2018.

59 SOUZA, M. P. M. de; ALMEIDA, A. A. C. de; VIANNA, S. S. Dynamic Stark shift in doppler-broadened four-wave mixing. *Phys. Rev. A*, v. 105, p. 053128, 2022.

60 MORENO, M. P.; ALMEIDA, A. A. C. de; VIANNA, S. S. Interference effect and Autler-Townes splitting in coherent blue light generated by four-wave mixing. *Phys. Rev. A*, v. 99, p. 043410, 2019.

61 FORTIER, T.; BAUMANN, E. 20 years of developments in optical frequency comb technology and applications. *Communications Physics*, v. 2, n. 1, p. 153, Dec 2019. ISSN 2399-3650.

62 PICQUÉ, N.; HÄNSCH, T. W. Frequency comb spectroscopy. *Nature Photonics*, v. 13, n. 3, p. 146–157, 2019.

63 LUNDBERG, L. et al. Frequency comb-based wdm transmission systems enabling joint signal processing. *Applied Sciences*, v. 8, n. 5, 2018. ISSN 2076-3417.

64 SOUZA, M. P. M. de. *Excitação coerente de um vapor atômico por trens de pulsos ultracurtos e lasers contínuos*. Thesis (Phd) — Universidade Federal de Pernambuco, 2012.

65 FELINTO, D. et al. Coherent accumulation in two-level atoms excited by a train of ultrashort pulses. *Optics Communications*, v. 215, n. 1, p. 69–73, 2003.

66 MORENO, M. P.; VIANNA, S. S. Femtosecond 1 ghz ti:sapphire laser as a tool for coherent spectroscopy in atomic vapor. *J. Opt. Soc. Am. B*, v. 28, n. 9, p. 2066–2069, 2011.

67 LOPEZ, J. P. et al. Coherent blue emission generated by rb two-photon excitation using diode and femtosecond lasers. *Journal of Physics B: Atomic, Molecular and Optical Physics*, v. 50, n. 8, p. 085001, mar 2017.

68 GARCÍA-WONG, A. et al. Velocity-selective spectroscopy of rb vapor with a train of short pulses and a diode laser. *Optics Communications*, v. 427, p. 462–468, 2018.

69 AKULSHIN, A. M. et al. Coherent and collimated blue light generated by four-wave mixing in rb vapour. *Opt. Express*, v. 17, n. 25, p. 22861–22870, Dec 2009.

70 AGARWAL, G. S.; BOYD, R. W. Quantum theory of rabi sideband generation by forward four-wave mixing. *Phys. Rev. A*, v. 38, p. 4019–4027, 1988.

71 MOLLOW, B. R. Power spectrum of light scattered by two-level systems. *Phys. Rev.*, v. 188, p. 1969–1975, 1969.

72 ORTIZ-GUTIÉRREZ, L. et al. Mollow triplet in cold atoms. *New Journal of Physics*, v. 21, n. 9, p. 093019, sep 2019.

73 PIOTROWICZ, M. J. et al. Measurement of the electric dipole moments for transitions to rubidium rydberg states via Autler-Townes splitting. *New Journal of Physics*, v. 13, n. 9, p. 093012, sep 2011.

74 GARCIA-FERNANDEZ, R. et al. Autler-Townes effect in a sodium molecular-ladder scheme. *Phys. Rev. A*, v. 71, p. 023401, Feb 2005.

75 SAGLAMYUREK, E. et al. Coherent storage and manipulation of broadband photons via dynamically controlled Autler–Townes splitting. *Nature Photonics*, v. 12, n. 12, p. 774–782, Dec 2018. ISSN 1749-4893.

76 PENG, Z. H. et al. Vacuum-induced Autler-Townes splitting in a superconducting artificial atom. *Phys. Rev. A*, v. 97, p. 063809, Jun 2018.

77 FENEUILLE, S.; SCHWEIGHOFER, M.-G. Conditions for the observation of the Autler-Townes effect in a two step resonance experiment. *Journal de Physique*, v. 36, n. 9, p. 781–786, 1975.

78 SALOMAA, R.; STENHOLM, S. Two-photon spectroscopy. ii. effects of residual doppler broadening. *Journal of Physics B: Atomic and Molecular Physics*, v. 9, n. 8, p. 1221, jun 1976.

79 DELSART, C.; KELLER, J.-C. The optical Autler-Townes effect in doppler-broadened three-level systems. *Journal de Physique*, v. 39, n. 4, p. 350–360, 1978.

80 AHMED, E.; LYYRA, A. M. Effect of doppler broadening on Autler-Townes splitting in the molecular cascade excitation scheme. *Phys. Rev. A*, v. 76, p. 053407, Nov 2007.

81 ALCOCK, C. B.; ITKIN, V. P.; HORRIGAN, M. K. Vapour pressure equations for the metallic elements: 298-2500k. *Canadian Metallurgical Quarterly*, v. 23, n. 3, p. 309–313, 1984.

82 WHITING, D. J. et al. Direct measurement of excited-state dipole matrix elements using electromagnetically induced transparency in the hyperfine paschen-back regime. *Phys. Rev. A*, v. 93, p. 043854, Apr 2016.

83 WHITING, D. J. et al. Single-photon interference due to motion in an atomic collective excitation. *Phys. Rev. Lett.*, v. 118, p. 253601, Jun 2017.

84 SOUZA, M. P. M. de. *Dynamic Stark Shift*. 2022. Available from Internet: <https://github.com/marcopolomoreno/dynamic-Stark-shift>. Accessed on: 01 jan 2023.

85 GRAY, H.; STROUD, C. Autler-Townes effect in double optical resonance. *Optics Communications*, v. 25, n. 3, p. 359–362, 1978. ISSN 0030-4018.

86 ZUO, Z. et al. Two-photon resonant four-wave mixing in a dressed atomic system: Polarization interference in a doppler-broadened system. *Phys. Rev. A*, v. 75, p. 023805, Feb 2007.

87 RAMÍREZ-MARTÍNEZ, F. et al. Electric-dipole forbidden transitions for probing atomic state preparation: the case of the Autler-Townes effect. *Journal of Physics B: Atomic, Molecular and Optical Physics*, v. 54, n. 9, p. 095002, may 2021.

88 ZHANG, Y. et al. Evidence of Autler-Townes splitting in high-order nonlinear processes. *Opt. Lett.*, v. 35, n. 20, p. 3420–3422, Oct 2010.

89 WHITING, D. J. et al. Four-wave mixing in a non-degenerate four-level diamond configuration in the hyperfine paschen-back regime. *Journal of Modern Optics*, v. 65, n. 5-6, p. 713–722, 2018.

90 MOON, H. S.; LEE, L.; KIM, J. B. Double resonance optical pumping effects in electromagnetically induced transparency. *Opt. Express*, v. 16, n. 16, p. 12163–12170, Aug 2008.

91 VUJICIć, N. et al. Velocity-selective double resonance in doppler-broadened rubidium vapor. *Phys. Rev. A*, v. 87, p. 013438, Jan 2013.

92 MORENO, M. P.; VIANNA, S. S. Coherence induced by a train of ultrashort pulses in a Λ-type system. *J. Opt. Soc. Am. B*, v. 28, n. 5, p. 1124–1129, May 2011.

93 SHENG, D.; GALVÁN, A. P.; OROZCO, L. A. Lifetime measurements of the $5d$ states of rubidium. *Phys. Rev. A*, v. 78, p. 062506, Dec 2008.

94 JEONG, T.; MOON, H. S. Phase correlation between four-wave mixing and optical fields in double Λ-type atomic system. *Opt. Express*, v. 24, n. 25, p. 28774–28783, Dec 2016.

95 BOYD, R. W. et al. Four-wave parametric interactions in a strongly driven two-level system. *Phys. Rev. A*, v. 24, p. 411–423, Jul 1981.

96 STEEL, D. G.; LIND, R. C. Multiresonant behavior in nearly degenerate four-wave mixing: the ac Stark effect. *Opt. Lett.*, v. 6, n. 12, p. 587–589, Dec 1981.

97 LIPSICH, A. et al. Absorption spectra of driven degenerate two-level atomic systems. *Phys. Rev. A*, v. 61, p. 053803, Apr 2000.

98 AKULSHIN, A. M.; BARREIRO, S. V.; LEZAMA, A. Highly selective four-wave mixing of low-intensity radiation in a degenerate two-level atomic system. *Quantum Electronics*, v. 30, n. 3, p. 189, mar 2000.

99 LEZAMA, A.; CARDOSO, G. C.; TABOSA, J. W. R. Polarization dependence of four-wave mixing in a degenerate two-level system. *Phys. Rev. A*, v. 63, p. 013805, Dec 2000.

100 ZHANG, J.-X. et al. Enhanced reflection via phase compensation from anomalous dispersion in atomic vapor. *Phys. Rev. A*, v. 83, p. 053841, May 2011.

101 ALVAREZ, A. S.; ALMEIDA, A. A. C. de; VIANNA, S. S. Two symmetric four-wave mixing signals generated in a medium with anomalous refractive index. *Journal of Physics B: Atomic, Molecular and Optical Physics*, v. 54, n. 4, p. 045403, feb 2021.

102 MOON, G.; NOH, H.-R. Analytic calculation of linear susceptibility in velocity-dependent pump-probe spectroscopy. *Phys. Rev. A*, v. 78, p. 032506, Sep 2008.

103 KIM, K. et al. Observation of arbitrary group velocities of light from superluminal to subluminal on a single atomic transition line. *Phys. Rev. A*, v. 68, p. 013810, Jul 2003.

104 LING, H. Y.; LI, Y.-Q.; XIAO, M. Electromagnetically induced grating: Homogeneously broadened medium. *Phys. Rev. A*, v. 57, p. 1338–1344, Feb 1998.

105 HOSSAIN, M. M. et al. Nonlinear resonances caused by coherent, optical pumping and saturating effects in the presence of three laser fields for the 85rb-d2 line. *Journal of Physics B: Atomic, Molecular and Optical Physics*, v. 44, n. 11, p. 115501, may 2011.

106 KRMPOT, A. J. et al. Sub-doppler absorption narrowing in atomic vapor at two intense laser fields. *Opt. Express*, v. 13, n. 5, p. 1448–1456, Mar 2005.

107 SAUTENKOV, V. A.; ROSTOVTSEV, Y. V.; SCULLY, M. O. Switching between photon-photon correlations and raman anticorrelations in a coherently prepared rb vapor. *Phys. Rev. A*, v. 72, p. 065801, Dec 2005.

108 VARZHAPETYAN, T. S. et al. Intensity correlations in a coherently prepared rb vapor in a magnetic field. *Optics Communications*, v. 282, n. 1, p. 39–44, 2009. ISSN 0030-4018.

109 CHEN, L.-Q. et al. Observation of temporal beating in first- and second-order intensity measurement between independent raman stokes fields in atomic vapor. *Phys. Rev. A*, v. 82, p. 033832, Sep 2010.

110 GOLOVIZIN, A. et al. Compact magneto-optical trap of thulium atoms for a transportable optical clock. *Opt. Express*, v. 29, n. 22, p. 36734–36744, Oct 2021.

111 DINNEEN, T. P. et al. Cold collisions of $\mathrm{sr}^* - \mathrm{Sr}$ in a magneto-optical trap. *Phys. Rev. A*, v. 59, p. 1216–1222, Feb 1999.

112 TELLES, G. D. et al. Inelastic cold collisions of a na/rb mixture in a magneto-optical trap. *Phys. Rev. A*, v. 59, p. R23–R26, Jan 1999.

113 CHU, S. et al. Three-dimensional viscous confinement and cooling of atoms by resonance radiation pressure. *Physical Review Letters*, v. 55, p. 48, 1985.

114 WALLACE, C. D. et al. Measurements of temperature and spring constant in a magneto-optical trap. *Journal of the Optical Society of America B*, v. 11, n. 5, p. 703–711, 1994.

115 RAAB, E. L. et al. Trapping of neutral sodium atoms with radiation pressure. *Physical Review Letters*, v. 59, p. 2631, 1987.

116 STEANE, A. M.; CHOWDHURY, M.; FOOT, C. J. Radiation force in the magneto-optical trap. *Journal of the Optical Society of America B*, v. 9, n. 12, p. 2142–2158, 1992.

117 SCHERER, D. R.; FENNER, D. B.; HENSLEY, J. M. Characterization of alkali metal dispensers and non-evaporable getter pumps in ultrahigh vacuum systems for cold atomic sensors. *Journal of Vacuum Science & Technology A*, v. 30, p. 061602, 2012.

118 VEISSIER, L. *Quantum memory protocols in large cold atomic ensembles*. Thesis (Phd) — Université Pierre et Marie Curie - Paris VI, Paris, France, 2013. Accessed on: 17 jan. 2019.

119 PALITTAPONGARNPIM, P. *Characterization of Magneto-optical Trap For Experiments in Light-Atom Interfacing*. Dissertation (Master's thesis) — University of Calgary, 2012.

120 AGRAWAL, G. Phase conjugation and degenerate four-wave mixing in three-level systems. *IEEE Journal of Quantum Electronics*, v. 17, n. 12, p. 2335–2340, 1981.

121 BOUBLIL, S.; WILSON-GORDON, A.; FRIEDMANN, H. Two-photon coherence and steady-state saturated and inverted populations in three-level systems. *Journal of Modern Optics*, v. 38, n. 9, p. 1739–1761, 1991.

122 MCINTYRE, D. H. et al. Diode-laser noise spectroscopy of rubidium. *Opt. Lett.*, v. 18, n. 21, p. 1816–1818, Nov 1993.

123 CAMPARO, J. C.; COFFER, J. G.; FRUEHOLZ, R. P. Temporal response of an atom to a stochastic field: Resonant enhancement of population fluctuations at the rabi frequency. *Phys. Rev. A*, v. 56, p. 1007–1011, Jul 1997.

124 CAMPARO, J. C.; COFFER, J. G.; FRUEHOLZ, R. P. Rabi resonances induced by an off-resonant, stochastic field. *Phys. Rev. A*, v. 58, p. 3873–3878, Nov 1998.

125 CAMPARO, J. C.; COFFER, J. G. Conversion of laser phase noise to amplitude noise in a resonant atomic vapor: The role of laser linewidth. *Phys. Rev. A*, v. 59, p. 728–735, Jan 1999.

126 NORRIS, D. G. et al. Observation of ground-state quantum beats in atomic spontaneous emission. *Phys. Rev. Lett.*, v. 105, p. 123602, Sep 2010.

127 AGARWAL, G. S. Exact solution for the influence of laser temporal fluctuations on resonance fluorescence. *Phys. Rev. Lett.*, v. 37, p. 1383–1386, Nov 1976.

128 GARDINER, C. *Stochastic Methods: A Handbook for the Natural and Social Sciences*. [S.l.]: Springer Berlin Heidelberg, 2009. (Springer Series in Synergetics). ISBN 9783540707134.

129 GARDINER, C.; ZOLLER, P. *Quantum noise: a handbook of Markovian and non-Markovian quantum stochastic methods with applications to quantum optics*. [S.l.]: Springer Science & Business Media, 2004.

130 ORSZAG, M. *Quantum Optics: Including Noise Reduction, Trapped Ions, Quantum Trajectories, and Decoherence*. [S.l.]: Springer International Publishing, 2018. ISBN 9783319804774.

131 VANIER, J. Atomic clocks based on coherent population trapping: a review. *Applied Physics B*, v. 81, n. 4, p. 421–442, Aug 2005. ISSN 1432-0649.

132 ESNAULT, F.-X. et al. Cold-atom double-Λ coherent population trapping clock. *Phys. Rev. A*, v. 88, p. 042120, Oct 2013.

133 ARAÚJO, M. O. et al. Measurement of the kerr nonlinear refractive index of cs vapor. *Phys. Rev. A*, v. 88, p. 063818, Dec 2013.

134 GRAY, H. R.; WHITLEY, R. M.; STROUD, C. R. Coherent trapping of atomic populations. *Opt. Lett.*, v. 3, n. 6, p. 218–220, Dec 1978.

135 ALMEIDA, A. A. C. de. *Spectral analysis of the four-wave mixing in a cold atomic sample using a single CW laser*. Dissertation (Master's thesis) — Universidade Federal de Pernambuco, 2019.

APPENDIX A – *WOLFRAM MATHEMATICA* - EIT IN A 3-LEVEL SYSTEM

EIT in a 3-level system - Chapter 2

Parameters

```
Γ21 = Γ23 = 2 * Pi * 3; (*Population decay rate in MHz*)
r = 5;
j = 0.01;
Ωa = r * Γ21; (*Control laser Rabi frequency*)
Ωb = j * Γ21; (* Probe laser Rabi frequency*)
γ12 = γ21 = γ23 = γ32 = 0.5 * Γ21; (*Coherence decay rate*)
γ13 = γ31 = (10^-2) * Γ21; (*Coherence decay rate*)
δa = 2 * Pi * 0; (*Control laser detuning*)
δb = 2 * Pi * x; (*Probe laser detuning*)
rangeplot = 50;
```

Solving the equations

We write the Bloch equations in a matrix format.

```
In[ ]:= R = {{Γ21}, {0}, {Γ23}, {0}, {0}, {0}, {0}, {0}, {0}};
```

```
In[ ]:= M = {{-Γ21, 0, -Γ21, -I * Ωa, 0, 0, I * Conjugate[Ωa], 0, 0},
 {0, -(Γ21 + Γ23), 0, I * Ωa, 0, -I * Conjugate[Ωb], -I * Conjugate[Ωa], 0, I * Ωb},
 {-Γ23, 0, -Γ23, 0, 0, I * Conjugate[Ωb], 0, 0, -I * Ωb},
 {-I * Conjugate[Ωa], I * Conjugate[Ωa], 0, -(γ12 + I * δa), -I * Conjugate[Ωb], 0, 0, 0, 0},
 {0, 0, 0, -I * Ωb, -(γ13 + I * (δa - δb)), I * Conjugate[Ωa], 0, 0, 0},
 {0, -I * Ωb, I * Ωb, 0, I * Ωa, -(γ23 - I * δb), 0, 0, 0},
 {I * Ωa, -I * Ωa, 0, 0, 0, 0, -(γ21 - I * δa), I * Ωb, 0},
 {0, 0, 0, 0, 0, 0, I * Conjugate[Ωb], -(γ31 - I * (δa - δb)), -I * Ωa},
 {0, I * Conjugate[Ωb], -I * Conjugate[Ωb], 0, 0, 0, 0, -I * Conjugate[Ωa], -(γ32 + I * δb)}};
```

```
In[ ]:= Xd = LinearSolve[M, R, Method → "DivisionFreeRowReduction"];
```

```
In[ ]:= rho11d = Extract[Xd[[1]], 1];
rho22d = Extract[Xd[[2]], 1];
rho33d = Extract[Xd[[3]], 1];
sigma12d = Extract[Xd[[4]], 1];
sigma13d = Extract[Xd[[5]], 1];
sigma23d = Extract[Xd[[6]], 1];
sigma21d = Extract[Xd[[7]], 1];
sigma31d = Extract[Xd[[8]], 1];
sigma32d = Extract[Xd[[9]], 1];
```

EIT example of chapter 2

```
In[ ]:= Plot[Im[sigma23d], {x, -rangeplot, rangeplot},
         PlotRange → All, Frame → True, FrameLabel → {"δb/2π (MHz)", "Im(σ23)"}]
```

Out[ ]=

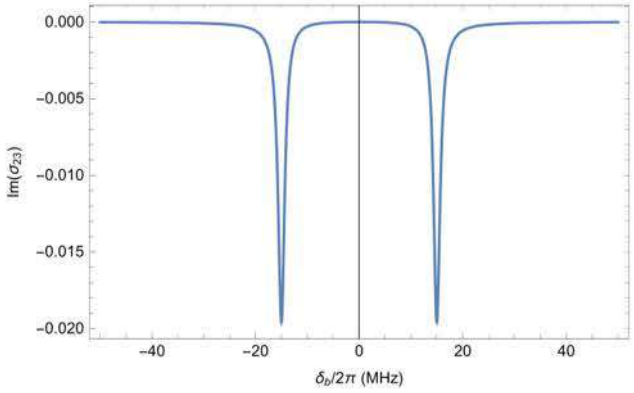

APPENDIX B – *WOLFRAM MATHEMATICA* - FWM SPECTRA OF SECTION 4

Forward FWM in copropagating configuration - Chapter 4

Parameters

```
Γ21 = Γ23 = 2 * Pi * 3; (*Population decay rate*)
r = 60;
j = 60;
Ωa = r * Γ21; (*Control laser Rabi frequency*)
Ωb = j * Γ21; (* Probe laser Rabi frequency*)
γ12 = γ21 = γ23 = γ32 = 0.5 * Γ21; (*Coherence decay rate*)
γ13 = γ31 = (10^-2) * Γ21; (*Coherence decay rate*)
δa = 2 * Pi * 0; (*Control laser detuning*)
δb = 2 * Pi * x;(*Probe laser detuning*)
rangeplot = 200;
step = 5;
g = 2 * Pi * 1 * 10^6; (*Time of flight decay rate*)
ω21 = 2 * Pi * 384 227 940.837 * 10^6; (*Optical frequency of the transition*)
c = 2.99792458 * 10^8; (*Speed of light*)
k = ω12/c; (*Wavevector*)
δa = 2 * Pi * 0 * 10^6 - k * v; (*Fixed laser detuning*)
δb = 2 * Pi * x * 10^6 - k * v; (*Scanning laser detuning*)
u = Sqrt[(2 * 313 * 1.38 × 10^-23)/(1.443 × 10^-25)] ;(*Atomic speed variance at T=40ºC*)
L = 0.05; (*Sample length*)
t = 0.04; (*Angle between incident input laser beams*)
d = 2 * 10^18; (*Atomic density*)
permitivitty = 8.854 * 10^-12;
dipoleMoment = 2.07 * 10^-29;
hbar = 1.054 * 10^-34;
κ = ω21 * d * dipoleMoment^2 / (2 * hbar * permitivitty * c);
```

Solving the equations

We write the Bloch equations in a matrix format.

```
R = {{-g * 0.5}, {0}, {-g * 0.5}, {0}, {0}, {0}, {0}, {0}, {0}};
```

```
M = {{-g, Γ21, 0, -I * Ωa, 0, 0, I * Conjugate[Ωa], 0},
 {0, -(g + Γ21 + Γ23), 0, I * Ωa, 0, -I * Conjugate[Ωb], -I * Conjugate[Ωa], 0},
 {0, Γ23, -g, 0, 0, I * Conjugate[Ωb], 0, 0},
 {-I * Conjugate[Ωa], I * Conjugate[Ωa], 0, -(g + γ12 + I * δa), -I * Conjugate[Ωb], 0, 0, 0},
 {0, 0, 0, -I * Ωb, -(g + γ13 + I * (δa - δb)), I * Conjugate[Ωa], 0, 0},
 {0, -I * Ωb, I * Ωb, 0, I * Ωa, -(g + γ23 - I * δb), 0, 0},
 {I * Ωa, -I * Ωa, 0, 0, 0, 0, -(g + γ21 - I * δa), I * Ωb},
 {0, 0, 0, 0, 0, 0, I * Conjugate[Ωb], -(g + γ31 - I * (δa - δb))},
 {0, I * Conjugate[Ωb], -I * Conjugate[Ωb], 0, 0, 0, 0, -I * Conjugate[Ωa], -(g +
```

```
Xd = SetPrecision[LinearSolve[M, R, Method → "CofactorExpansion"], MachinePrecision];
```

```
In[•]:= rho11d = Extract[Xd[[1]], 1];
        rho22d = Extract[Xd[[2]], 1];
        rho33d = Extract[Xd[[3]], 1];
        sigma12d = Extract[Xd[[4]], 1];
        sigma13d = Extract[Xd[[5]], 1];
        sigma23d = Extract[Xd[[6]], 1];
        sigma21d = Extract[Xd[[7]], 1];
        sigma31d = Extract[Xd[[8]], 1];
        sigma32d = Extract[Xd[[9]], 1];
```

```
In[•]:= nA = 1 + (d * dipoleMoment^2 / (2 * permitivitty * hbar)) * (Re[sigma12d] / (Ωa));
        nB = 1 + (d * dipoleMoment^2 / (2 * permitivitty * hbar)) * (Re[sigma23d] / (Ωb));
        deltaKB = (2 * (ω12) / c) * (Cos[t / 2] - Cos[3 * t / 2]) -
            ((ω23 + (2 * Pi * (x) * 10^6)) / c) * (nB * Cos[t / 2] - nA * Cos[3 * t / 2]);
        X3 = I * κ * (I * sigma31d * Ωa, / (-2 * I * δa + I * δb + γ12 + g));
        X1 =
          -κ * 0.5 / (-2 * I * δa + I * δb + γ12 + g);
        Ωs = X3 * (Exp[X1 * L] - Exp[I * deltaKB * L]) / (X1 - I * deltaKB);
```

Numerical integration

```
dataINT = Transpose[{Table[x, {x, -rangeplot, rangeplot, passointegral}],
    Table[NIntegrate[1/(u √π) e^(-(v)^2/u^2) * (Ωs / 10^6), {v, -∞, ∞},
      Method → "DoubleExponential", MaxRecursion → 50, WorkingPrecision → 10],
     {x, -rangeplot, rangeplot, passointegral}]}];

dataFWM = Transpose[{Table[x, {x, -rangeplot, rangeplot, passointegral}],
    data[[All, 2]] * Conjugate[data[[All, 2]]]}];
```

```
In[•]:= ListPlot[{dataFWM}, PlotRange → All, Joined → True,
         MaxPlotPoints → Infinity, Frame → True, FrameLabel → {"δb/2π (MHz)", "|Ωs|²"}]
```

Out[•]=

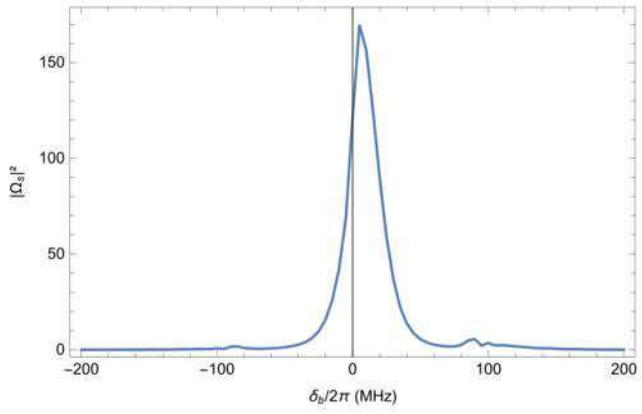

APPENDIX C – PYTHON CODE OF SECTION 5

```
1  iimport numpy as np
2
3  rangeG2=0.5E-6 #G2 Range in us. Be careful, the longer the interval, slower
       the program.
4
5  def G2(tau,I1,I2, N,stepG2): #G2 function for positive delays
6
7      numerator=0
8      denominator1=0
9      denominator2=0
10
11     mean1=np.mean(I1)
12     mean2=np.mean(I2)
13
14     for i in range (0,N,stepG2):
15         denominator1=denominator1+(I1[i]-mean1)*(I1[i]-mean1)
16     denominator1=denominator1/N
17
18
19     for i in range (0,N-tau,stepG2):
20         numerator=numerator+(I1[i]-mean1)*(I2[i+tau]-mean2)
21         denominator2=denominator2+(I2[i+tau]-mean2)*(I2[i+tau]-mean2)
22     numerator=numerator/(N-tau)
23     denominator2=denominator2/(N-tau)
24
25
26     return numerator/np.sqrt(denominator1*denominator2)
27
28 def fullG2(I1,I2, timeVecG2, cut, N,Samples,stepG2): #Function to build the
       final correlation curve adding positive and negative delays
```

```
29
30      if (len(timeVecG2) % 2) == 0:
31          timeVecG2=np.arange((-1E6*(cut*N)/Samples),1E6*(cut*N)/Samples,stepG2*1E6/Samples)
32          vecG2P=np.zeros(int(len(timeVecG2)//2)+1)
33          for i in range(0,int(len(timeVecG2)//2)+1):
34              vecG2P[i]=G2(i*stepG2,I1,I2, N,stepG2)
35
36          vecG2N=np.zeros(int(len(timeVecG2)//2))
37          for i in range(0,int(len(timeVecG2)//2)):
38              vecG2N[i]=G2((i+1)*stepG2,I2,I1, N, stepG2)
39      else:
40          timeVecG2=np.arange((-1E6*(cut*N)/Samples),1E6*(cut*N)/Samples+1E6/Samples,stepG2*
41          vecG2P=np.zeros(int(len(timeVecG2)//2)+1)
42          for i in range(0,int(len(timeVecG2)//2)+1):
43              vecG2P[i]=G2(i*stepG2,I1,I2, N,stepG2)
44
45
46          vecG2N=np.zeros(int(len(timeVecG2)//2))
47          for i in range(0,int(len(timeVecG2)//2)):
48              vecG2N[i]=G2((i+1)*stepG2,I2,I1, N,stepG2)
49
50      vecG2=np.concatenate([np.flip(vecG2N),vecG2P])
51
52      return vecG2
53
54
55  def main(c1,c2,begin,end): #Choose the columns to calculate the correlation
        between them.
56      for i in range(begin,end):
57          DATE = '2022.08.05'
58          SOURCE = i
59          print('Date: '+DATE+' Curve: '+str(SOURCE))
60
```

```
61          path = 'File_address_'+DATE+'\\{}.txt'
62          file = path.format(str(SOURCE))
63
64          sampling, s1, s2 =np.loadtxt(file, delimiter='\t', skiprows=1,
                usecols=(0,c1,c2), unpack=True)
65
66          Samples=int(1/(sampling[1]-sampling[0]))
67          if Samples%10==9:
68              Samples+=1
69          elif Samples%10==1:
70              Samples-=1
71          CutRight = int(0E-6*Samples) #Time cut to the right -> useful for
                extracting smaller intervals in big sets of data
72          CutLeft = int(0E-6*Samples)
73
74          stepG2 = 1; #For faster runs, you may choose to jump some points with
                this parameters.
75
76          dataG2 = []
77          pearson = []
78          I1=s1[CutLeft:-CutRight:1]
79          I2=s2[CutLeft:-CutRight:1]
80          N=len(I1)
81          cut=rangeG2*Samples/(N)
82          timeVecG2=np.arange((-cut*1E6*N/Samples)+1E6/Samples,cut*1E6*N/Samples,stepG2*1E6/
83          dataG2.append(fullG2(I1, I2,timeVecG2, cut, N,Samples,stepG2))
```

APPENDIX D – *WOLFRAM MATHEMATICA* - INTENSITY CORRELATIONS OF SECTION 5

Intensity correlations between transmission signals - chapter 5

Parameters

```
t0 = 0; (*Inital time (μs)*)
tF = 20; (*Final time (μs)*)
step = 10^-3;
j = .1;
x = 30;
Γ21 = Γ23 = 2 * Pi * 6; (*Population decay rate (MHz)*)
Ωa = Ωb = j * Γ21; (*Rabi frequency*)
γ12 = γ21 = Γ21 * 0.5; (*Coherence decay rate*)
γ23 = γ32 = Γ23 * 0.5; (*Coherence decay rate*)
γ13 = γ31 = (10^-2) * γ12; (*Coherence decay rate*)
ρ11,0 = 0.5; (*Initial population*)
ρ33,0 = 0.5; (*Initial population*)
δa = 2 * Pi * x; (*Detuning*)
δb = 2 * Pi * x; (*Detuning*)
```

We write the Bloch equations keeping the time dependence.

```
In[•]:= eqs = {drho11[t] == (i Conjugate[Ωa] sigma21[t] + rho22[t] Γ21 - i sigma12[t] Ωa) dt,
    drho22[t] == (-i Conjugate[Ωa] sigma21[t] - i Conjugate[Ωb] sigma23[t] +
        rho22[t] (-Γ21 - Γ23) + i sigma12[t] Ωa + i sigma32[t] Ωb) dt,
    drho33[t] == (i Conjugate[Ωb] sigma23[t] + rho22[t] Γ23 - i sigma32[t] Ωb) dt,
    dsigma12[t] == (-i Conjugate[Ωa] rho11[t] + i Conjugate[Ωa] rho22[t] - i Conjugate[Ωb]
          sigma13[t] + sigma12[t] (-γ12 - i δa)) dt + i sigma12[t] × dw[t], dsigma13[t] ==
     (i Conjugate[Ωa] sigma23[t] + sigma13[t] (-γ13 - i (δa - δb)) - i sigma12[t] Ωb) dt,
    dsigma23[t] == (sigma23[t] (-γ23 + i δb) + i sigma13[t] Ωa - i rho22[t] Ωb + i rho33[t] Ωb)
      dt - i sigma23[t] × dw[t], dsigma21[t] ==
     (sigma21[t] (-γ21 + i δa) + i rho11[t] Ωa - i rho22[t] Ωa + i sigma31[t] Ωb) dt -
      i sigma21[t] × dw[t], dsigma31[t] ==
     (i Conjugate[Ωb] sigma21[t] + sigma31[t] (-γ31 + i (δa - δb)) - i sigma32[t] Ωa) dt,
    dsigma32[t] == (i Conjugate[Ωb] rho22[t] - i Conjugate[Ωb] rho33[t] -
         i Conjugate[Ωa] sigma31[t] + sigma32[t] (-γ32 - i δb)) dt + i sigma32[t] × dw[t]};
```

Define the itô's process and solve the SDEs.

```
In[•]:= proc = ItoProcess[eqs, {rho11[t], rho22[t], rho33[t], sigma12[t],
      sigma13[t], sigma23[t], sigma21[t], sigma31[t], sigma32[t]},
     {{rho11, rho22, rho33, sigma12, sigma13, sigma23, sigma21, sigma31, sigma32},
      {ρ11,0, 0, ρ33,0, 0, 0, 0, 0, 0, 0}}, {t, 0}, w ≃ OrnsteinUhlenbeckProcess[0, 1, 0, 0]];
    data = RandomFunction[proc, {t0, tF, step}, Method → "StochasticRungeKuttaScalarNoise"];

In[•]:= rho11d = data[[2]][[1]][[1]][[All, 1]];
    rho22d = data[[2]][[1]][[1]][[All, 2]];
    rho33d = data[[2]][[1]][[1]][[All, 3]];
    sigma12d = data[[2]][[1]][[1]][[All, 4]];
    sigma13d = data[[2]][[1]][[1]][[All, 5]];
    sigma23d = data[[2]][[1]][[1]][[All, 6]];
    sigma21d = data[[2]][[1]][[1]][[All, 7]];
    sigma31d = data[[2]][[1]][[1]][[All, 8]];
    sigma32d = data[[2]][[1]][[1]][[All, 9]];
```

We plot part of the simulated time series.

```
In[•]:= ListLinePlot[Im[sigma32d][[10000 ;; 11000]], PlotRange → All,
 Frame → True, FrameLabel → {"Time (ns)", "Im(sigma12)"}]
```

Out[•]=

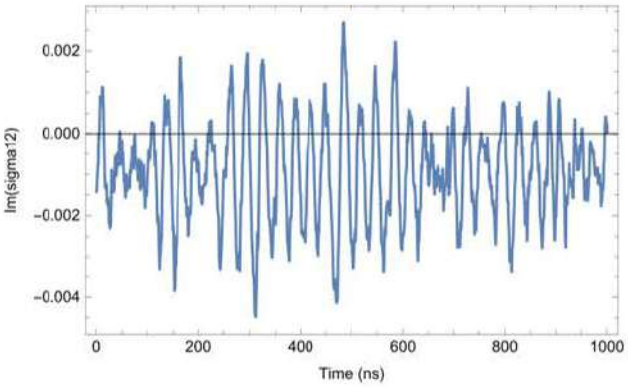

Finally, we calculate the cross -correlation between intensity fluctuations.

```
In[•]:= xcorr[m_] := Mean[Drop[Standardize[Im[sigma21d[[10000 ;;]]]], -m] *
    Drop[Standardize[Im[sigma23d[[10000 ;;]]]], m]]
g2 = Table[xcorr[m], {m, -500, 500}];
ListLinePlot[g2, PlotRange → {All, {-1, 1}},
 Frame → True, FrameLabel → {"Delay (ns)", "g2"}]
```

Out[•]=

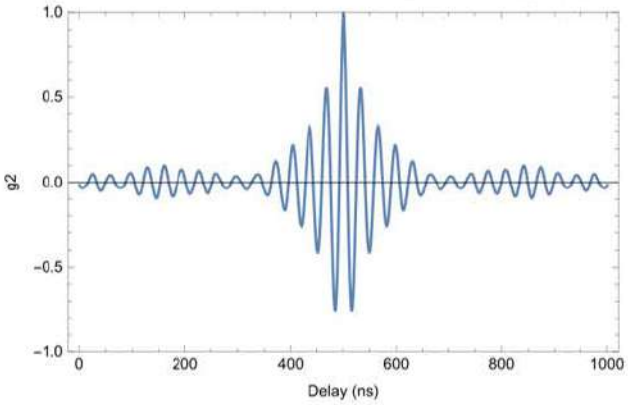

We can also calculate the Fourier transform of the correlation function, showing a peak consistent with the chosen detuning.

```
In[•]:= ft = Fourier[g2, FourierParameters → {-1, 1}];
        sr = 1 / stepTempo;
        ff = Table[(n - 1) sr / Length[ft], {n, Length[ft]}] // N;
        ListLinePlot[Transpose[{ff[[2 ;; 500]], Abs[ft[[2 ;; 500]]]}], PlotRange → All,
         Frame → True, FrameLabel → {"Frequency (MHz)", "Absolute Value"}]
```

Out[•]=